

EXTENSION OF A MICROSACLE INDENTATION FRACTURE MODEL TO  
NANOSCALE CONTACT IN PURVIEW OF MECHANICAL NANOFABRICATION  
PROCESSES

By

JARED HANN

A THESIS PRESENTED TO THE GRADUATE SCHOOL  
OF THE UNIVERSITY OF FLORIDA IN PARTIAL FULFILLMENT  
OF THE REQUIREMENTS FOR THE DEGREE OF  
MASTER OF SCIENCE

UNIVERSITY OF FLORIDA

2012

© 2012 Jared Hann

To my mother Nerida who introduced me to the wonders of science

## ACKNOWLEDGMENTS

I would like to acknowledge all those who were instrumental in my journey, which has brought me to the point of graduating with a Master of Science in mechanical engineering. First and foremost I must give all thanks to my maker. I have been the recipient of what I consider to be many blessings from the almighty, without which, I would not be here. I have experienced miracles, which have shaped a remarkable story. I am forever grateful for these.

I would like to thank my mother who introduced me to science, and filled the house with fascinating books throughout my childhood. She provided essential opportunities and encouraged my passion for science and creativity. I am deeply grateful to my mother for this.

I would like to thank all the teachers who made a difference in my life, particularly Mr. Graham, my 6<sup>th</sup> grade teacher. The way a teacher helps a child in those early years can have a profound and lasting effect.

I would like to thank two of my greatest mentors – Marty Holzworth and Steve Ashfield. They found me during a difficult time, saw potential in me, encouraged me to fulfill my dreams, and gave me the right tools. Without them, I wouldn't be here.

I would like to thank my advisor Professor Curtis Taylor, who took me into his lab, taught me, and mentored me through graduate school. He sent me to a number of conferences and provided me with the opportunities that have been instrumental in my engineering progression. He has taken a keen and sincere interest in enhancing my skills and in teaching me how to achieve success. He has a remarkable talent in teaching, from which many others and I have been the beneficiary.

I would like to thank my lab partner Eddie McCumiskey. He is one of the most helpful and selfless people one could meet. Since I first came into this lab two years ago, he has helped me and everyone else in the lab in all of our projects. He is the ultimate team player, and any lab, group, company or organization will be lucky to have him working for them. There are many people, including myself, who can say that without Eddie, they wouldn't be where they are.

I would like to thank everyone else who has helped me. There are many of them. I have been blessed with many wonderful friends. I may not have mentioned their names here, but I know them, and I am very grateful for them and their kindness. To name just a few, I would like to thank Professor Greenslet, Professor Segal, Dr. Mahla, Bijoyraj, Luis, Mina, Raul, Arnab, Sean, Qiuya, and everyone else who has seen me through graduate school and made a difference. I will endeavor to help others, as they have each helped me.

Last, but certainly not least, I would like to thank my wife, Nichelle, who took a big risk, and married me! She is wonderful. We have experienced the challenges and joys of graduate school together. We are a great team and are excited to progress to the next set of challenges that come our way.

# TABLE OF CONTENTS

	<u>page</u>
ACKNOWLEDGMENTS.....	4
LIST OF FIGURES.....	9
LIST OF ABBREVIATIONS.....	12
ABSTRACT.....	13
CHAPTER	
1 INTRODUCTION.....	15
1.1 Mechanical Nanofabrication.....	15
1.2 Problem Statement.....	17
1.3 Hypothesis.....	17
1.4 Objectives.....	18
1.5 Organization of Thesis.....	19
2 LITERATURE REVIEW & BACKGROUND.....	21
2.1 Nanoindentation.....	21
2.2 Nanoindentation and Fracture of Brittle Materials.....	22
2.3 Indentation Fracture Model.....	24
2.4 Extension of the Indentation Fracture Model to Nanoscale Contacts.....	29
2.5 Sharp Indenters Reduce the Fracture Threshold.....	30
2.6 Residual Stress Can Affect Material Response.....	31
2.7 Interacting Stress Fields Influence Deformation and Fracture.....	31
2.8 Cyclic Indentations Influence Deformation and Fracture.....	33
2.9 Manufacturing Basis for Extending the Indentation Fracture Model to Nanoscale Contact and Ultra-low Loads.....	35
2.10 Atomic Force Microscopy is Used to Characterize Nanoindentations.....	35
2.11 Nanoindentation on Si(100).....	39
3 MATERIALS & METHODS.....	42
3.1 Overview.....	42
3.2 Preparing the Si(100) Substrate for Nanoindentation.....	42
3.3 Asylum Research MFP-3D™ Nanoindenter.....	44
3.4 Asylum Research MFP-3D™ Atomic Force Microscope (AFM).....	46
3.5 Virtual Deflection Calibration.....	47
3.6 Inverted Optical Lever Sensitivity (InvOLS) Calibration.....	48
3.8 Locating the Nanoindentations.....	50
3.9 Scanning the Indents Using Atomic Force Microscopy.....	51
3.10 Calculating the Maximum Indent Depth From Nanoindentation Data.....	52

3.11	Post-Processing AFM Data with SPIP™ Software.....	53
3.12	Locating and Measuring Radial Cracks .....	55
3.13	Measuring Residual Indent Depth.....	56
3.14	Cube Corner Tip Metrology.....	57
4	FRACTURE THRESHOLD EXPERIMENT .....	59
4.1	Overview .....	59
4.2	Calibration and Preparation .....	59
4.3	Nanoindentation Array .....	59
4.4	Results.....	65
4.5	Discussion .....	67
5	ADJACENT INDENTATION EXPERIMENT .....	69
5.1	Overview.....	69
5.2	Calibration and Preparation .....	69
5.3	Adjacent Nanoindentation Array .....	69
5.4	Results.....	72
5.5	Discussion .....	76
5.4.1	No Fracture Below the Threshold.....	76
5.4.2	Elastic Relaxation of Indents .....	77
5.4.3	Adjacent Nanoindentations Separated by $0a$ .....	77
5.4.4	Adjacent Nanoindentations Separated by $10a$ .....	77
5.4.5	Adjacent Nanoindentations Separated by $5a$ .....	78
5.4.6	Adjacent Nanoindentations Separated by $2a$ .....	78
5.4.7	Adjacent Nanoindentations Separated by $1a$ .....	80
5.4.8	Stress Field Contours for Adjacent Indentations .....	80
5.4.8.1	Equations of stress for a rigid cone contact .....	81
5.4.8.2	Polar stress coordinates.....	82
5.4.8.3	Principal stresses .....	85
5.4.8.4	Von Mises stress criterion .....	85
5.4.8.5	Modeling the stress field contours in Matlab .....	86
5.4.8.6	Von Mises stress field contours for adjacent indentations.....	87
5.4.9	Secondary Radial Cracks Release Residual Stress.....	90
6	CYCLIC LOADED INDENTATION EXPERIMENT .....	92
6.1	Overview .....	92
6.2	Calibration and Preparation .....	92
6.3	Cyclic Load Nanoindentation Array.....	92
6.3	Results.....	95
6.4	Discussion .....	98
7	CONCLUSION.....	100

## APPENDIX

A	MATLAB M-FILE OF VON MISES STRESS FIELD CONTOURS FOR ADJACENT INDENTATIONS .....	103
B	MATLAB M-FILE OF VON MISES STRESS FIELD CONTOURS FOR A SINGLE INDENTATION .....	104
	LIST OF REFERENCES .....	107
	BIOGRAPHICAL SKETCH .....	114

## LIST OF FIGURES

<u>Figure</u>	<u>page</u>
1-1 Illustration of the hypothesis that adjacent and cyclic contacts may induce fracture below the threshold load.....	18
2-1 Illustration of a generic load-displacement curve showing important measured parameters .....	22
2-2 Illustration of the five major types of cracks: cone, palmqvist, median, lateral, and half-penny radial .....	23
2-3 Model for median crack initiation in an elastic/plastic indentation field .....	26
2-4 Plot of equilibrium function $\frac{AE}{E}$ showing development of flaw into full-scale crack at threshold .....	28
2-5 AFM scanning procedure .....	37
2-6 The types of data obtained from each AFM scan, shown using scans of a 400 $\mu$ N cube corner indent in Si(100) .....	39
2-7 Illustrations of Si(100) .....	40
3-1 Si substrate cutting procedure .....	43
3-2 Si substrate cleaning procedure .....	43
3-3 Photograph of the Nanoindenter/AFM experimental set up showing the vibration isolation enclosure which houses the nanoindenter .....	44
3-4 The nanoindenter module .....	45
3-5 Cut-away illustration of the AFM head with nanoindenter module and key parts labeled .....	46
3-6 Illustrations of the AFM cantilever holder .....	47
3-7 Illustration of the virtual deflection calibration .....	48
3-8 Illustration of the InvOLS calibration .....	49
3-9 The Berkovich indenter tip .....	51
3-10 Load displacement curve of a 800 $\mu$ N cube corner indent on Si(100) with maximum depth ( $h_{max}$ ) and final depth ( $h_{final}$ ) labeled .....	53

3-11	AFM scans of an 800 $\mu\text{N}$ cube corner indent in Si(100) with histogram maps of the height data showing post processing procedure.....	54
3-12	AFM scans with horizontal and vertical profiles showing that post processing of images does not affect the depth measurements of indents .....	55
3-13	Amplitude images of an 800 $\mu\text{N}$ cube corner indent in Si(100), showing radial cracks .....	56
3-14	Height images of an 800 $\mu\text{N}$ cube corner indent in Si(100) with 3 line profiles, the mean value of which is taken as the depth measurement .....	57
3-15	Cube corner tip metrology procedure .....	58
4-1	Schematic of the nanoindentation array for determination of the single indentation fracture threshold in Si(100) using a cube corner indenter.....	61
4-2	Selected AFM amplitude images of 1 $\mu\text{N}$ – 10 000 $\mu\text{N}$ cube corner nanoindentations in Si(100) .....	62
4-3	AFM amplitude images of 250 $\mu\text{N}$ – 800 mN cube corner nanoindentations in Si(100).....	63
4-4	Schematic of the nanoindentation array for the determination of the single indentation fracture threshold in Si(100) using a cube corner indenter.....	64
4-5	Selected AFM amplitude images of nanoindentations from the 200 $\mu\text{N}$ – 400 $\mu\text{N}$ array with radial cracks identified .....	65
4-6	AFM amplitude images of a 280 $\mu\text{N}$ indent showing no crack, and a 290 $\mu\text{N}$ indent showing a crack. The threshold load is 280 $\mu\text{N}$ – 290 $\mu\text{N}$ .....	66
4-7	Plots of indent depth vs. indent load and indent width vs. indent load.....	67
4-8	Comparison of fracture threshold values reported in the literature and the results of this study .....	68
5-1	AFM images of indent radius measurements for 50 $\mu\text{N}$ , 200 $\mu\text{N}$ , and 800 $\mu\text{N}$ indents.....	70
5-2	Schematic of the adjacent indentation array.....	71
5-3	A selection of AFM amplitude images of the adjacent indentation array shown as a function of load and indent separation.....	73
5-4	50 $\mu\text{N}$ adjacent indent amplitude images with maximum depth and residual depth measurements.....	74

5-5	200 $\mu\text{N}$ adjacent indent amplitude images with maximum depth and residual depth measurements.....	75
5-6	800 $\mu\text{N}$ adjacent indent amplitude images with maximum depth, residual depth, and radial crack length measurements.....	76
5-7	Amplitude image of 800 $\mu\text{N}$ adjacent indents separated by $2a$ showing an intermediate crack between indents .....	80
5-8	Indentation model for a conical contact penetrating a medium a depth of $b + \epsilon$ .....	82
5-9	Illustration of the polar stress components of an infinitesimal element in response to an indenting cone with normal force ( $N$ ) .....	84
5-10	Illustration of von Mises and Tresca yield surfaces in the principal stress coordinates, including the deviatoric plane and hydrostatic axis .....	86
5-11	Von Mises stress field contours for adjacent indentations .....	88
5-12	Amplitude image of a 800 $\mu\text{N}$ adjacent indents separated by $2a$ with matching Von Mises stress field contours .....	89
5-13	Selected amplitude images of 800 $\mu\text{N}$ indents showing the presence of both primary and secondary cracks.....	91
6-1	Illustration of the cyclic load indentation array .....	95
6-2	Selection of AFM amplitude images of cyclic load indents, showing no fracture below the fracture threshold, $P^*$ .....	96
6-3	Load cycle vs. residual indent depth ( $h_{\text{res}}$ ) plot .....	97
6-4	Load cycle vs. radial crack length ( $c$ ) plot.....	98

## LIST OF ABBREVIATIONS

AFM	Atomic Force Microscopy
LVDT	Linear Variable Differential Transformer
MAF	Magnetic Field Assisted Nanomachining (Finishing)
M-file	Matlab coding file
NPS	Nanopositioning System

Abstract of Thesis Presented to the Graduate School  
of the University of Florida in Partial Fulfillment of the  
Requirements for the Degree of Master of Science

EXTENSION OF A MICROSCALE INDENTATION FRACTURE MODEL  
TO NANOSCALE CONTACT IN PURVIEW OF  
MECHANICAL NANOFABRICATION PROCESSES

By

Jared Hann

August 2012

Chair: Curtis R. Taylor  
Major: Mechanical Engineering

Mechanical nanofabrication technologies will be indispensable in the production of emerging micro- and nanotechnologies. Methods such as nanoimprint embossing, massively parallel tip-based nanofabrication, continuous roll-to-roll processing, free abrasive machining, etc., provide a viable means of scalable nanostructuring of surfaces. However, one of the challenges these processes face is that they involve moving parts and mating of surfaces that contact at dimensions less than 100 nm. Such small contacts concentrate the applied stresses, and can create irreversible damage and fracture, which limits resolution, accuracy, and reproducibility of the fabrication process. Therefore, it is critical to understand the fundamental deformation and fracture mechanisms that occur at nanoscale contacts. To date, there have been no systematic studies performed using nanoindentation at ultra low loads ( $<1\text{mN}$ ) that have tested the applicability of the indentation fracture model at nanoscale contacts ( $<100\text{ nm}$ ), or in the presence of adjacent or cyclic loaded contacts. This work investigated the extension of the Lawn and Evans indentation fracture model (developed primarily for microscale contacts) to nanoscale contacts. Nanoindentation was performed at ultra low loads ( $<1$

mN), using a sharp ( $r \sim 32$  nm) cube corner tip, on Si(100), as a function of load, adjacent indent spacing, and load cycle, to simulate nanoscale contacts in mechanical nanofabrication processes. AFM metrology was used to characterize indent dimensions and radial cracks on the surface. The threshold load for a single, isolated indentation was found to be  $280 \mu\text{N} - 290 \mu\text{N}$ , which is lower than previously reported. The results showed that sequential adjacent indentations performed at close proximity (1 indent separation) interact with each other in a way that increases both indent depth and radial crack length. Cyclic loaded indentations also increased indent depth and radial crack length, due to sub-surface defect pile-up and fatigue. However, neither sequentially loaded adjacent indents, or cyclic indentations caused fracture below the threshold for a single, isolated indentation.

## CHAPTER 1 INTRODUCTION

### 1.1 Mechanical Nanofabrication

Mechanical nanofabrication methods such as nanoimprint embossing<sup>1, 2</sup>, dip-pen nanolithography<sup>3, 4</sup>, continuous roll-to-roll processing<sup>5, 6</sup>, free abrasive machining<sup>7, 8</sup>, etc., will be indispensable in the production of emerging micro- and nano-technologies, and provide a cost-effective means for scalable nanostructuring of surfaces. These methods are capable of nanofabrication with unmatched resolution (<10 nm), and are compatible with almost any material. Product applications include ultra-light-weight and high-resolution space X-ray telescopes<sup>9, 10</sup>, high-density data storage systems<sup>11, 12</sup>, energy efficient solar cells<sup>13, 14</sup>, targeted drug delivery<sup>15, 16</sup>, and many other advanced applications. These technologies have the potential to significantly improve the efficiencies of product energy<sup>17, 18</sup>, healthcare<sup>19, 20</sup>, food production<sup>21, 22</sup>, and a variety of other industries.

Mechanical nanofabrication involves moving parts and mating surfaces that contact at dimensions less than 100 nm. Such small contacts concentrate the applied stresses and can create irreversible damage and fracture that limit resolution, accuracy, and reproducibility of the fabrication process. These limitations represent a significant challenge to the development of leading nanomanufacturing technologies. A greater understanding of the fundamental mechanisms of nanoscale fracture and damage is necessary to overcome these challenges.

In the established indentation fracture model of Lawn and Evans<sup>23</sup> a threshold load and flaw size is observed for initiation of fracture due to sharp indenters (Vickers and Berkovich). Below this threshold, fracture is suppressed. This model was primarily

developed for microscale contacts and hardness testing. Using a Vickers indenter and an approximation for the elastic/plastic indent tensile stress distribution, the model predicts a threshold load of 3 mN and critical flaw size of 200 nm in Si. The suppression of cracking below the threshold is due to the inability of the contact-induced tensile stress to reach a critical value for crack propagation.

In contrast to the indentation fracture model, which was developed for isolated microscale contacts, mechanical nanofabrication methods involve adjacent and cyclic loaded nanoscale (<100 nm) contacts. It is possible that such contacts increase stress in the substrate, resulting in an altered fracture and deformation response. Thus, an investigation of adjacent and cyclic loaded nanoscale contacts, is needed to gain a more complete understanding of the fundamental fracture and deformation mechanisms in mechanical nanofabrication methods.

Magnetic Assisted Finishing (MAF) is an example of a nanofabrication technique that is better understood in light of this study. MAF is a free abrasive machining process that is capable of achieving ultraprecision surfaces (0.18 nm rms)<sup>24</sup> and is being developed to create mirrors for x-ray telescope applications. The material removal mechanism responsible for ultraprecision surface finishing in MAF is currently unknown. Fracture has been proposed as a possible mechanism of material removal with the caveat that in MAF, diamond abrasives strike the substrate with a force <50  $\mu$ N, which is below the currently accepted fracture threshold for a sharp diamond cube corner indenter in Si (500 - 1500  $\mu$ N)<sup>25</sup>. However, it is possible that the adjacent and cyclic contacts present in MAF increase the applied stresses, leading to fracture below the threshold load. Investigation of the effects of adjacent and repeated contacts on

deformation and fracture below the threshold load would potentially validate the theory that fracture may be responsible for material removal in MAF. Furthermore, such an investigation would potentially validate the extension of the indentation fracture model to sharp nanoscale contacts ( $r < 100$  nm) in purview of adjacent and cyclic loaded contact scenarios.

## **1.2 Problem Statement**

To date, there have been no studies that systematically investigated the extension of the indentation fracture model to sharp nanoscale contacts ( $r < 100$  nm) in purview of mechanical nanofabrication techniques, which involve adjacent and cyclic loaded contacts.

## **1.3 Hypothesis**

In the indentation fracture model<sup>23</sup>, it is the magnitude of the tensile stress distribution below a sharp indenter that determines the fracture threshold load. Nanoscale contacts ( $< 100$  nm) create higher tensile stresses, which leads to a lower fracture threshold<sup>25</sup>. Cyclic loaded indentations increase stress concentrations from subsurface defect pile-up and fatigue<sup>26</sup>. Adjacent indentations lead to interacting stress fields that increase sub-surface stress<sup>7</sup>.

Therefore, we hypothesize that the conventional (microscale) indentation fracture model<sup>23</sup> may not apply to sharp nanoscale contacts ( $r < 100$  nm) in purview of adjacent or cyclic loaded contacts. This hypothesis is illustrated in Figure 1-1.

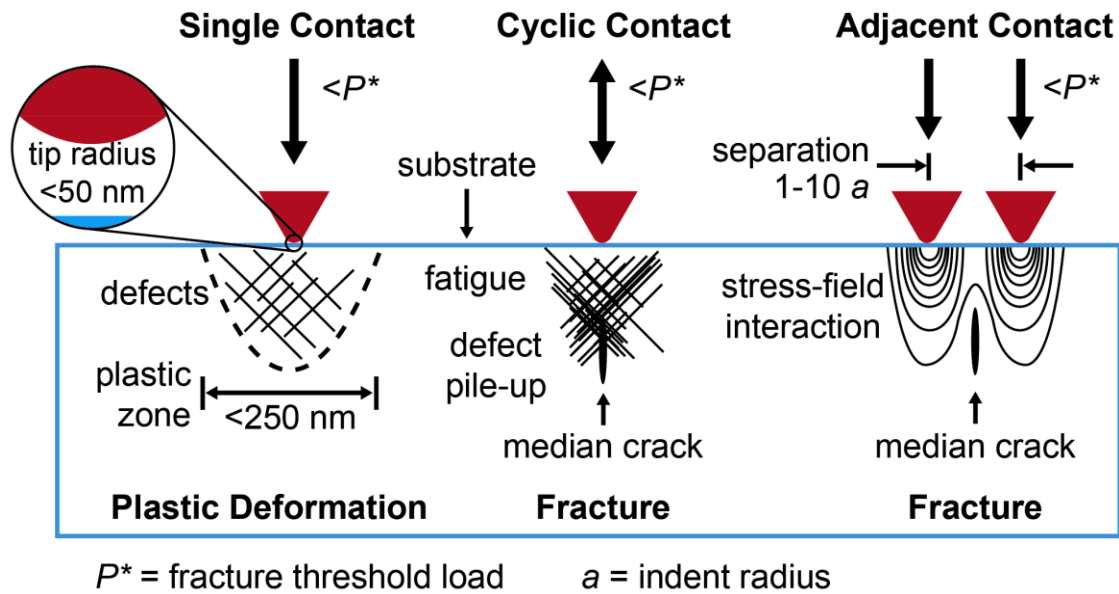


Figure 1-1. Illustration of the hypothesis that adjacent and cyclic contacts may induce fracture below the threshold load ( $P^*$ )

#### 1.4 Objectives

The objectives of this study are three-fold: 1) gain a greater understanding of nanoscale contact induced fracture and deformation, 2) investigate the validity of fracture as a possible material removal mechanism in MAF, and 3) investigate an extension of the current indentation fracture model to nanoscale contacts in purview of adjacent and cyclic loaded contacts scenarios.

These objectives are accomplished through the following systematic experimentation: 1) determine the fracture threshold load for a single isolated indentation in Si(100) using a sharp cube corner indenter ( $r= 32\text{ nm}$ ), 2) determine the effect of adjacent indentations on the fracture threshold load, crack extension, and deformation, and 3) determine the effect of cyclic loaded indentations on the fracture threshold load, crack extension, and deformation.

## 1.5 Organization of Thesis

This thesis is organized into a logical progression of chapters, beginning with the current section: Chapter 1: Introduction.

Chapter 2: Literature Review and Background, provides a review of nanoscale contact fracture. The capabilities and limitations of the indentation fracture model are investigated using evidence from previous studies published in the literature. These studies report the effects of cyclic and adjacent indents on deformation and fracture at relatively high loads ( $>1$  mN), and micro- or macro-scale dimensions ( $>100$  nm). This guides the reader towards the goals and objectives of this study, which are to address the current gap in understanding of cyclic and adjacent contact fracture and deformation at ultra-low loads ( $<1$  mN) and nanoscale dimensions ( $<100$  nm). A hypothesis is provided and a short preview of the experiments that will test the hypothesis is given. A review of nanoindentation and atomic force microscopy is provided to prepare the reader for the experimental sections of this study.

Chapter 3: Materials & Methods, reviews the specifications of the substrate (Si) and instruments (nanoindenter and atomic force microscope) used in all three experiments of this study. The experimental methods that are common to all three experiments are provided in this chapter.

Chapter 4: Fracture Threshold Experiment, details the experiment which determined the fracture threshold of a single, isolated indentation from a cube corner indenter in Si(100). Procedures, results and discussion are provided.

Chapter 5: Adjacent Indentation Experiment, details the investigation of the effects of sequential, adjacent nanoindentations on fracture and deformation. Procedures, results and discussion are provided.

Chapter 6: Cyclic Loaded Indentation Experiment, details the investigation of the effects of nanoindentation load cycle on fracture and deformation. Procedures, results and discussion are provided.

Chapter 7: Conclusion, contains a summary of the results and discussion of all experiments in this study. The impact of this study is followed by limitations and future work. Following the conclusion, an appendix, references and a biographical sketch are provided. References are provided in the Nature journal format.

## CHAPTER 2 LITERATURE REVIEW & BACKGROUND

### 2.1 Nanoindentation

Nanoindentation involves the loading and unloading of a geometrically defined indenter tip into a material using high-resolution sensors and actuators that continuously control and monitor the load and displacement. Load-displacement data is collected and interpreted to obtain mechanical properties such as hardness, elastic modulus, adhesion force, and fracture toughness.<sup>27</sup> One of the great advantages of nanoindentation is that many mechanical properties can be retrieved from load displacement data alone, without the need to image the indent. It is particularly useful in obtaining the mechanical properties of thin films (thickness < 1000 nm), where the surface material can be tested without necessitating removal from the bulk.

The load-displacement curve consists of a loading portion, and an unloading portion (see Figure 2-1). The loading curve represents the load-displacement data acquired as the indenter penetrates the material. The unloading curve represents the load-displacement data acquired as the indenter is withdrawn from the material. The x,y position of the apex of the curve corresponds to the maximum load and maximum depth of the indent. The elastic unloading stiffness,  $S = dP/dh$ , is defined as the slope of the upper portion of the unloading curve during the initial stages of unloading. The accuracy of the hardness and modulus measurements depends on how well these parameters can be measured experimentally. Another important measurement is the permanent depth of penetration after the indenter is fully unloaded,  $h_{\text{final}}$  (final depth). These parameters are depicted in a generic load-displacement plot in Figure 2-1.

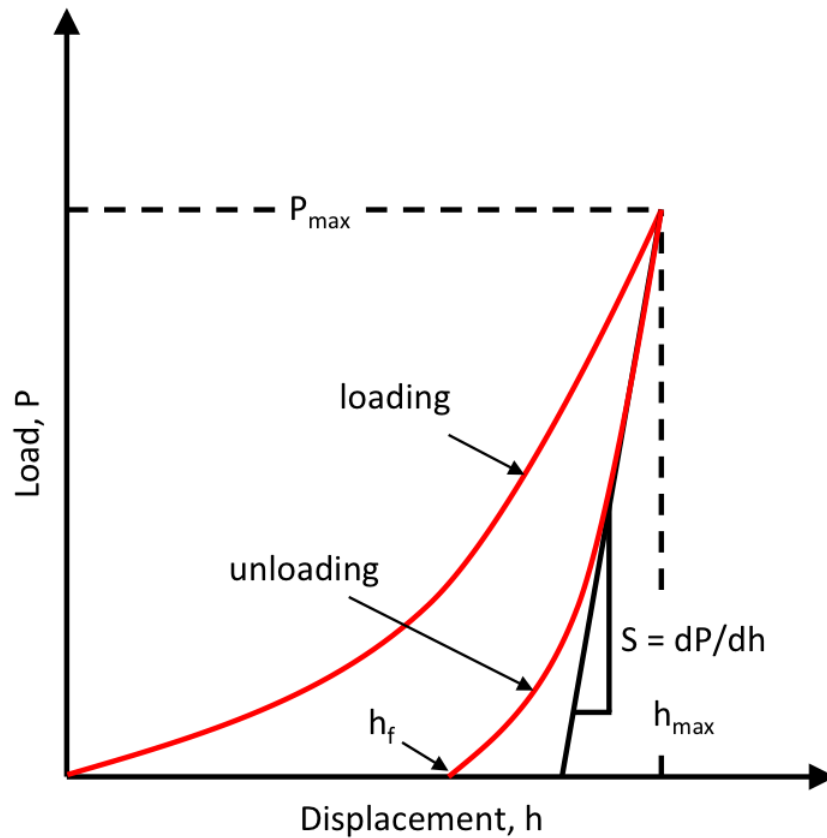


Figure 2-1. Illustration of a generic load-displacement curve showing important measured parameters such as maximum load ( $P_{max}$ ), maximum indentation depth ( $h_{max}$ ), final impression depth ( $h_f$ ), and initial unloading stiffness ( $S$ ).

## 2.2 Nanoindentation and Fracture of Brittle Materials

Nanoindentation is particularly useful in the study of fracture in brittle materials. Sharp indenters are used to make indentations on brittle materials that form radial cracks, which extend from the triangular impression corners. In the indentation of brittle materials there are five major types of cracks depending on the load, material, environmental conditions, and indenter.<sup>28</sup> The five types of cracks are illustrated in Figure 2-2.

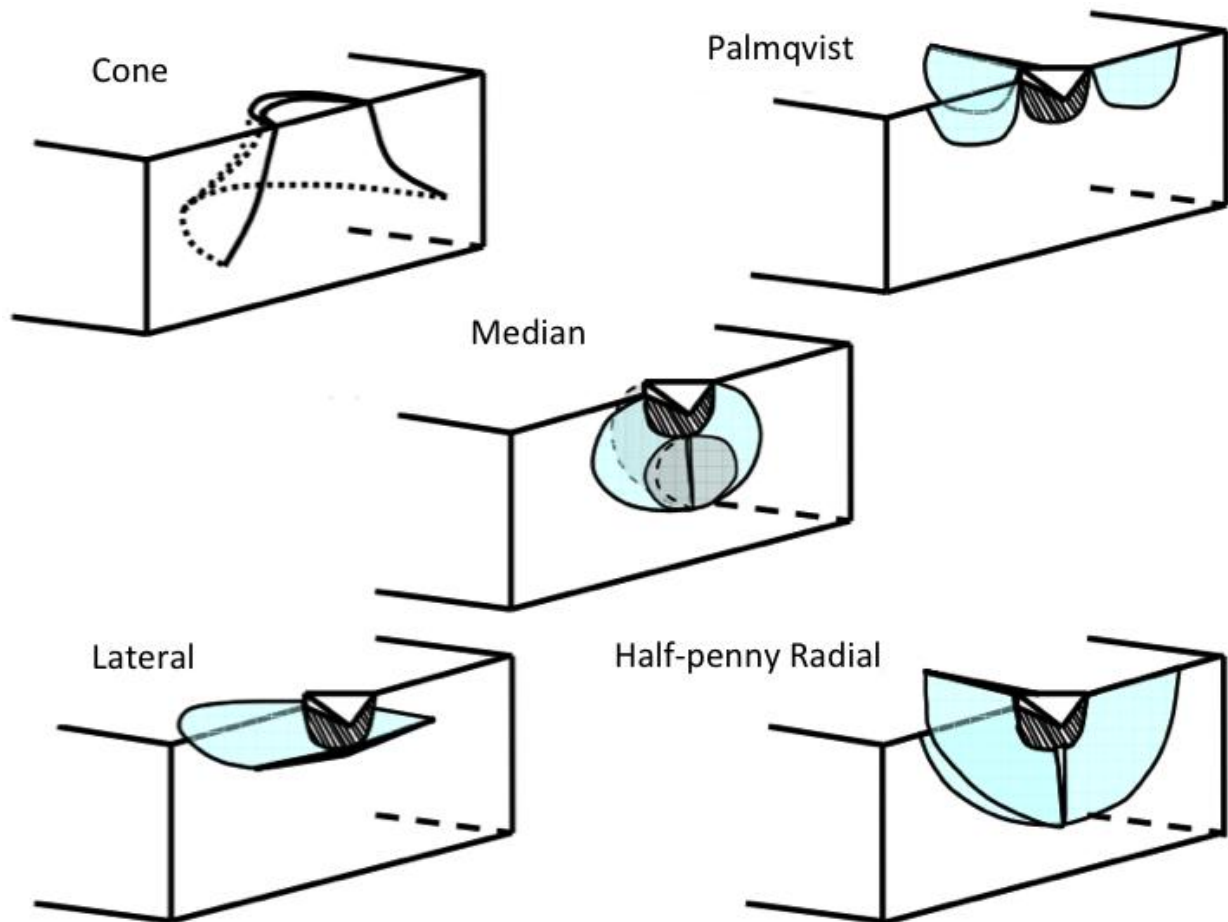


Figure 2-2. Illustration of five major types of cracks: cone, palmqvist, median, lateral, and half-penny radial. [Adapted from Chen, J., Indentation-based methods to assess fracture toughness for thin coatings. *Journal of Physics D: Applied Physics* **45** (20), 2, Figure 1 (2012)]

This thesis is concerned with three of the five crack types in Figure 2-2: median, lateral, and half-penny radial (hereafter referred to as radial). Short descriptions of these three crack types, adapted from the descriptions given by Chen et al.<sup>29</sup> are given below.

**Median:** These types of cracks propagate parallel to the axis of the load but are created beneath the plastic deformation zone due to the wedging action of a pyramidal indenter.

Lateral cracks: These types of cracks generate beneath the plastic deformation zone and initially propagate almost parallel to the surface of the material before turning upwards to the surface to form a chip. They originate from the unloading cycle for most ceramics and from the loading cycle for some glasses. These cracks may also appear in tough materials in cyclic loading. In thin coatings, the lateral crack may also occur at the interface, which can lead to chipping.

Radial cracks: This type of crack usually forms during the unloading procedure. Such a crack may start from a radial crack running downwards, or a median crack running upwards, or a mixture of the two.

Radial crack measurements are used to determine the fracture toughness of the material.<sup>30, 31</sup> Using indentation fracture mechanics theory<sup>32, 33, 34</sup>, Harding, et al.<sup>30</sup> and Pharr<sup>27</sup> determined that the fracture toughness  $K_c$  of the material is related to the radial crack length  $c$  by

$$K_c = \alpha \left( \frac{E}{H} \right)^{1/2} \left( \frac{P}{c^{3/2}} \right) \quad (2-1)$$

where  $P$  represents the nanoindentation load and  $\alpha$  is an empirical geometric constant equal to 0.040<sup>27</sup> for a cube corner indenter.  $H$  and  $E$  are the hardness and Young's elastic modulus, respectively.

### 2.3 Indentation Fracture Model

In the established indentation fracture model of Lawn et al.<sup>23</sup>, a critical load and flaw size threshold is observed for the initiation of fracture due to sharp indenters (Vickers and Berkovich), below which, fracture is suppressed. In the model (Figure 2-3), a sharp indenter at load  $P$  produces a plastic impression of characteristic dimension  $a$  from which the hardness is calculated

$$H = \frac{P}{\alpha\pi a^2} \approx \text{constant} \quad (2-2)$$

where  $\alpha$  is the empirical geometric constant from Equation 2-1, equal to 0.040<sup>27</sup> for a cube corner indenter. Hill's solution<sup>35</sup> for a spherical cavity under internal pressure results in a maximum tensile stress at the elastic/plastic interface, with a decrease towards a negative value at the indenter/specimen contact and within the surrounding elastic region to zero, remote from the contact. Lawn et al.<sup>23</sup> approximated Hill's solution<sup>35</sup> with a linear profile as shown in Figure 2-3. In the model,  $\sigma_m$  is the maximum tensile stress at the interface at a depth  $d$  below the surface and  $b$  is the spatial extent over which the tensile component of the field acts. Peak stress scales with indentation pressure according to

$$\sigma_m = \theta H \approx \text{constant} \quad (2-3)$$

where  $\theta$  is a dimensionless factor. Hardness is the key scaling factor that establishes the intensity of the stress.

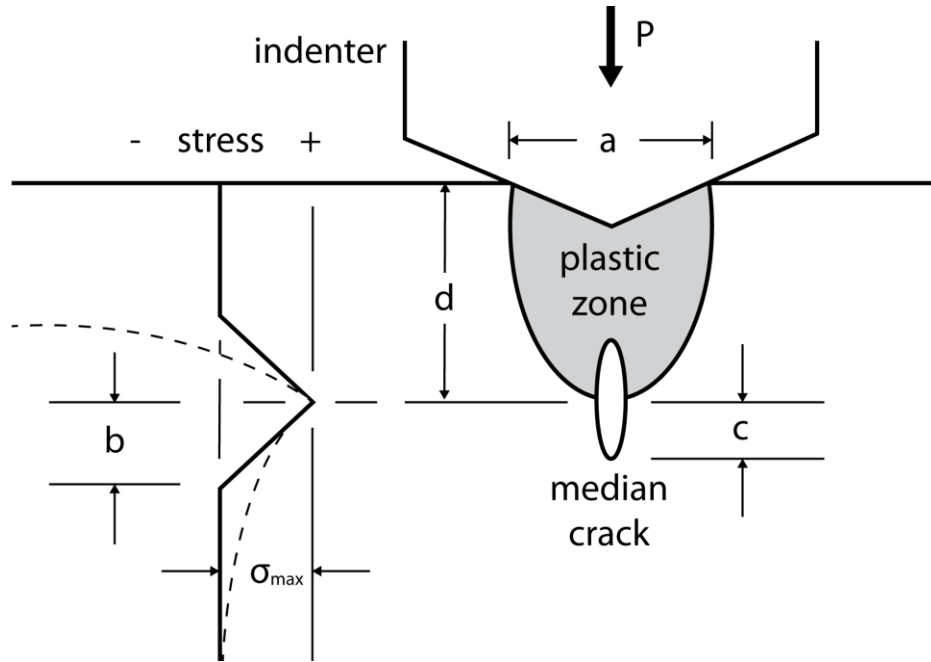


Figure 2-3. Model for median crack initiation in an elastic/plastic indentation field. The nucleation center for the median crack is located in the region of maximum tension, at the base of the plastic zone (shaded). Distribution of normal stress along the load axis is shown according to Hill's elastic/plastic solution (broken curve) and present approximation (full curve). [Adapted from Lawn, B. R. & Evans, A. G., A model for crack initiation in elastic/plastic indentation fields. *Journal of Materials Science* **12**, 2197, Figure 2 (1977)]

The spatial extent of the field scales with indentation size

$$b = \eta a \quad (2-4)$$

where  $\eta$  is a dimensionless factor. Substituting Equation 2-2 into Equation 2-4 gives

$$b = \sqrt{\frac{P\eta^2}{\alpha\pi H}} \quad (2-5)$$

Using a simple approximation for the tensile stress distribution in Figure 2-3

$$\sigma(r) = \sigma_m \left(1 - \frac{r}{b}\right) \quad r \leq b \quad (2-6)$$

$$\sigma(r) = 0 \quad r \geq b \quad (2-7)$$

where  $\sigma(r)$  is the radial stress about the penny axis.

The aim of this model is to determine the loading conditions at which the dominant flaw becomes “critical” and fracture is initiated. By evaluating the stress intensity factor for axially symmetric penny cracks<sup>36</sup>

$$K = \left[ \frac{2}{\sqrt{\pi c}} \right] \int_0^c \frac{r\sigma(r)dr}{\sqrt{(c^2-r^2)}} \quad (2-8)$$

Substituting Equation 2-6 and Equation 2-7 and solving the integral in Equation 2-8

$$K = \sigma_m \left[ \sqrt{\left(\frac{c}{\pi}\right)} \right] \left[ 1 - \frac{1}{2} \sqrt{\left(1 - \frac{b^2}{c^2}\right)} - \frac{c}{2b} \sin^{-1} \left(\frac{b}{c}\right) \right], \quad (c \geq b) \quad (2-9)$$

$$K = 2\sigma_m \left( \sqrt{\left(\frac{c}{\pi}\right)} \right) \left( 1 - \frac{\pi c}{4b} \right), \quad (c \leq b) \quad (2-10)$$

Invoking the condition for Griffith equilibrium

$$K = K_c \quad (2-11)$$

and using Equation 2-3 and Equation 2-5 to eliminate  $\sigma_m$  and  $b$  provides the critical relations for crack extension in reduced notation

$$1 = \mathcal{C}^{1/2} \left[ 1 - \frac{1}{2} \sqrt{\left(1 - \frac{\mathcal{P}}{\mathcal{C}^2}\right)} - \frac{1}{2} \frac{\mathcal{C}}{\mathcal{P}^{1/2}} \sin^{-1} \left(\frac{\mathcal{P}^{1/2}}{\mathcal{C}}\right) \right], \quad (\mathcal{C} \geq \mathcal{P}^{1/2}) \quad (2-12)$$

$$1 = \mathcal{C}^{1/2} \left( 1 - \frac{\pi \mathcal{C}}{4\mathcal{P}^{1/2}} \right), \quad (\mathcal{C} \leq \mathcal{P}^{1/2}) \quad (2-13)$$

using the substitutions

$$\mathcal{C} = \left( \frac{2\theta H}{\pi^{1/2} K_c} \right)^2 c \quad (2-14)$$

$$\mathcal{P} = \left( \frac{26\eta^2 1\theta^4 H^3}{\alpha \pi^3 K_c^4} \right)^2 P \quad (2-15)$$

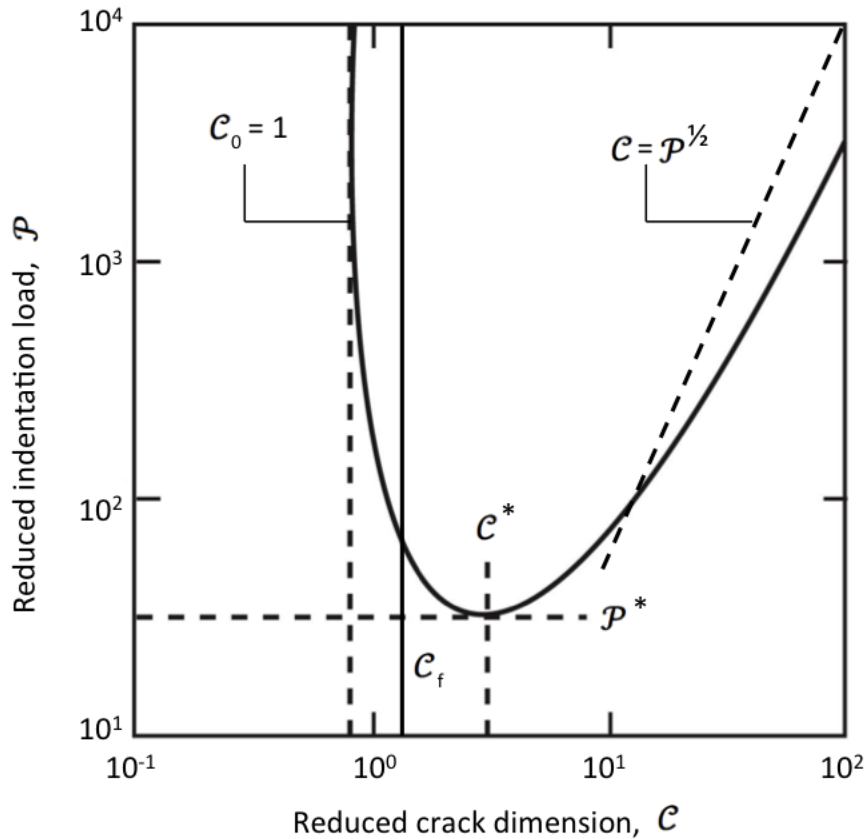


Figure 2-4. Plot of equilibrium function  $P(C)$  showing development of flaw into full-scale crack at threshold, indicated by  $C^*$  (threshold flaw size) and  $P^*$  (threshold load). [Adapted from Lawn, B. R. & Evans, A. G., A model for crack initiation in elastic/plastic indentation fields. *Journal of Materials Science* **12**, 2198, Figure 3 (1977)]

Figure 2-4 illustrates the equilibrium function (Equation 2-12 and Equation 2-13) for development of a flaw into a full-scale crack at threshold  $C^*$  (threshold flaw size) and  $P^*$  (threshold load). As the indenter is loaded, the flaw experiences an increasing driving force until, at the load where the line ' $C_f = \text{constant}$ ' intersects the equilibrium curve, the Griffith condition for extension is satisfied. From this point, the flaw is free to develop into a median crack. The  $P(C)$  curve has a minimum at  $(P^*, C^*)$ , where

$$C^* = 2.250^{23} \quad (2-16)$$

$$P^* = 28.11^{23} \quad (2-17)$$

The result is that no flaw, regardless of its favorable size or location can extend at indentation loads below  $P^*$ . The minimum on the equilibrium curve (Figure 2-4) represents a threshold for the requirements of initiation. The threshold parameters at this point are

$$C^* = \left( \frac{1.767}{\theta^2} \right)^2 \left( \frac{K_c}{H} \right)^2 \quad (2-18)$$

$$P^* = \left( \frac{54.47\alpha}{\eta^2\theta^2} \right)^2 \left( \frac{K_c}{H} \right)^3 K_c \quad (2-19)$$

Using a Vickers indenter, the model predicts a threshold load of 3 mN and a threshold flaw size of 200 nm in Si. Bradby, et al.<sup>25</sup> reported a higher fracture threshold for a Vickers indenter in Si of 20 – 50 mN.

It is important to note that the Lawn & Evans indentation fracture model addresses single, isolated, microscale contacts from an indenter geometry that is traditionally used at relatively very high loads (N) compared to nanoindentation. The model does not accommodate sharper indenters such as the Berkovich or cube corner, nor does it address multiple contact scenarios such as cyclic loading or adjacent interacting contacts.

## **2.4 Extension of the Indentation Fracture Model to Nanoscale Contacts**

We should expect to find fundamental differences between conventional material responses at the macroscale (governed by continuum laws), microscale (governed by discrete defects – defects, dislocations, microstructural interfaces, microcracks), and nanoscale (governed by interatomic force laws).<sup>37</sup> In his famous 1959 lecture “There is Plenty of Room at the Bottom”,<sup>38</sup> Feynman stated that properties inevitably change when approaching the nanoscale, partly due to quantum effects, but also from a shifting balance between competing classical forces as the surface/volume ratio increases.

The question then arises: can the indentation fracture model, which was developed for microscale contacts, be extrapolated to nanoscale dimensions? How valid are the conventional laws of fracture and deformation at the nanoscale? How does repeated nanoindentation in the same location affect the deformation and fracture response of the material? How do interacting stress fields from adjacent nanoindentations at close proximity affect the deformation and fracture response of the material? Do very sharp contacts such as those from the cube corner indenter with tip radii  $<50$  nm cause fracture at a lower threshold load?

### **2.5 Sharp Indenters Reduce the Fracture Threshold**

Nanoindentation has been very useful in the investigation of fracture in brittle materials, using crack length to determine fracture toughness, as described in section 2.2. This method has traditionally used a Vickers indenter, loaded to 10 N or greater, with crack lengths of 100  $\mu\text{m}$  or more. For measuring the fracture toughness of thin films and materials at the nanoscale, smaller indentations are needed. However, the fracture threshold presents a challenge, since below a certain load, no fracture is possible. For Vickers and Berkovich indenters in most ceramic materials, this threshold load is close to 250 mN.<sup>27</sup> This places severe restrictions on the spatial resolution that can be achieved. The cracking threshold depends not only on indenter tip geometry, but also on the condition of the tip. For instance, the cube corner indenter, in theory, has an apex with the geometry of a cube, but in practice the apex is spherical, with a nominal radius.

The cube corner indenter has been effective in measuring fracture toughness of thin films and materials at the nanoscale, because it displaces more than three times<sup>27</sup> the material as the Berkovich for a given load, thus producing greater stresses and

strains in the surrounding material. Considering that nucleation and propagation of indentation cracks are promoted by higher stresses and strains, it is expected that a sharper indenter should have a reduced threshold fracture load. Indeed, Harding, et al.<sup>25</sup> found that cracking thresholds can be reduced by an order of magnitude by using sharp indenters and reported a threshold load of 0.5 mN – 1.5 mN for a cube corner indenter in Si(100).

For a more comprehensive discussion of indenter geometry-dependent fracture mechanisms and fracture toughness evaluation, the review article by Chen et al.<sup>29</sup> is an excellent resource.

## 2.6 Residual Stress Can Affect Material Response

Indentation causes residual stress in the material, which can be measured by utilizing the crack lengths of subsequent indentations. The general expression for the contribution of the residual stress field  $\sigma_r(x)$  to the total stress intensity factor at the tip of a probing crack is given by<sup>39, 33</sup>

$$K = 2 \left( \frac{c}{\pi} \right)^{1/2} \int_0^c \frac{\sigma_r(x)}{\sqrt{(c^2-x^2)}} dx \quad (2-18)$$

This is of particular interest to mechanical nanofabrication processes such as free abrasive machining, where multiple, adjacent abrasives strike the sample, thereby increasing residual stresses in the material.

## 2.7 Interacting Stress Fields Influence Deformation and Fracture

If the stress fields from two adjacent indenters interact, it can potentially affect the material's response to the indentation.

Bhagavat et al.<sup>7</sup> conducted finite element analysis at loads >40 mN to investigate the effect of spacing between multiple indents and reported that abrasive spacing has a

significant impact on material response. In their analysis, as the concentration of the slurry increases, causing the abrasive spacing to decrease, the depth of indentation increases, resulting in more material removal at a prescribed load.

Zhang et al.<sup>40</sup> used finite element analysis at loads >170 N to study interacting Vickers indentations on brittle materials. Their model applied displacement control to the indenter and separated the adjacent indents by a distance  $D$  normalized to the indentation diameter, by  $D/d$ . They reported that the damage created by the second indent is strongly influenced by the damage zone of the original indent. When the normalized separation distance is small, the median damage zone induced by the second indentation was significantly larger than that induced by the first indentation and tended to spread towards the first, creating a zone of intense damage between the two indentations. When the normalized separation was large, i.e.  $D/d > 10$ , the interaction between adjacent indents was negligible. When  $D/d$  was  $\sim 6$ , a slight increase in load was observed. This was because the second indentation was conducted in the hardened plastic region of the first indentation. As the distance was further reduced to  $D/d < 4$ , the indentation load due to the second indent was the same as the first. At this separation, however, the radial crack length was greater on the second indentation than the first. Furthermore, they found that the unloading phase causes significant lateral cracking and tends to create damage in a region in between the two indentations. Experimental validation of their finite element analysis confirmed these results.

Choi, et al.<sup>41</sup>, also studied crack interaction between adjacent Vickers indentations, reporting that cracks due to adjacent indents in soda-lime glass may be

“repulsive” or “attractive” depending on the induced stress field, with the crack size due to the second indent being greater in the “attractive” mode than in the “repulsive” mode.

Twigg, et al.<sup>42</sup> found that the propagation of cracks was influenced by internal residual stress along grain boundaries in addition to the stress field created by adjacent indentations.

To date, however, there have been no systematic studies to investigate the effects of stress field interactions between adjacent indentations from very sharp contacts (cube corner,  $r < 100$  nm) at ultra-low loads ( $< 1$  mN), on deformation, fracture, or the fracture threshold load.

## **2.8 Cyclic Indentations Influence Deformation and Fracture**

Characterization of fatigue properties is vital to designing micro/nanoelectromechanical systems (MEMS/NEMS), and to mechanical nanofabrication techniques in general, because moving components involved in these devices are subject to cyclic loading.

Van Vliet, et al.<sup>43</sup> conducted 2D Bragg-Nye<sup>44</sup> bubble raft models of nucleation beneath sharp indenters and found that during cyclic loading, complete unloading of the crystal resulted in the formation of well-defined slip steps at the surface. These slip steps acted as points of stress concentration, undergoing immediate plastic deformation and emitting dislocations into the crystal upon subsequent reloading of the surface. In contrast, defects that moved to the surface in single loaded indentations did not act as dislocation sources. They found that the contact fatigue response of cyclic indentation suppresses homogenous defect nucleation within the crystal, causing the crystal to yield at lower loads. Furthermore, cyclic contacts led to increased dislocation interactions near the indented surface, resulting in an effective cyclic strain hardening of the crystal.

Muhlstein, et al.<sup>45</sup> reported that Si thin films can degrade and fail under cyclic loading conditions that are 50% of the fracture strength of single cycle. Li, et al.<sup>46</sup> reported that failure in a Si beam occurs after progressive accumulation of damage such as the stable propagation of a crack. Several studies<sup>47, 48, 49</sup> have shown that Indentation with a sharp diamond indenter creates high stresses that can cause pressure-induced phase transformations in Si.

Guiberteau, et al.<sup>26</sup> evaluated sub-surface damage in brittle ceramics due to grinding and polishing using a spherical indenter and found that, at large numbers of cycles and high contact pressures, deformation-induced intergranular microfracture led to severe grain dislodgement. In short, cyclic loading led to increased fatigue damage.

Guiu, et al.<sup>50</sup> used a technique based on repeated indentation with a Vickers indenter to investigate the propagation of sub-surface cracks subjected to cyclic loading in both fine-grained alumina and Zirconia Toughened Alumina (ZTA). They reported evidence that cyclic compressive loads across the work faces produced enhanced crack-growth rates.

Cavalieri<sup>51</sup> performed cyclic nanoindentation using a Berkovich indenter on nanocrystalline metals at loads >5 mN, and found that indentation depth and crack length increases as the number of cycles increase.

However, to date, no studies have investigated the effects of cyclic loading on deformation, cracking, or the fracture threshold at ultra-low loads (<1 mN) or nanoscale contacts (<100 nm).

## **2.9 Manufacturing Basis for Extending the Indentation Fracture Model to Nanoscale Contact and Ultra-low Loads**

The greatest challenge faced by nanomanufacturing today is a lack of understanding of fundamental principles at the nanoscale. The established indentation fracture model of Lawn & Evans was developed for microscale contacts (>100 nm), relatively high loads (mN-N), and single, isolated indentations. In mechanical nanofabrication, moving parts and surfaces contact at dimensions less than 100 nm, at ultra-low loads (<1mN), and include both cyclic and adjacent contacts. These conditions create stress concentrations that cause deformation and fracture, which can limit the resolution, accuracy, and reproducibility of the fabrication process. This adversely affects the optimization and advancement of nanofabrication processes to large-scale manufacturing and production.

A greater understanding of fracture and deformation at the nanoscale is achieved through research using nanoindentation to simulate ultra-low load (<1mN), nanoscale contacts (<100nm) in mechanical nanofabrication processes. Cyclic loaded indents and sequentially loaded adjacent indents simulate the multiple contact conditions in mechanical nanofabrication. Investigating the fracture threshold load under these conditions will test the validity of the indentation fracture model at nanoscale contacts and in multiple contact scenarios.

### **2.10 Atomic Force Microscopy is Used to Characterize Nanoindentations**

AFM is a microscopy technique that can be used to obtain extremely high resolution (~0.3 nm)<sup>52</sup> images of nanoindentations and their associated deformation and surface cracks. Characterization of indents from an AFM image provides very precise indent depth and crack length measurements. 3D topographical maps can be

generated from AFM height data and used to visualize essential features of the indent such as shape, deformation, pile-up, and cracks.

The AFM used in this study operates via an optical lever system, which measures the bending of a flexible cantilever probe as it responds to mechanical interactions with the surface. A super luminescent diode (SLD) shines onto the back of a reflective cantilever, which is mounted at 11 degrees with respect to the sample plane. A lens focuses the light beam from the SLD at the lever, and the light reflects off the cantilever and up to a recollimation lens and mirror to a position sensitive detector, a segmented photodiode. The position of the reflected beam on the photodiode is determined by the change in angle or height of the deflected cantilever. The photodiode is segmented into four quadrants. A voltage is generated from each quadrant that is proportional to the intensity of light illuminating it. An optical lever sensitivity calibration converts the cantilever deflection into a displacement measurement. An illustration of the AFM scanning process and an image taken with AFM are shown in Figure 2-5.

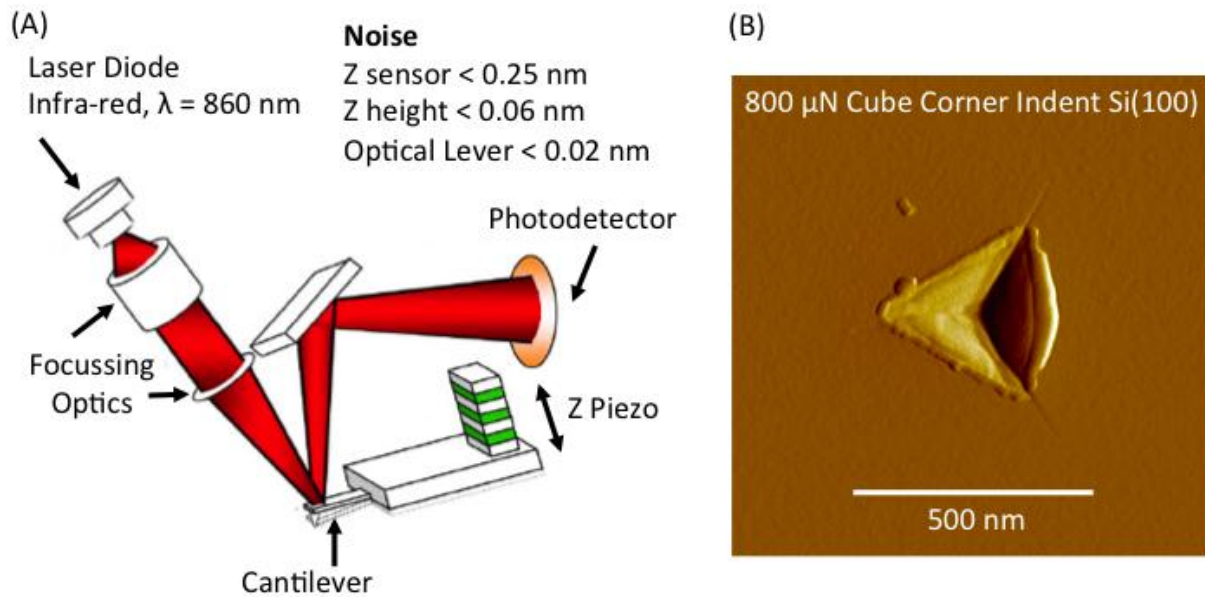


Figure 2-5. AFM scanning. A) AFM optical lever system. B) MFP-3D™ AFM scan of 800  $\mu\text{N}$  Indent using a cube corner indenter tip on Si(100). Photos courtesy of Jared Hann

All AFM scans in this study were performed in non-contact, alternating current (AC) mode operation. In AC mode, the tip oscillates with a specific amplitude, above the sample surface. As the tip scans over the sample surface, the height of the probe is adjusted to keep the oscillation amplitude constant at the set point voltage. To maintain a constant average separation between the tip of the probe and the point of the surface directly beneath it, the Z-piezo moves the cantilever. By decreasing the amplitude set point, the force between the tip and sample is increased. As the surface topography changes, attraction forces will cause the oscillation amplitude of the probe to decrease below the set point value. In response, the feedback system decreases the Z voltage, which moves the tip away from the surface, allowing the amplitude to increase. Likewise, if the probe experiences decreased attraction from the sample, the oscillation amplitude increases above the set point. In response, the feedback system will increase the Z-voltage, which moves the piezo closer to the surface, decreasing the amplitude.

As the tip moves over the surface, it traces the contour of the sample. A single AFM scan in AC mode captures four types of data: height, amplitude, phase, and Z-sensor.

Height data is obtained from the calibrated Z-piezo position. The image obtained from height data provides a 2D topographical map, from which it can be difficult to locate or view features. A 3D visualization can be developed from the height data to improve the appearance of such surface features. Height data is used to measure indent depth and width.

Amplitude data is derived from the difference between the drive amplitude and the oscillation amplitude of the probe, which is caused by tip-sample interactions. This results in an image that looks more like an optical microscope image and aids in the visualization of the shape of features. In this study, amplitude images are used to locate indentation cracks because they are more visible in amplitude scans than in height data scans. Amplitude images are also used to measure radial crack length. It is important to note, however, that the z-height in an amplitude image represents the amplitude and does not provide any meaningful height data. Therefore, indent depth cannot be measured from amplitude images.

Phase data images are another alternative to height images and show the result of tip sample interactions. They are obtained by the change in phase between the drive signal and the response of the cantilever. The phase signal changes when the probe encounters regions of different composition. Phase shifts are registered as bright and dark regions in phase images, comparable to the way height changes are indicated in height images.

Finally, Z sensor data is derived from Z-axis Linear Variable Differential Transformer (LVDT) measurements, which are more accurate than height data but contain more noise and are therefore less precise.

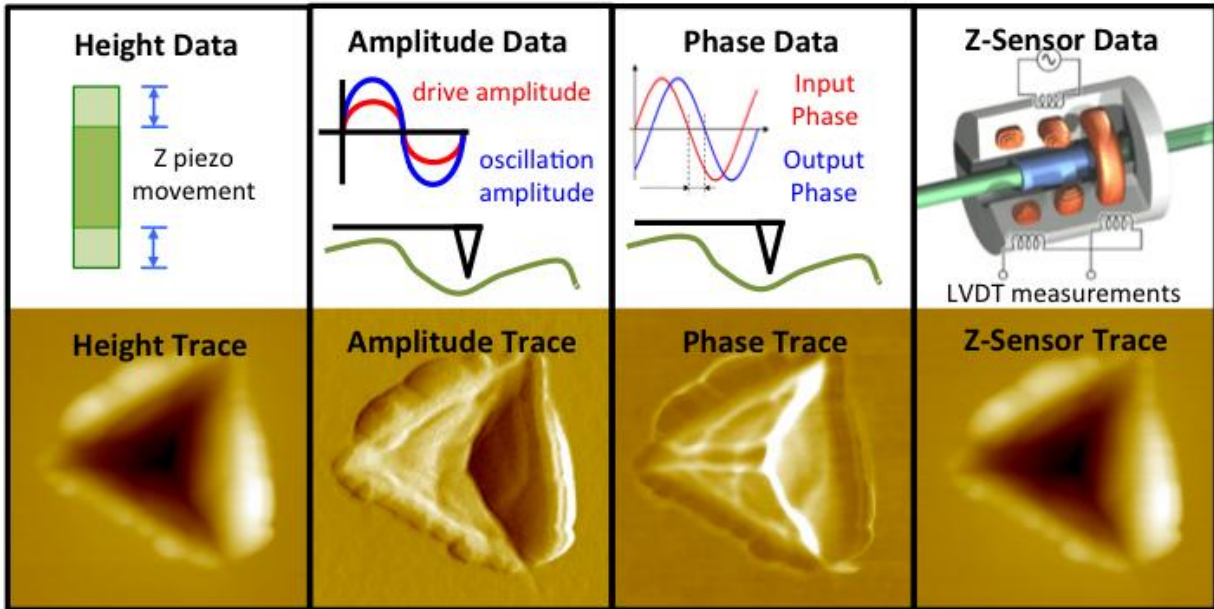


Figure 2-6. The types of data obtained from each AFM scan: height, amplitude, phase, and z-sensor, shown using scans of a  $400\mu\text{N}$  cube corner indent in Si(100)

### 2.11 Nanoindentation on Si(100)

Mechanical nanofabrication techniques are commonly applied to semiconductor materials, the most common of which is single-crystal Si, and particularly the Si(100) crystal orientation. For this reason, Si(100) has been selected as the material on which all nanoindentation will be performed. This will optimize the applications to which the results of these experiments may be applied. Si is to a degree, also representative of brittle materials in general, which further extends the application of these results.

Si is a brittle metalloid and forms a diamond cubic crystal structure, shown in Figure 2-7 (A), in a tetrahedral geometry, shown in Figure 2-7 (B). Nanoindentation

tests on Si(100) have revealed a hardness of 5.1-13.1 GPa and a Young's modulus of 62-179 GPa<sup>54</sup>. These properties are dependent on the doping level.

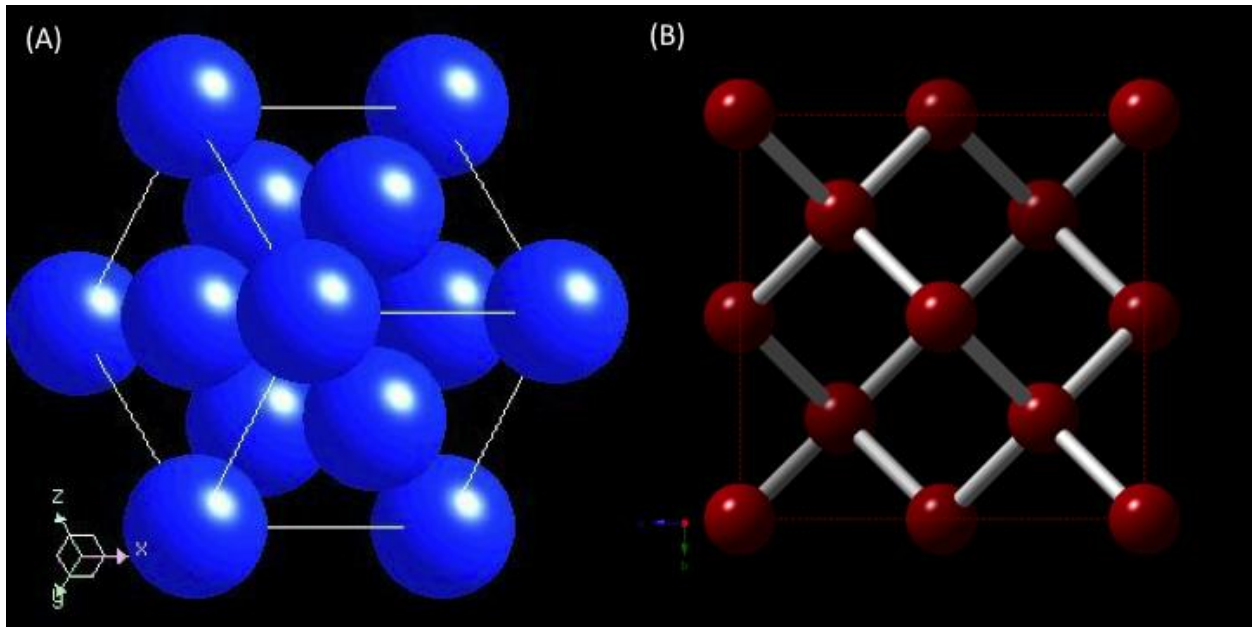


Figure 2-7. Illustrations of Si(100) crystal structure and geometry. A) Face centered cubic (fcc) crystal structure and B) Diamond tetrahedral geometry shown in the [100] direction

During nanoindentation in Si with a Berkovich indenter, the unloading load-displacement curves show a discontinuity (pop-out) at high peak loads (>30 mN) and hysteresis loops at low peak loads (<20 mN).<sup>55</sup> Gogotsi and colleagues<sup>56, 57</sup> proposed that pop-out corresponds to the formation of metastable Si-XII/SiIII crystalline phases, while the hysteresis for one cycle of loading and unloading corresponds to the formation of amorphous Si (a-Si). These features however, depend on the centerline-to-face angle of the indenter tip.

The cube corner indenter is sharp (35.30 centerline-to-face angle) and extrudes a considerable amount of material, thus avoiding phase transformation. However, if the loading rate is low enough, a small amount of Si-II phase remaining in the hardness impression can transform to crystalline Si-XII phase. At rapid unloading rates, the Si-II

phase cannot transform to another crystalline phase due to kinetic barriers to nucleation and growth.<sup>58</sup> The experiments in this study avoid pop-out by indenting with a cube corner tip at ultra-low loads ( $<1$  mN) and a relatively high loading rate (0.2 mN/s).

## CHAPTER 3 MATERIALS & METHODS

### 3.1 Overview

This chapter provides the specifications and preparation of the Si substrate upon which nanoindentation is performed. The specifications of the MFP-3D™ nanoindenter (Asylum Research, Inc., Santa Barbara, CA USA) used in these experiments, are provided. Nanoindentation methods that were common to all three experiments in this study are outlined. The specifications of the MFP-3D™ AFM (Asylum Research Inc.) used in these experiments are provided and the AFM methods common to all experiments are outlined. Post processing methods used to process AFM images are described. Finally, the methods for characterizing the indenter tip, indentation depth, and radial crack length are provided.

### 3.2 Preparing the Si(100) Substrate for Nanoindentation

Nanoindentation was performed on a 10 x 10 mm<sup>2</sup> Si substrate. Using a high precision diamond scribe (Ted Pella, Inc., Redding, CA, USA), the substrate was cut from a 100 mm diameter, 400 μm thick, p-type, boron doped, single crystal, double-sided polish, epi-ready, 8-40 Ω-cm wafer (University Wafer, South Boston, MA), as shown in Figure 3-1 (A).

Next, 5 mg of Crystalbond™ 509-3, clear adhesive (Ted Pella, Inc.) was placed on a 15 mm diameter AFM specimen disc (Ted Pella, Inc.) and heated at 130 °C on a digital hotplate (Thermo Scientific®, Dubuque, IA, USA). This allowed the substrate to bond to the specimen disc upon cooling.

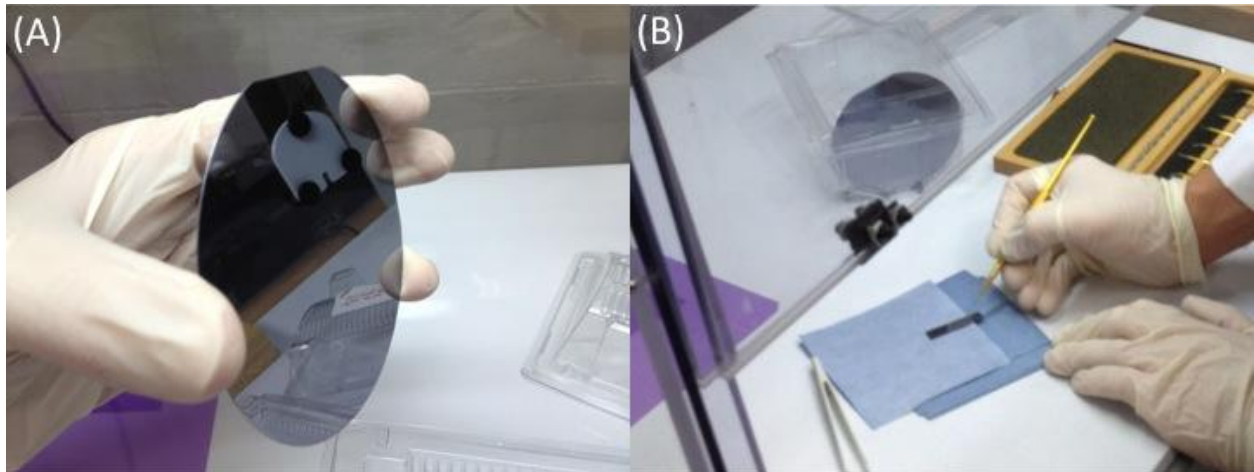


Figure 3-1. Images of the Si wafer cutting procedure. A) A 100 mm diameter Si wafer from which the substrate was cut. B) A square 10 mm<sup>2</sup> Si piece cut from the wafer. Photos courtesy of Jared Hann

Snow cleaning by ultrapure (99.9999%) CO<sub>2</sub> gas was used to prepare a pristine surface. CO<sub>2</sub> passing through a snow jet was applied at 1000 psi for 5 seconds, followed by drying with N<sub>2</sub> gas at 50 psi for 5 seconds, as shown in Figure 3-2 (B). The cleaned sample was checked to confirm that the surface was free of particulates with an AmScope (Irvine, CA, USA) MD600 optical microscope at PL 10/0.25 160/0 resolution.

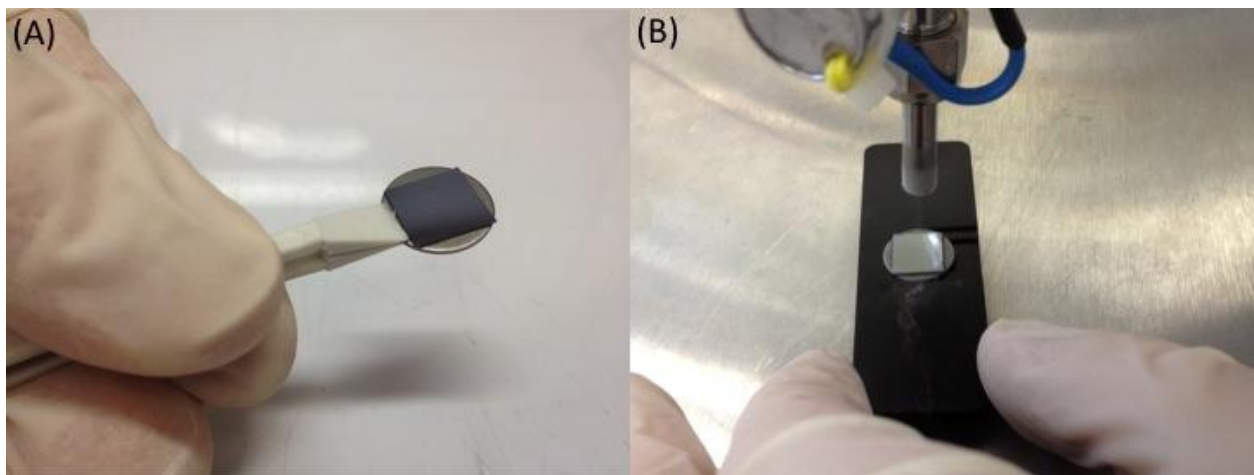


Figure 3-2. Images of the Si substrate cleaning procedure. A) The 10 mm<sup>2</sup> Si substrate bonded to an AFM specimen disc prior to cleaning. B) Cleaning the Si substrate with ultrapure CO<sub>2</sub> snow. Photos courtesy of Jared Hann

### 3.3 Asylum Research MFP-3D™ Nanoindenter

Nanoindentation was performed using a MFP NanoIndenter™ (Asylum Research Inc.) with a 75 nN force and 0.3 nm displacement resolution (both values take into account lab noise). An AEK-2002 (Herzan, Inc., Laguna Hills, CA USA) enclosure provided passive acoustic isolation to the nanoindenter. The nanoindenter was operated by an all-digital ARC2™ Controller using IgorPro (WaveMetrics, Inc., Tigard, OR USA) MFP-3D™ software, which provided low noise, fast operation, and 25+ megapixel resolution. The MFP-3D™ Base illuminating system provided top and bottom viewing for the samples and was positioned on a calibrated 100 kg granite passive vibration isolation slab (Standridge Granite Corp., Santa Fe Springs, CA, USA). The granite slab sat on a Stable Table (Herzan, Inc.) that provided active vibration isolation to the nanoindenter. Photographs of the experimental setup inside the clean room facility and a view inside the acoustic isolation enclosure are shown in Figure 3-3.

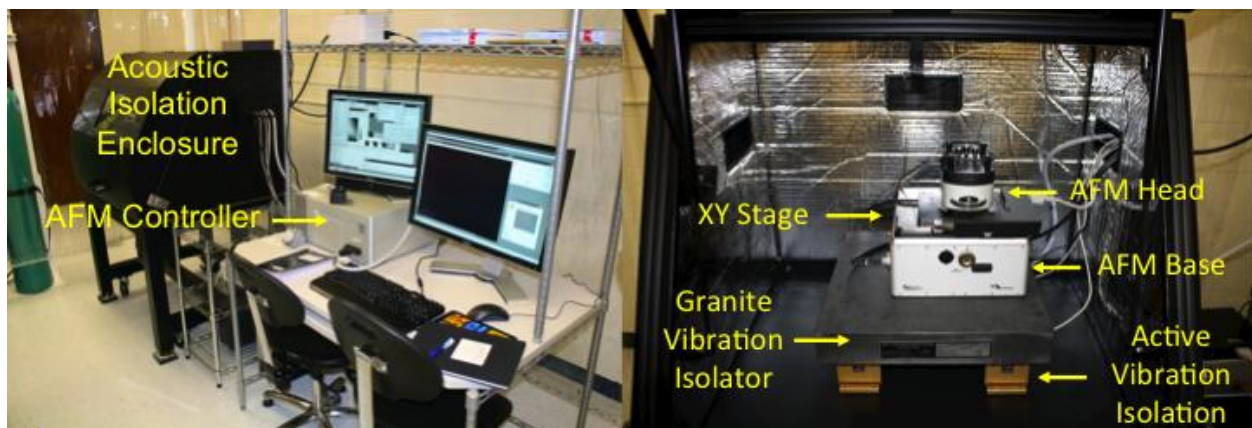


Figure 3-3. Photograph of the Nanoindenter/AFM experimental set up showing the vibration isolation enclosure which houses the nanoindenter, and the controller, which operates it. A view from inside the acoustic isolation enclosure shows the nanoindenter instrument. Photos courtesy of Jared Hann

Nanoindentation was conducted with the nanoindenter module inserted into the AFM head of the MFP-3D™ and placed over the sample, which was placed on an X-Y

scanning stage. The XY stage uses a flexure scanner and patented nanopositioning sensors (NPS™). A photograph of the XY stage, sample mount, and nanoindenter module is shown in Figure 3-4.

The MFP-3D™ has a Z range of 15 μm with a loading rate range of 1 μN/s to 1 mN/s. The noise in the Z height is < 0.06 nm. The flexure spring in the nanoindenter module has a force constant of 3,814 N/m. Using the spring constant of the nanoindenter module and a calibration of the optical lever sensitivity, Z displacement is converted to a force measurement via Hooke's Law. This provides both displacement and force control.

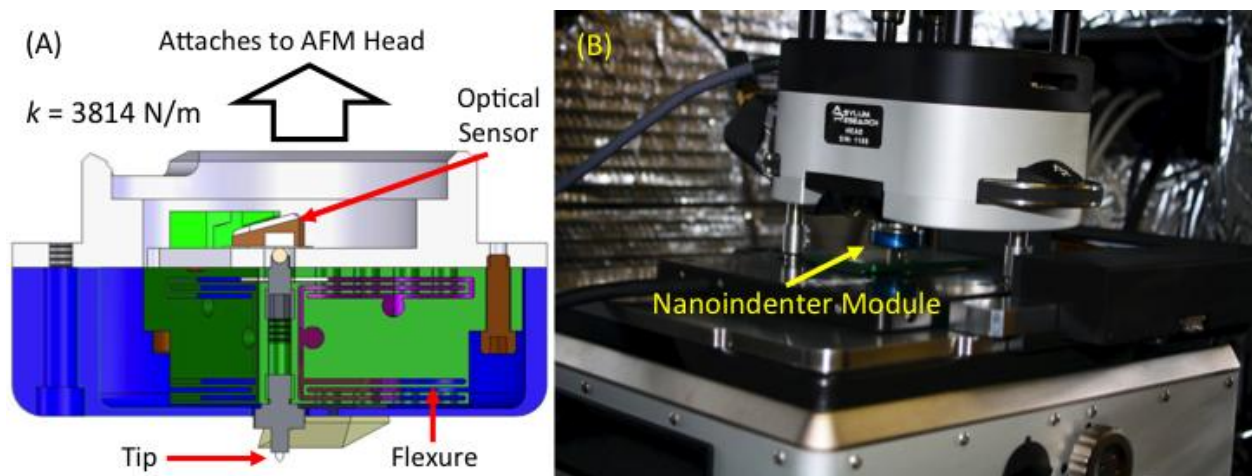


Figure 3-4. The nanoindenter module. A) Cutaway schematic of the MFP-3D™ nanoindenter module. B) Photograph of the nanoindenter instrument showing the module. Photo courtesy of Jared Hann

The nanoindenter operates with a 75 nN lab noise force and 0.3 nm displacement resolution. Positioning accuracy in the sample plane was <0.6 nm using closed-loop nanopositioning sensors.

The MFP-3D™ uses an optical lever sensor with diffraction-limited optics and a low coherence light source that eliminates most interference artifacts. The NPS™ Z-axis sensor records precise measurements of the indenter position which provides accurate

force and topography measurements. A labeled cutaway illustration of the AFM head in the indentation configuration is shown in Figure 3-5.

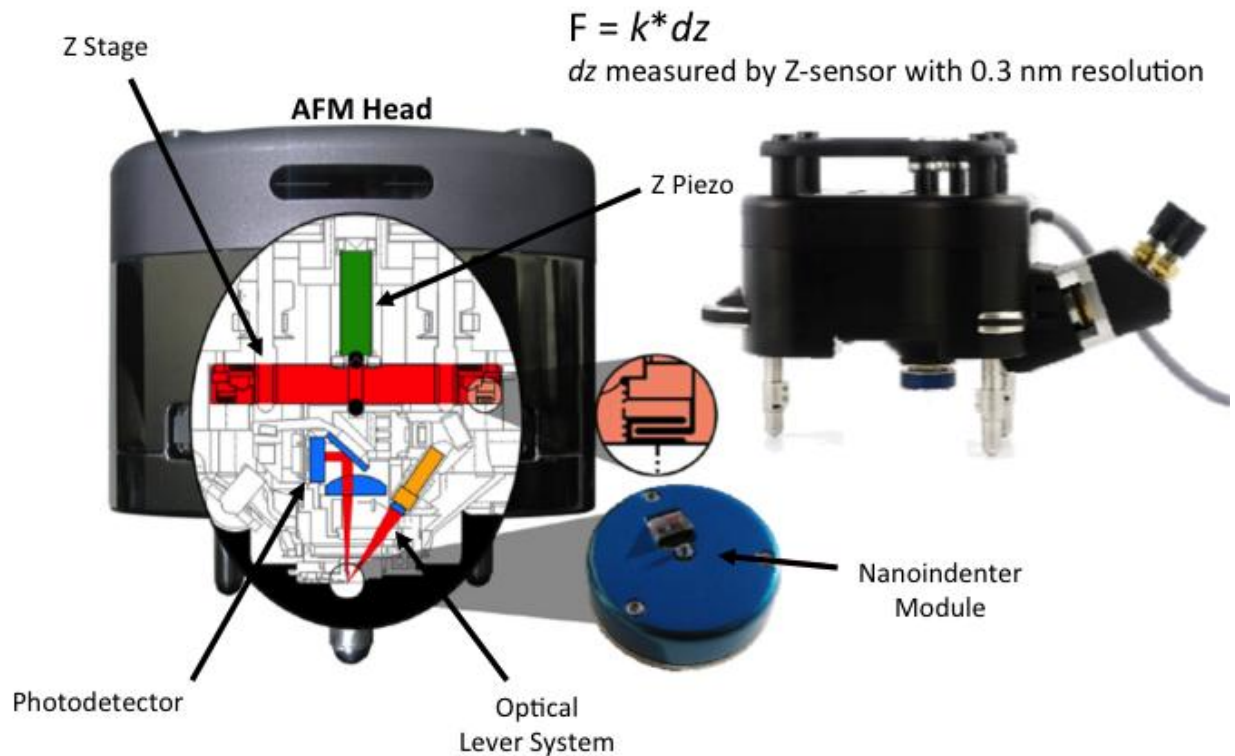


Figure 3-5. Cut-away illustration of the AFM head with nanoindenter module and key parts labeled. [Adapted from Bonilla, A. & Fuierer, R. (Boston, 2008)]

### 3.4 Asylum Research MFP-3D™ Atomic Force Microscope (AFM)

AFM was performed using the same instrument used for nanoindentation (see section 3.3 for details). The MFP-3D™ was operated in AFM mode by removing the nanoindenter module from the AFM head and inserting a cantilever holder module, which is held with a stainless steel clip. The MFP-3D™ supports both contact and non-contact mode imaging and is compatible with both air and fluid imaging. A labeled photograph of the cantilever holder is shown in Figure 3-6.

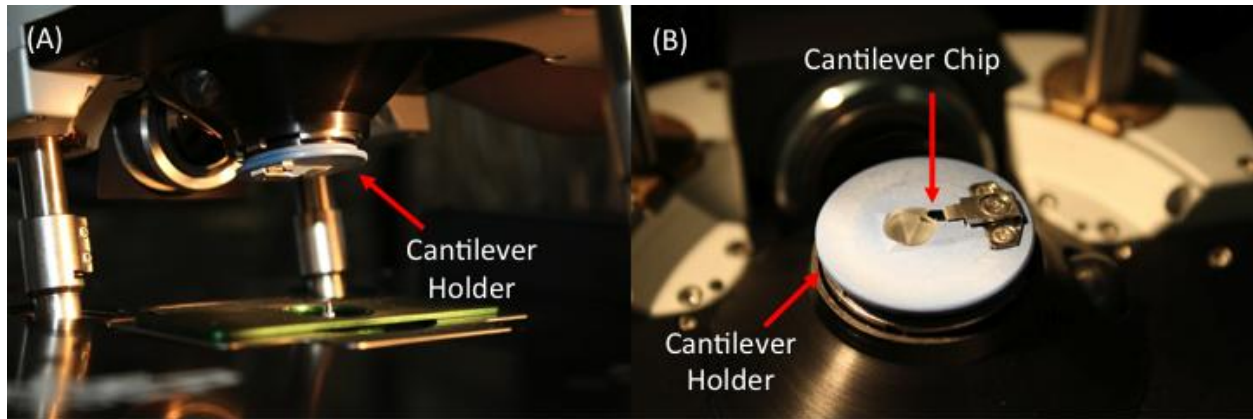


Figure 3-6. Photographs of the AFM cantilever holder. A) Photo of the AFM head as it is placed above a sample to be scanned. B) Photo of the AFM head placed on its back with the cantilever chip clearly visible. Photos courtesy of Jared Hann

Indents were scanned using an SSS-NCH SuperSharpSilicon™ (NANOSENSORS™, Neuchatel, Switzerland) non-contact mode AFM probe with 2-10 nm tip radius.

### 3.5 Virtual Deflection Calibration

Virtual deflection is a mechanical coupling of the photodiode deflection signal with the Z piezo movement. It depends on how the light aligns on the lever and is calibrated by performing a 'virtual' indentation procedure in free air, above the sample. The indenter extends and then retracts over a distance of  $\sim 12 \mu\text{m}$ . Over this range, the deflection is plotted against the Linear Variable Differential Transformer (LVDT), or Z sensor, displacement. A  $\sim 6 \mu\text{m}$  linear portion of this plot is chosen, and a virtual deflection is performed again over this range. From this data, a virtual deflection value is obtained. A typical value is  $\sim 2 \text{ mV}/\mu\text{m}$ . An illustration of the virtual deflection calibration is shown in Figure 3-7.

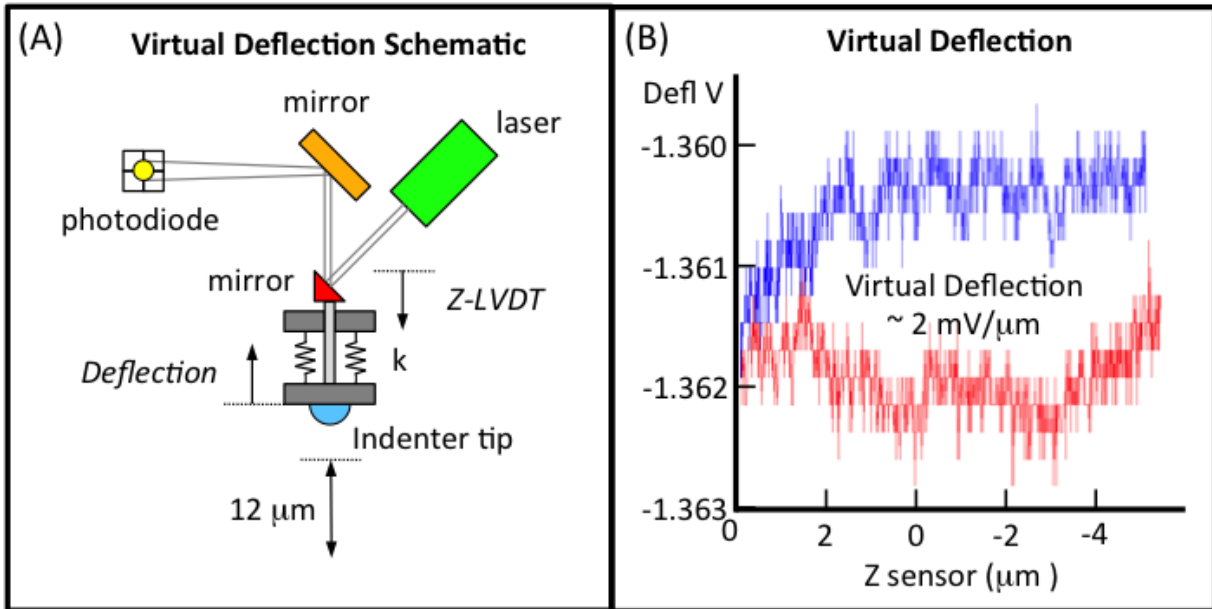


Figure 3.7. Illustrations of the virtual deflection calibration. A) Schematic of the virtual deflection in free air. B) Deflection vs. Z sensor plot for a virtual deflection performed in this study

### 3.6 Inverted Optical Lever Sensitivity (InvOLS) Calibration

To obtain quantitative data from nanoindentation, a calibration of the optical lever sensitivity is performed which returns the Z distance that corresponds to the deflection voltage from the photodiode signal. This is achieved by conducting a hard contact with a spherical sapphire tip, which, if the contact is infinitely hard, results in no plastic deformation (i.e. no indentation depth) and therefore the deflection voltage is equal to Z sensor displacement only.

In the InvOLS procedure for this study, a triggered force was executed with a relative trigger of 4 volts from an initial position of -2 V. For a greater degree of statistical significance, the InvOLS was performed 100 times. Deflection voltage was plotted against Linear Variable Differential Transformer (LVDT) displacement and the InvOLS was calculated over the range -1V to +1V. A scatter plot was created to display

the range of the multiple InvOLS values. After removing outliers further than 1 standard deviation from the mean, a histogram of the remaining values was produced, from which a mean InvOLS measurement was taken. A typical InvOLS value in these experiments was ~ 700 nm/V. This procedure is outlined in Fig 3-8.

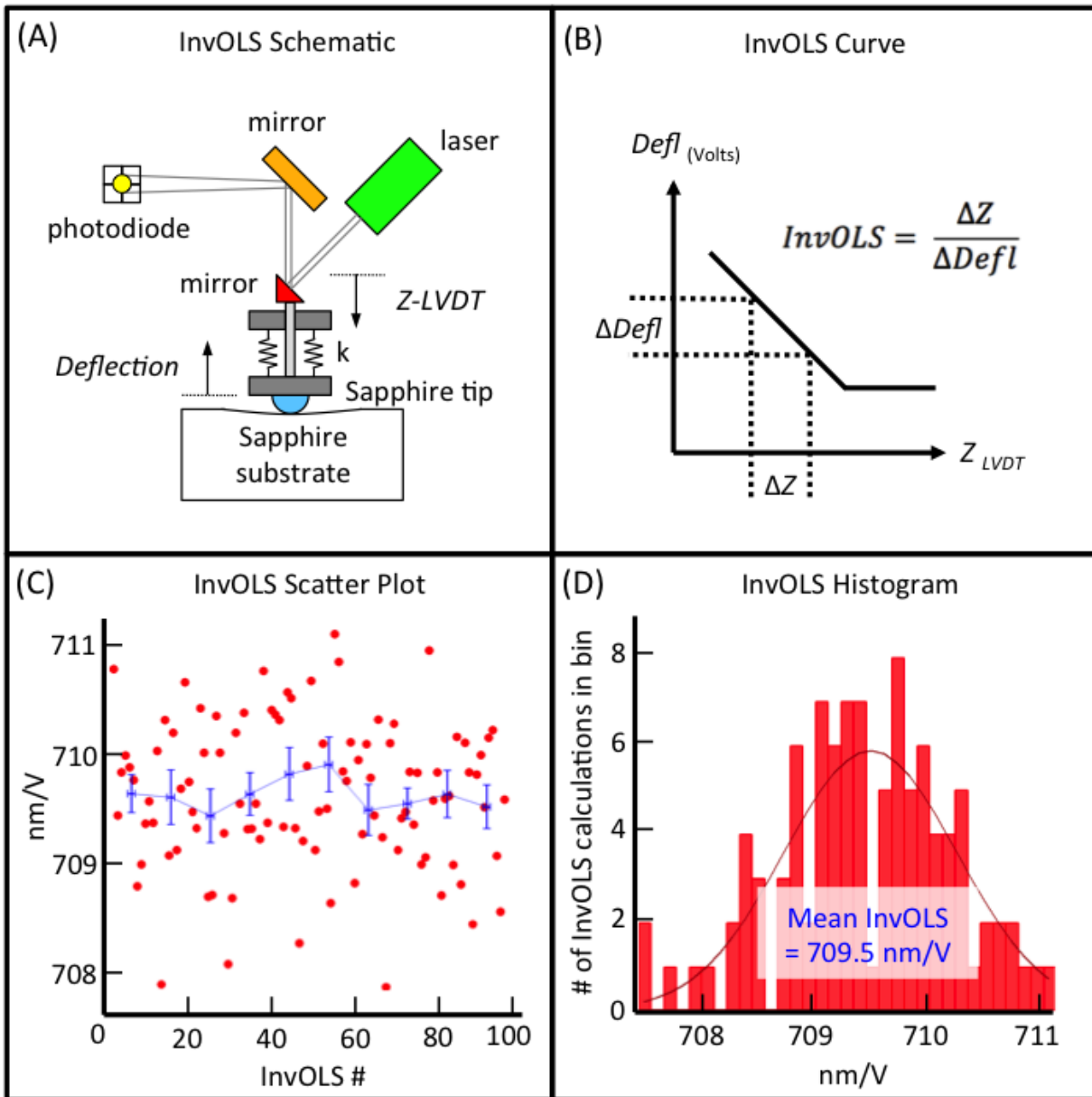


Figure 3-8. Illustrations of the InvOLS calibration. A) Schematic of InvOLS indentation with a spherical indenter. B) Illustration of the InvOLS calibration curve. C) Scatter plot of 100 InvOLS values taken while calibrating for the fracture threshold experiment. (D) Histogram of the InvOLS values with a calculation of the mean InvOLS in nm/V

### 3.8 Locating the Nanoindentations

The AFM scan window for an MFP-3D™, which corresponds to the range of the XY stage piezo, is 90 μm. Optical microscopy is required to obtain an image at larger scales beyond 90 μm. However, ultra-low load (<1 mN) nanoindentations measuring < 200 nm wide are not visible using optical microscopy. Using AFM to locate indents on the 10 x 10 mm square Si substrate used in these experiments would have required ~ 100 million AFM scans. At ~ 10 minutes per scan, this would have been prohibitive.

For this reason, a 0.5 mm scratch that ended within 90 μm of the indentations was scribed across the surface using the nanoindenter. To provide the line with an optically observable thickness, a relatively high load (5 mN) was applied to the indenter as it scribed the line. A Berkovich tip, which is less sharp than a cube corner tip and is used for higher load indentations, was used to create the scratch. The procedure began by placing the Si substrate (attached to an AFM specimen disc) on a magnetic AFM specimen disc holder and inserting into the XY stage using magnetic clips. A synthetic diamond Berkovich indenter tip (Asylum Research) was inserted into the nanoindenter module, which was inserted into the AFM head. Leg extenders were attached to the AFM head to extend the height of the nanoindenter module above the sample. The AFM head was placed on the XY stage and a water bubble level was used to maintain level as the nanoindenter was lowered towards the sample surface.

After scribing the 0.5 mm line from left to right at a load of 5 mN, at approximately the center of the Si substrate, the tip was raised. The XY stage was moved 50 μm to the left, which was equivalent to tip moving 50 μm to the right. The tip was withdrawn and the AFM head was raised and removed from the XY stage. The Berkovich tip was exchanged with a cube corner tip that was later used to create the nanoindentations.

The geometry and appearance of the diamond Berkovich indenter used in this experiment are shown in Figure 3-9.

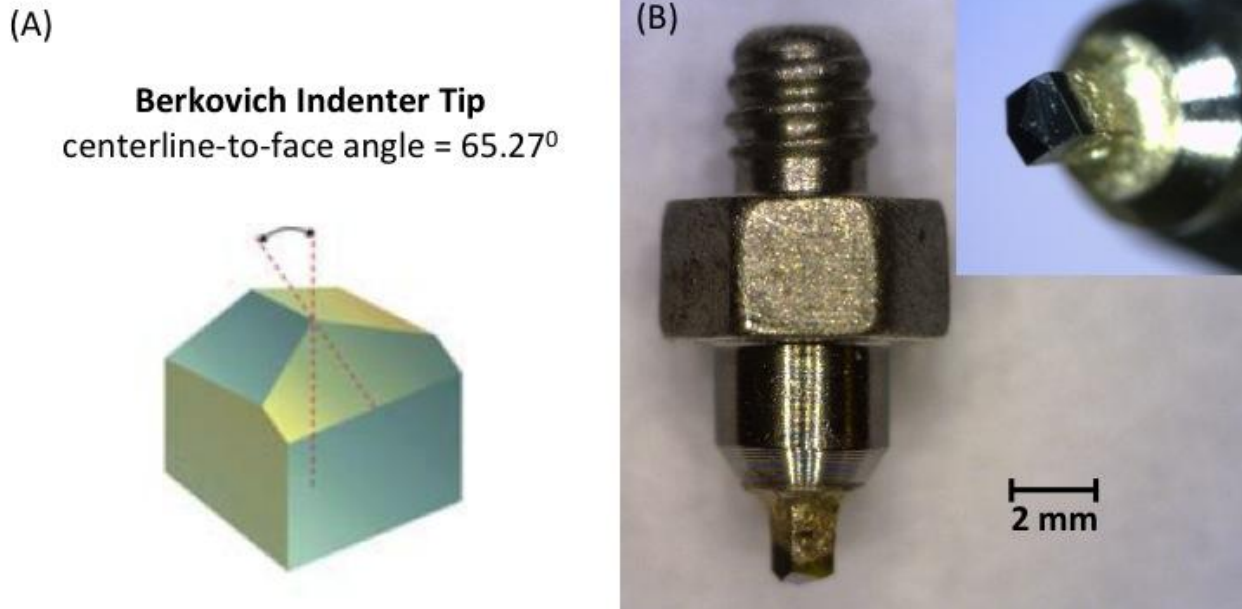


Figure 3-9. Images of the Berkovich indenter tip. A) Illustration of the geometry of a Berkovich tip. B) Optical images of the Berkovich tip used in this study. Photos courtesy of Jared Hann

### 3.9 Scanning the Indents Using Atomic Force Microscopy

To scan the surface, a non-contact cantilever (see section 3.4) was inserted into the cantilever holder and placed in the AFM head, which was lowered onto the Si substrate. First, the inbuilt optical microscope was used to locate the 0.5 mm horizontal (X direction) scratch by rastering across the surface in the Y direction. When the scribed line was found, it was followed towards the right until it ended. This was the location of the nanoindentations, within a  $\sim 90 \mu\text{m}$  region. Here, a  $90 \mu\text{m}$  scan was performed to precisely locate the nanoindentation array.

Before scanning was performed, a thermal tune was performed on the cantilever to acquire the approximate resonant frequency. This provided the user with a frequency range over which to more precisely locate the resonant frequency, using an auto tune,

which scanned between 50 and 400 Hz and found the precise resonant frequency. The resonant frequency varied with each scan and was updated regularly.

After the resonant frequency was located, the phase offset was adjusted to 90 degrees. The target amplitude was set to 1.5 V with an offset of -10 % and the set point voltage was lowered to 1.45 V. Ensuring the cantilever was at least 1 mm above the sample surface, the Z piezo was fully extended (engaged) to 150 V. The AFM head was manually lowered towards the surface until the Z piezo began to retract as evidenced by a decreasing Z voltage. After surface contact was achieved at a midpoint Z voltage of 75 V, the Z piezo was withdrawn, the acoustic enclosure was closed and secured, and further operation was conducted from digital controls only. The Z piezo was re-engaged with the surface, the set point lowered to 1.3 V, and scanning was commenced.

Scanning was performed at a scan speed of 1 Hz and a resolution of 512 scan points and lines. Height, Amplitude, Phase and Z height data was recorded from each scan in both trace and retrace. Raw data was saved, and plane corrected data was shown in the user panel.

### **3.10 Calculating the Maximum Indent Depth From Nanoindentation Data**

Nanoindentation was performed in load control with a data collection rate of 10 points per  $\mu\text{N}$ . The indenter records load and displacement data in the form of a curve, as shown in Figure 3-8. The indenter is first loaded into the material, reaching a maximum depth,  $h_{\text{max}}$ , and then as the indenter is withdrawn, the impression experiences an elastic recovery resulting in a final depth measurement,  $h_{\text{final}}$ . The indent experiences further elastic recovery, and an oxide layer forms on it's surface, which leads to a residual depth, which is measured using AFM scans of the indentation impression (see section 3.13). The maximum depth is measured via nanoindentation.

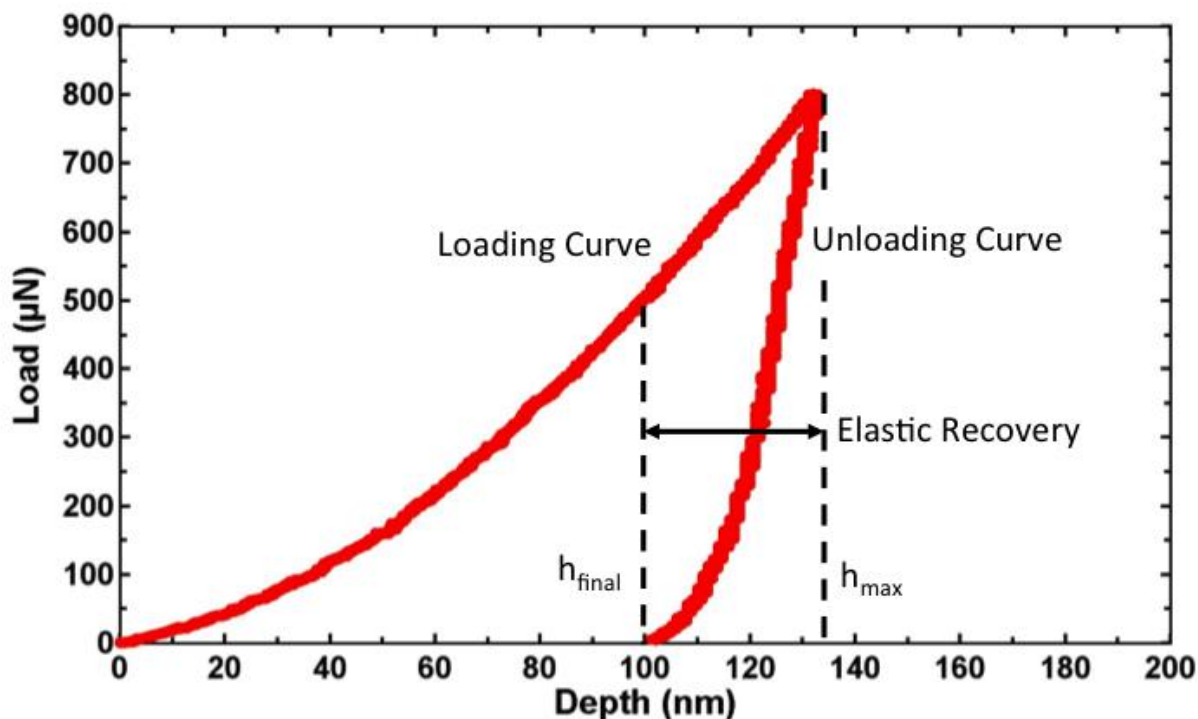


Figure 3-10. Load displacement curve of a 800  $\mu\text{N}$  cube corner indent on Si(100), showing the loading curve, unloading curve, elastic recovery, maximum indent depth ( $h_{\text{max}}$ ) and final indent depth ( $h_{\text{final}}$ )

### 3.11 Post-Processing AFM Data with SPIP™ Software

Scanning Probe Imaging Processor (SPIP™) software (Image Metrology, Inc., Hørsholm, Denmark) was used to post-process AFM images. First, a maximum flatness tilt was applied so that the height distribution histogram maximized the frequency of a dominating height level. Using this procedure, when SPIP™ detected two dominating height levels, it maximized the sum of those two frequencies. At this point, the image contained small surface corrugations, which were dominated by the noise in the system, and created observable steps between successive scan lines. A histogram alignment elevated the individual line profiles so that their height distribution obtained the best match. The mean Z height was set to zero as a reference from which to make indent depth measurements. These procedures are outlined in Figure 3-11.

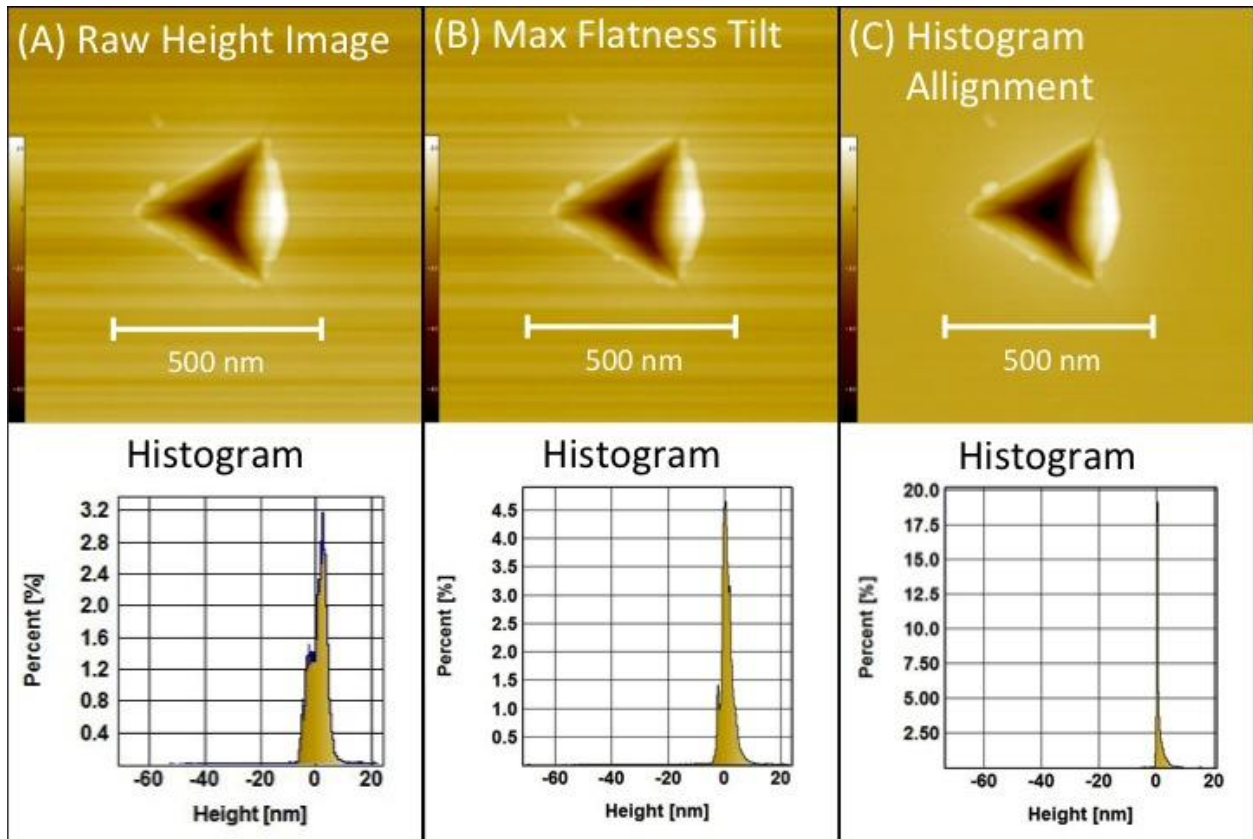


Figure 3-11. AFM images and histogram plots of the post processing procedure applied to indentations in this study. A) Raw height image with a histogram showing a relatively large height distribution. B) Max flatness tilted image, with a histogram plot showing a narrowed height distribution. C) Histogram aligned image with a histogram plot, showing a significantly narrowed height distribution

Profiles of the indents at each stage of post image processing revealed that processing did not affect indent depth measurements (see Figure 3-12).

A 3D visualization was applied to the 2D plane-corrected height images using the SPIP™ 3D visualization tool. The software provides the capability to rotate, translate, and scale the 3D image in all three coordinate axes directions, which aided the visualization of the indent.

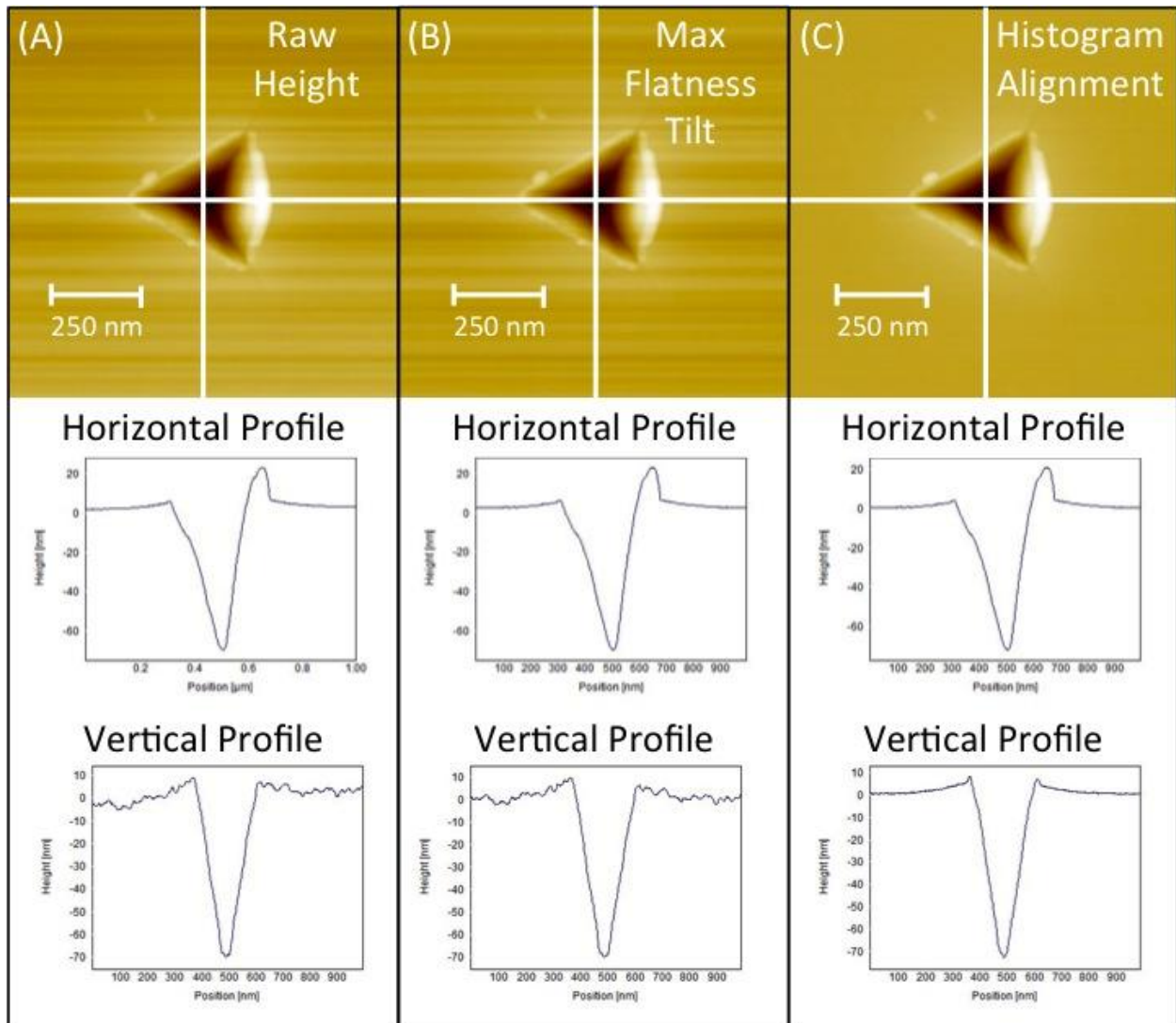


Figure 3-12. AFM scans with horizontal and vertical profiles showing that post processing of images does not affect the depth measurements of indents. A) Raw height image and profiles. B) Max flatness tilted image and profiles. C) Histogram aligned image and profiles

### 3.12 Locating and Measuring Radial Cracks

Radial cracks were located by visual inspection of AFM images of the indentations. Radial cracks were measured by selecting the line profile tool, tracing the radial crack, and recording the x-axis length of the profile line (note: z-axis data in an amplitude image is not related to height). The location and measurement of radial cracks is shown in Figure 3-13.

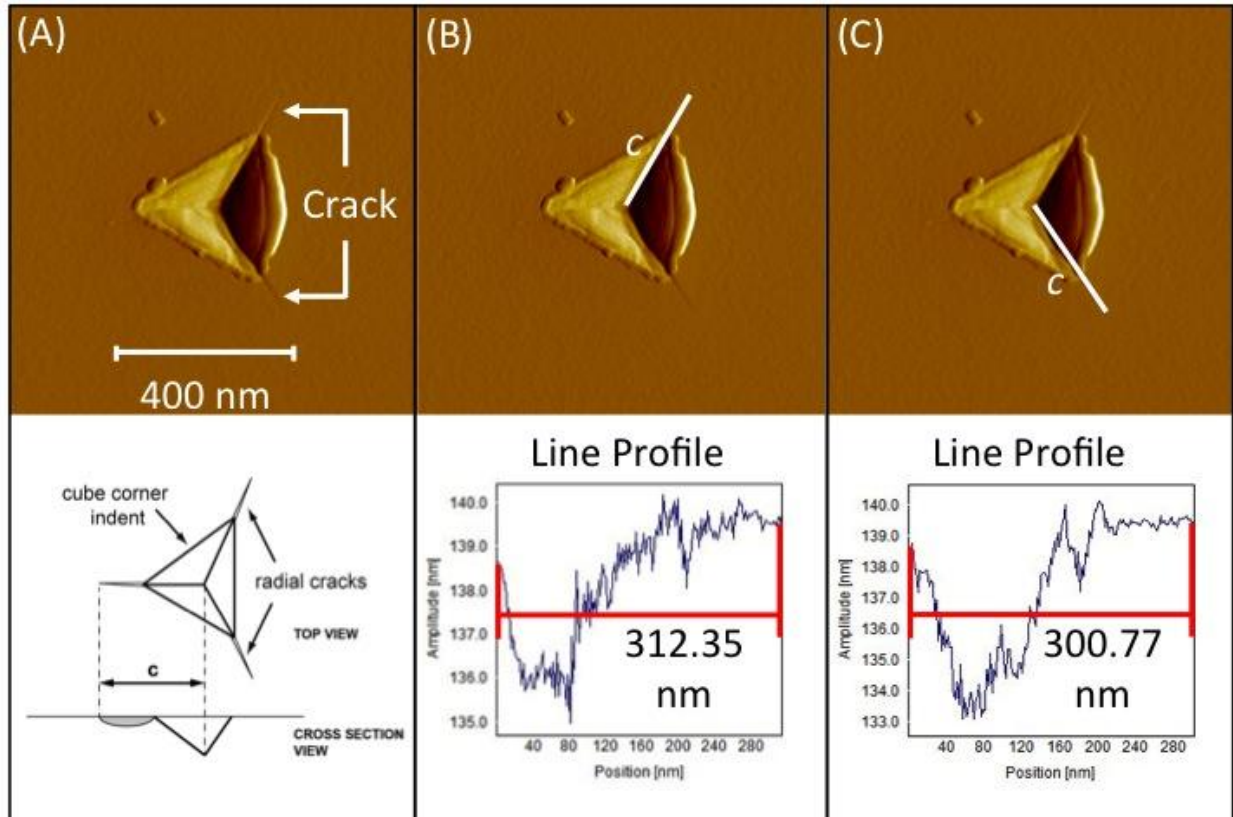


Figure 3-13. Radial crack measurement procedure. A) AFM amplitude image of an indent showing two radial cracks with an illustration of a cross sectional view of a radial crack. B) Measurement of one of the two radial cracks. C) Measurement of the second radial crack

### 3.13 Measuring Residual Indent Depth

Residual indent depth was measured by applying the line profile tool across the indents from corrected AFM height images. The depth of the profile line from each of the triangular vertices to the midpoint of the opposite baseline was recorded and the mean value of these three measurements was calculated. This procedure is illustrated in Figure 3-14. Measurements of indent width were recorded in a similar manner, using three profiles for each indent.

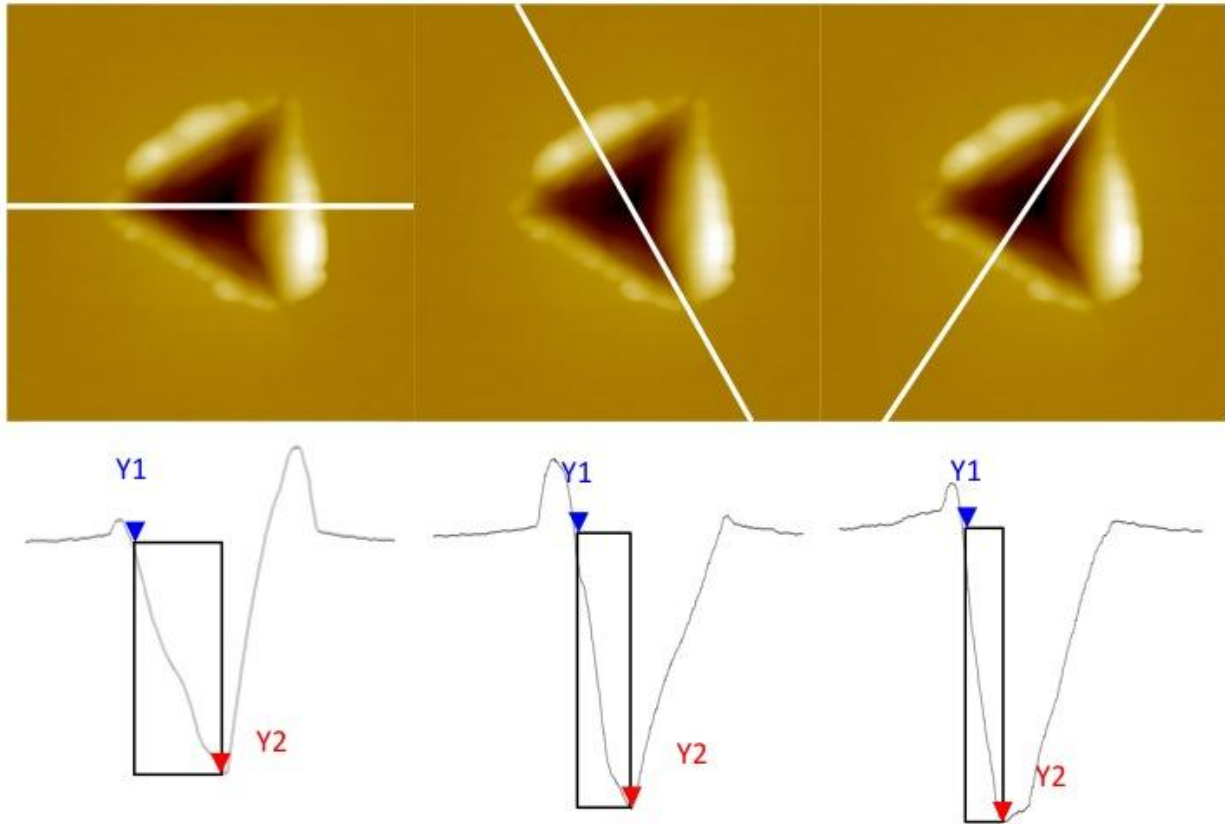


Figure 3-14. Three height images and line profiles of an 800  $\mu\text{N}$  cube corner indent in Si(100). The depth measurement for each indent is taken as the mean value of these three measurements

### 3.14 Cube Corner Tip Metrology

In theory, the cube corner tip has an apex with the geometry of a cube, but in practice, the apex is spherical with a nominal radius. The cube corner used in this study was characterized via AFM metrology. The procedure first involved inserting the cube corner tip into a tip holder that was inserted into the XY stage and secured with magnetic clips, which held the nanoindenter vertical, facing upwards. The AFM module (cantilever holder) was then inserted into the AFM head and lowered onto the XY stage with the cantilever tip positioned above the indenter tip. The tip apex was scanned and processed using SPIP™ software to reveal a tip radius of 32 nm. A collage of pictures outlining the procedure is shown in Figure 3-15.

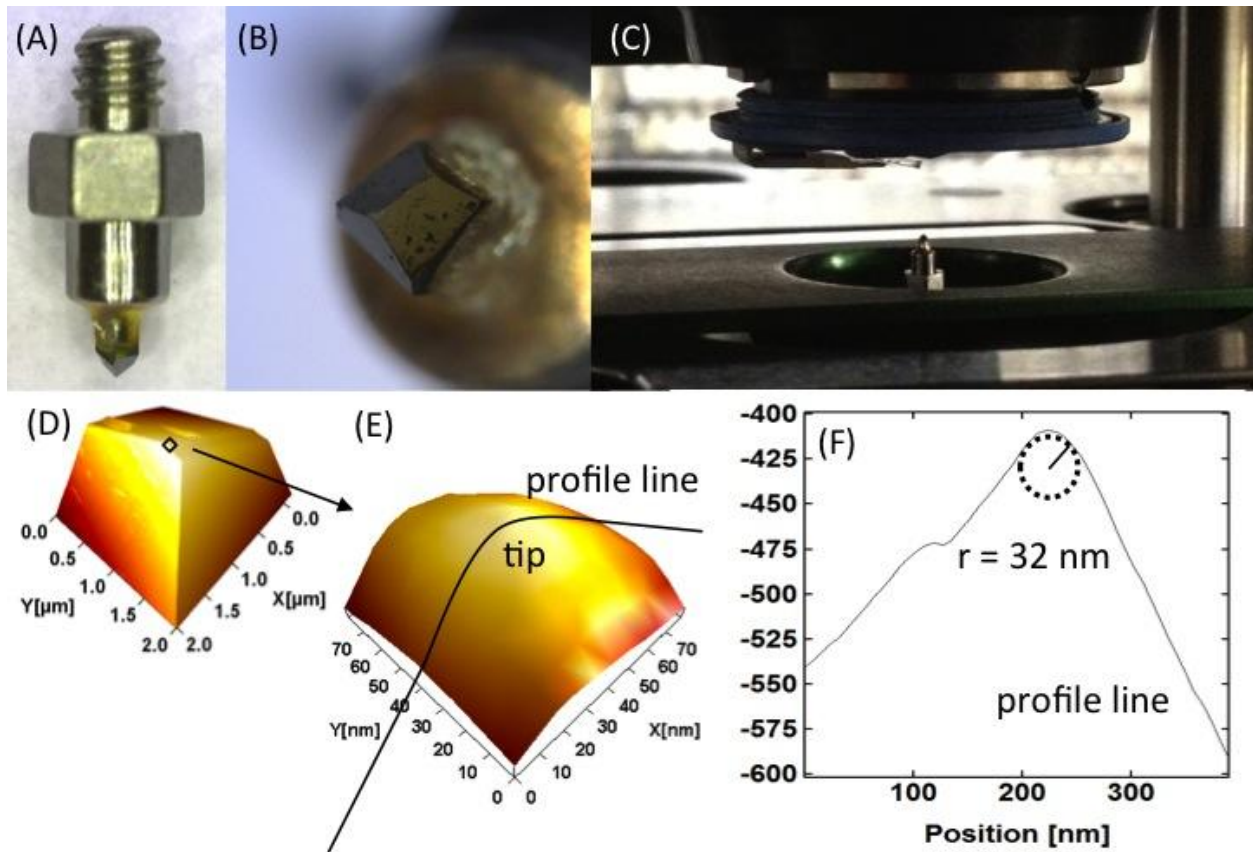


Figure 3-15. Cube corner tip metrology procedure. A) Optical image of the cube corner tip. B) Close view of cube corner tip. C) Photograph of AFM cantilever above cube corner tip before scanning. D) 3D visualization of cube corner tip. E) 70  $\mu\text{m}$  3D visualization of cube corner tip, showing a profile line across tip surface. F) Profile of cube corner tip showing the radius. Photos courtesy of Jared Hann

## CHAPTER 4 FRACTURE THRESHOLD EXPERIMENT

### 4.1 Overview

This chapter details the methods, results, discussion and conclusion of the experiment to determine the fracture threshold for a single, isolated nanoindentation in Si(100) using a diamond cube corner indenter tip.

### 4.2 Calibration and Preparation

The nanoindenter was calibrated with a virtual deflection calibration as outlined in section 3.5, then an InvOLS calibration using the procedure in section 3.6. After nanoindentation calibrations were completed, the 10 x 10 mm Si(100) substrate was cut, cleaned and checked for particulates as described in section 3.2. A 0.5 mm line was scribed at a 5 mN load using a Berkovich indenter as described in section 3.8. After these preparatory steps, the nanoindentation arrays were performed with a cube corner indenter tip.

### 4.3 Nanoindentation Array

This experiment was designed to determine the fracture threshold load when using a cube corner indenter tip ( $r \sim 32$  nm) in Si(100). The experimental plan was to perform indentation over a wide range of loads and then scan with AFM to visually identify the load at which cracking first occurs. By narrowing the range of loads over which indentation was performed, and scanning each indent with AFM, the fracture threshold load was determined within a very precise range (10 mN). The procedure for performing the first of these nanoindentation arrays is outlined.

The cube corner indenter was inserted into the nanoindenter module, which was attached to the AFM head. The AFM head was lowered onto the Si sample, which

remained unmoved from the Berkovich scratch to ensure a contact with close proximity ( $< 90 \mu\text{m}$ ) to the final Berkovich tip withdrawal. Indentations were performed under load control at maximum loads of  $1 \mu\text{N}$ ,  $2 \mu\text{N}$ ,  $3 \mu\text{N}$ ,  $4 \mu\text{N}$ ,  $5 \mu\text{N}$ ,  $10 \mu\text{N}$ ,  $20 \mu\text{N}$ ,  $30 \mu\text{N}$ ,  $40 \mu\text{N}$ ,  $50 \mu\text{N}$ ,  $100 \mu\text{N}$ ,  $200 \mu\text{N}$ ,  $400 \mu\text{N}$ ,  $600 \mu\text{N}$ ,  $800 \mu\text{N}$ ,  $1 \text{ mN}$ ,  $1.2 \text{ mN}$ ,  $1.4 \text{ mN}$ ,  $1.6 \text{ mN}$ ,  $1.8 \text{ mN}$ ,  $2 \text{ mN}$ ,  $4 \text{ mN}$ ,  $6 \text{ mN}$ ,  $8 \text{ mN}$ , and  $10 \text{ mN}$ . The loading function for each indent consisted of a 5 second load, 2 second hold, and 5 second unload. Indentation was performed with a start distance of  $5.26 \mu\text{m}$ , force distance of  $500 \text{ nm}$ , and velocity of  $100 \text{ nm/s}$ . The trigger was set to force and adjusted according to the maximum indent load. For  $1\text{-}10 \mu\text{N}$  indents the trigger was set to  $1 \mu\text{N}$ . For  $20 \mu\text{N} - 10 \text{ mN}$  indents, the trigger was set to  $5 \mu\text{N}$ . Each indent was performed on a 5 by 5 grid of 25 indents, each separated by  $10 \mu\text{m}$ , creating a total array size of  $40 \mu\text{m}^2$ . A schematic of the indentation array is shown in Figure 4-1.

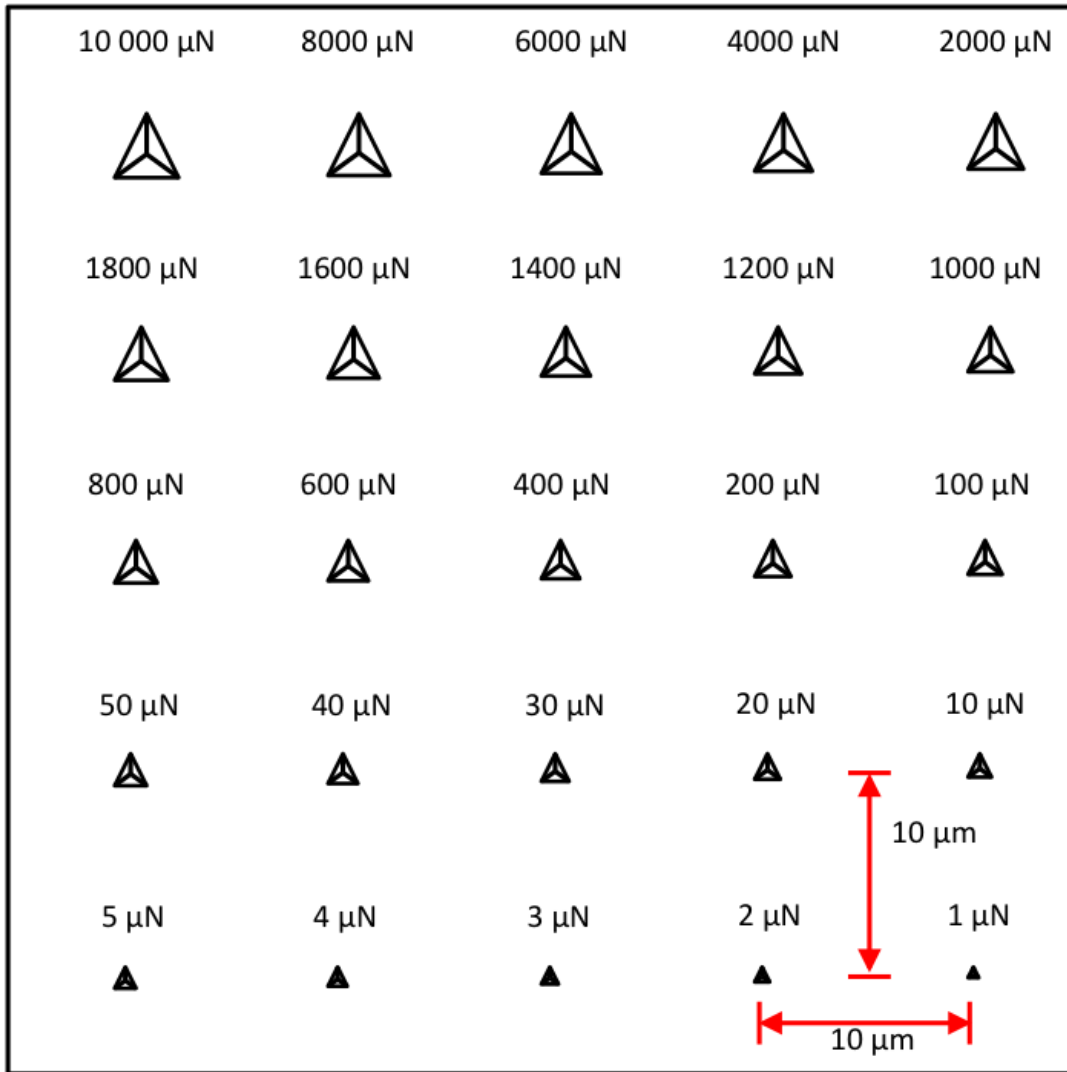


Figure 4-1. Schematic of the nanoindentation array for determination of the single indentation fracture threshold in Si(100) using a cube corner indenter. The load range for this array was 1  $\mu\text{N}$  – 10 000  $\mu\text{N}$

The 1  $\mu\text{N}$  – 10 mN array was scanned using a VISTAprobes™ T300R (Nanoscience Instruments, Inc., Phoenix, AZ, USA) non-contact mode AFM probe with <10 nm tip radius. AFM scanning was performed using the procedure outlined in section 3.7. A selection of the processed images of these indentations is shown in Figure 4-2.

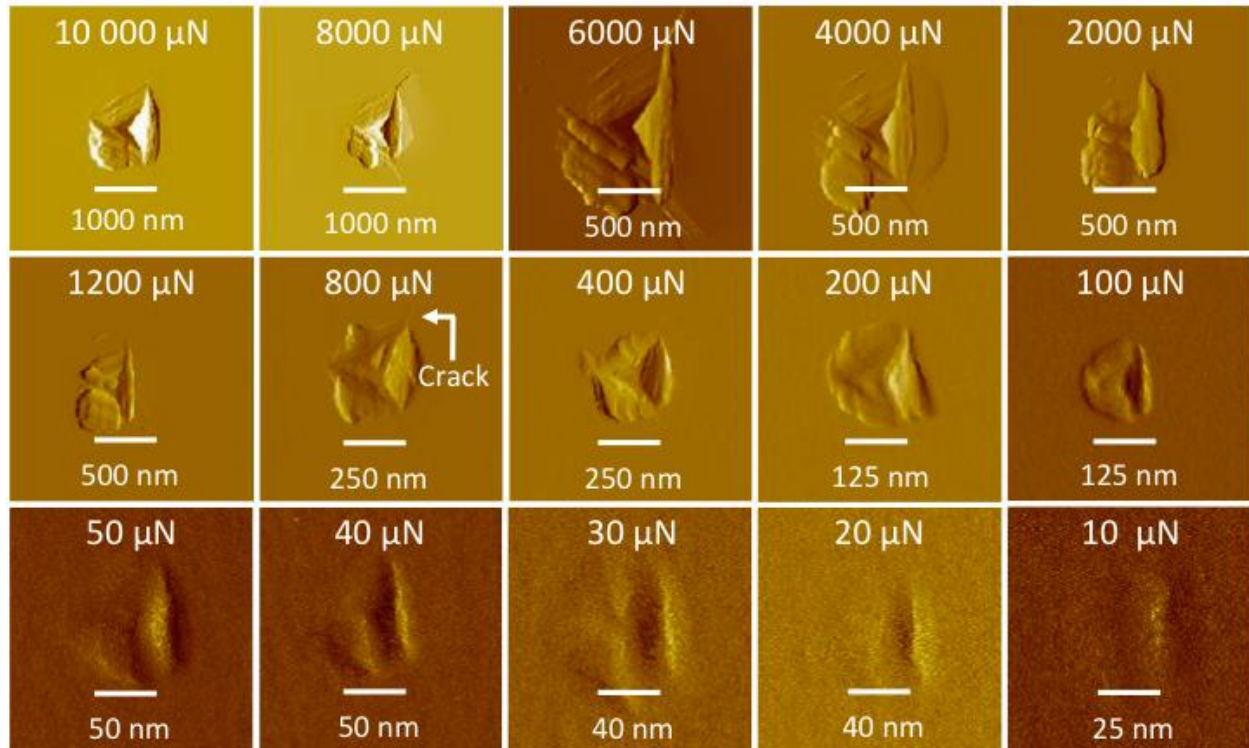


Figure 4-2. Selected AFM amplitude images of 1  $\mu\text{N}$  – 10 000  $\mu\text{N}$  cube corner nanoindentations in Si(100). The fracture threshold occurs within the 200  $\mu\text{N}$  – 800  $\mu\text{N}$  range

AFM images from the 1  $\mu\text{N}$  – 10 000  $\mu\text{N}$  range indentation array show no evidence of a radial crack  $\leq$  200  $\mu\text{N}$ , but a 320 nm crack is observed at 800  $\mu\text{N}$ . Thus, results indicate that the fracture threshold occurred between 200  $\mu\text{N}$  and 800  $\mu\text{N}$ . Subsequent indentation was conducted across the 200  $\mu\text{N}$  – 800  $\mu\text{N}$  load range at intervals of 50  $\mu\text{N}$  to locate the fracture threshold load with greater precision.

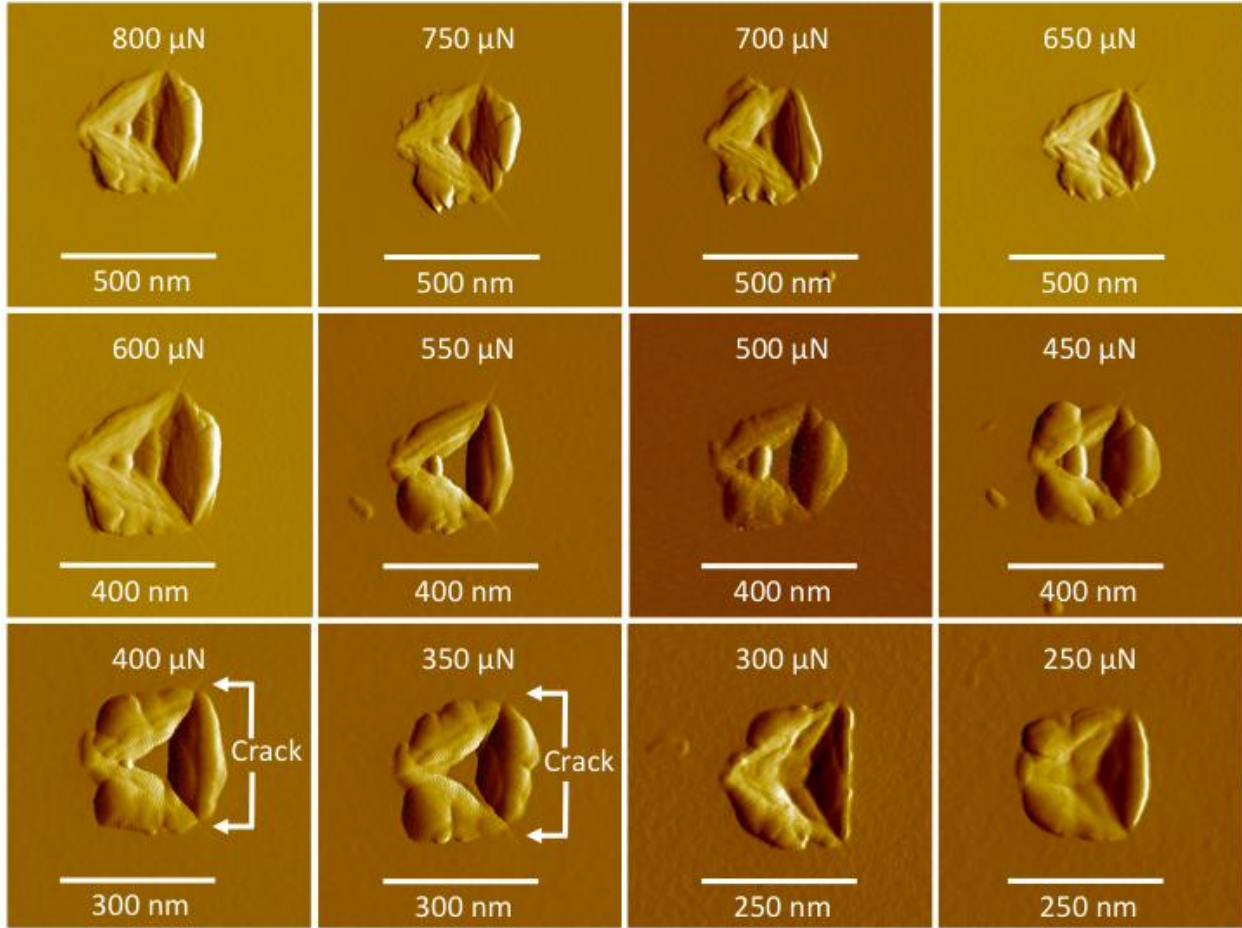


Figure 4-3. AFM amplitude images of 250  $\mu\text{N}$  – 800  $\mu\text{N}$  cube corner nanoindentations in Si(100). The fracture threshold occurs within the (250  $\mu\text{N}$  – 400  $\mu\text{N}$ ) range

AFM images from the 200  $\mu\text{N}$  – 800  $\mu\text{N}$  range indentation array show two radial cracks in the 400  $\mu\text{N}$  indentation, two radial cracks in the 350  $\mu\text{N}$  indentation, and no radial crack below 250  $\mu\text{N}$ .

Subsequent indentation was conducted across the 200  $\mu\text{N}$  – 400  $\mu\text{N}$  load range, to ensure coverage across the fracture threshold, at intervals of 10  $\mu\text{N}$  to locate the fracture threshold load with greater precision. Each load was repeated 5 times for statistical significance, at a separation of 5  $\mu\text{m}$ . This resulted in a total of 105 indents. All indents were conducted at a loading rate of 200  $\mu\text{N/s}$ . The InvOLS for this experiment was calculated to be 711.57  $\text{nm/V}$ . Each indent was conducted at a start distance of

5.26  $\mu\text{m}$ , a force distance of 500 nm, a velocity of 100 nm/s, and with a 5  $\mu\text{N}$  force trigger. A schematic of the 200  $\mu\text{N}$  – 400  $\mu\text{N}$  array is shown in Figure 4-4.

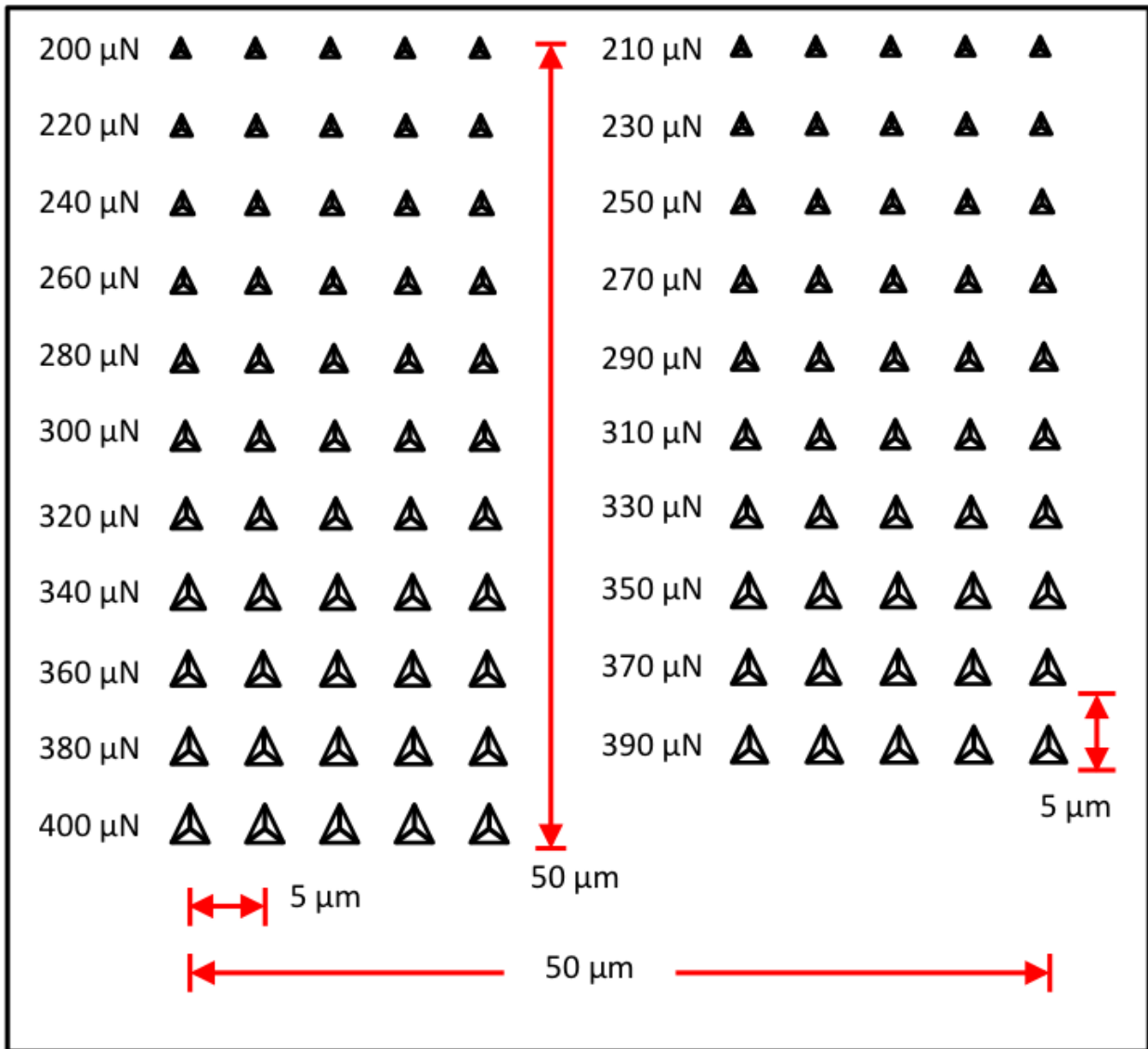


Figure 4-4. Schematic of the nanoindentation array for the determination of the single indentation fracture threshold in Si(100) using a cube corner indenter. The load range for this array was 200  $\mu\text{N}$  – 400  $\mu\text{N}$

The 200  $\mu\text{N}$  – 400 mN array was scanned using the procedure given in 3.7. Each indent was scanned in a 500 x 500 nm window.

#### 4.4 Results

Selected AFM amplitude images from the 200  $\mu\text{N}$  – 400  $\mu\text{N}$  nanoindentation array are shown in Figure 4-5.

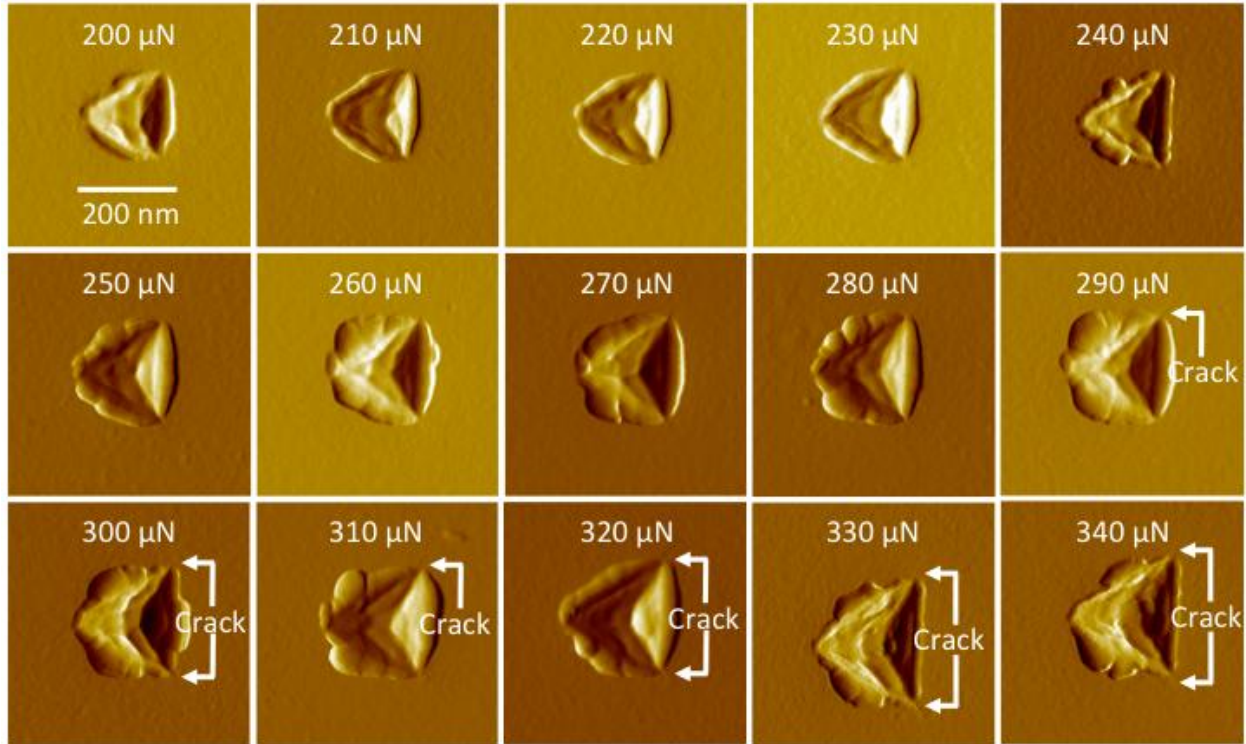


Figure 4-5. Selected AFM amplitude images of nanoindentations from the 200  $\mu\text{N}$  – 400  $\mu\text{N}$  array with radial cracks identified

Visual inspection of the amplitude images from the AFM scans of the 200  $\mu\text{N}$  – 400  $\mu\text{N}$  indents revealed cracks in a 290  $\mu\text{N}$  indent but no cracks below this load. This indicated that fracture occurred within the 280  $\mu\text{N}$  – 290  $\mu\text{N}$  range. Therefore, the fracture threshold for a single, isolated, cube corner (radius~32 nm) indenter in Si(100) is 280  $\mu\text{N}$  – 290  $\mu\text{N}$ . Enlarged AFM images of 280  $\mu\text{N}$  and 290  $\mu\text{N}$  indents are shown in Figure 4-6.

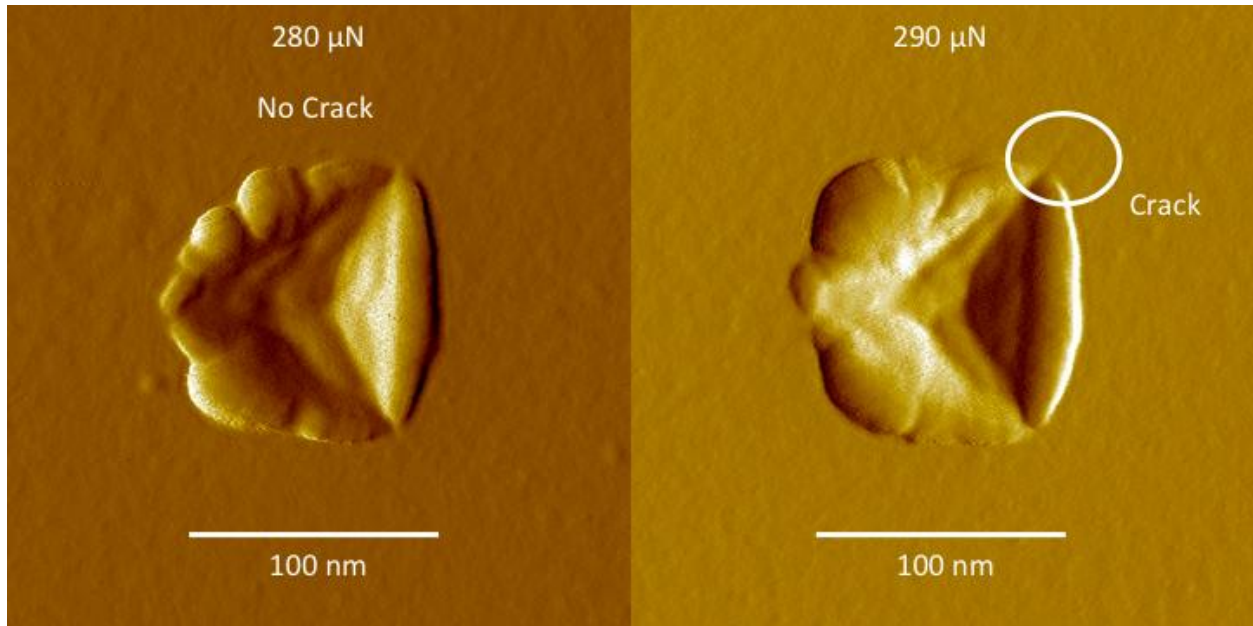


Figure 4-6. AFM amplitude images of a 280  $\mu\text{N}$  indent showing no crack, and a 290  $\mu\text{N}$  indent showing a crack. The threshold load is 280  $\mu\text{N}$  – 290  $\mu\text{N}$

Following the location of the fracture threshold load, the residual depth was measured via AFM metrology, using the procedure outlined in section 3.10. The residual indent depth ( $h_{\text{res}}$ ) was plotted as a function of load, superimposed with a plot of maximum indent depth ( $h_{\text{max}}$ ), and recorded as described in section 3.8. Depth vs. load and width vs. load plots are provided in Figure 4-7.

As indicated by the load vs. indent depth plot in Figure 4-7, indentation unloading is accompanied by elastic recovery of the material. Furthermore, there is a growth of an oxide layer in the indent, which also contributes to a decrease in indent depth. This leads to a difference between maximum depth and the residual depth measured via AFM metrology. The width vs. residual indent depth ratio is between 4.65 and 7.28 for indents between 200  $\mu\text{N}$  and 400  $\mu\text{N}$ .

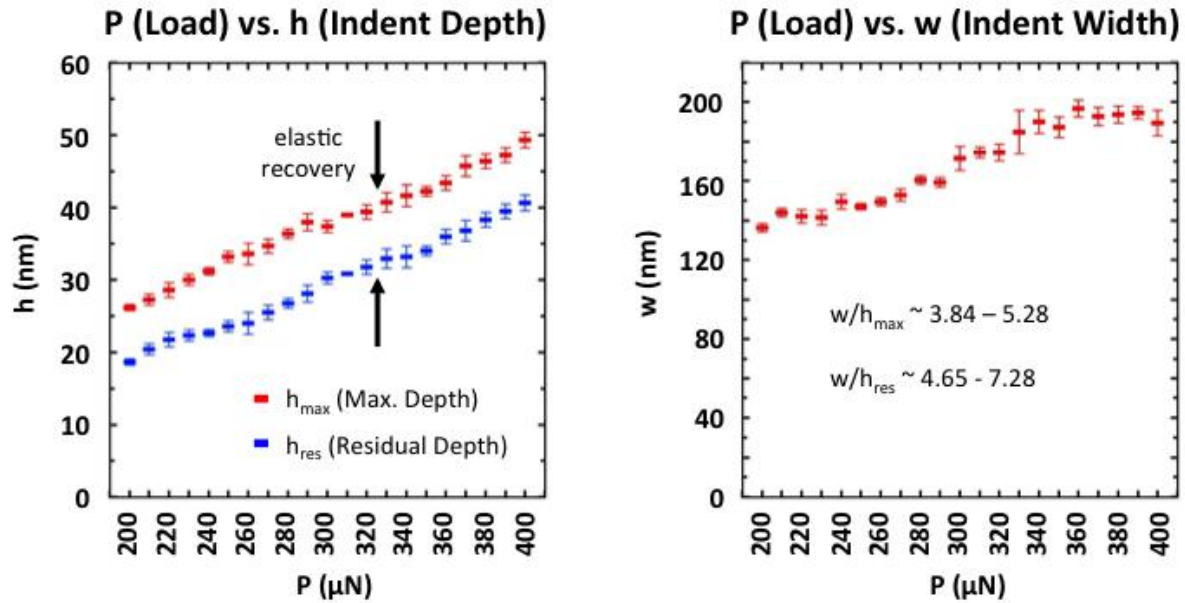


Figure 4-7. Plots of indent depth vs. indent load and indent width vs. indent load. Error bars represent one standard deviation from the mean (of measurements from 5 indents)

#### 4.5 Discussion

Lawn, et al. (1977)<sup>23</sup> predicted a fracture threshold of 3000  $\mu\text{N}$  for a Vickers indentation in Si. However, nanoscale indenters can generate higher concentrated stresses than Vickers indenter. For example, Harding, et al. (1995)<sup>30</sup> reported a threshold load of 500  $\mu\text{N}$  – 1500  $\mu\text{N}$  for a cube corner indenter in Si(100). The fracture threshold load in this experiment (280  $\mu\text{N}$  – 290  $\mu\text{N}$ ) represents a lower fracture threshold than previously reported in the literature. It also represents a more focused approach, with indentations performed at 10  $\mu\text{N}$  intervals, and an entire study focused on cube corner (nanoscale) indentation in Si(100). A comparison of the fracture threshold result from this study and previous threshold loads reported in the literature is shown in Figure 4-11.

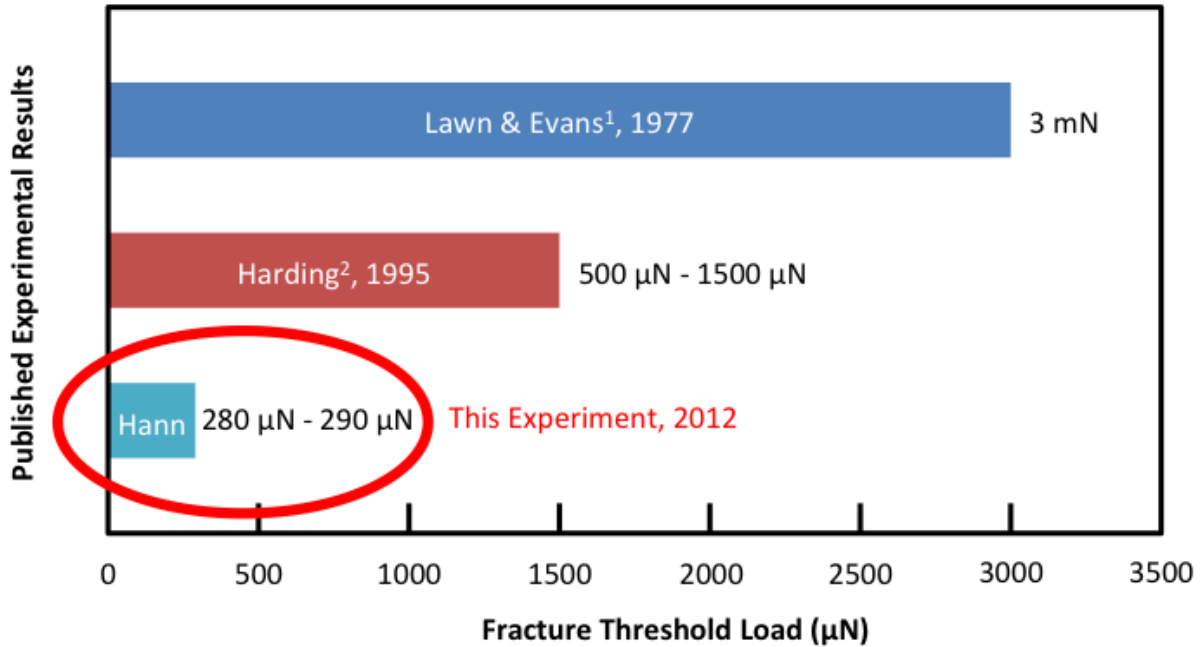


Figure 4-8. Comparison of fracture threshold values reported in the literature and the results of this study

Our experimentally determined fracture threshold (280 µN – 290 µN) for a single, isolated indentation is used as a reference from which to compare the effects of cyclic and adjacent indentation. It is hypothesized that adjacent indents and cyclic loaded indents may cause fracture below the single, isolated indentation fracture threshold load.

## CHAPTER 5 ADJACENT INDENTATION EXPERIMENT

### 5.1 Overview

In this chapter, adjacent indentation pairs are performed as a function of maximum load and indent separation. AFM metrology is conducted by inspecting indent images for evidence of fracture below the threshold. Indents are characterized via depth and crack length measurements, which are plotted against maximum load and indent separation for the observation of correlations between these parameters. Von Mises stress field contours provide a qualitative visualization of interacting elastic stress fields from adjacent indentations.

### 5.2 Calibration and Preparation

The nanoindenter was calibrated with a virtual deflection calibration as outlined in section 3.5, then an InvOLS calibration using the procedure in section 3.6. After nanoindentation calibrations were completed, the 10 x 10 mm<sup>2</sup> Si(100) substrate was cut, cleaned and checked for particulates as described in section 3.2. A 0.5 mm line was scribed at a 5 mN load using a Berkovich indenter as described in section 3.8. After these preparatory steps, the nanoindentation arrays were performed with a cube corner indenter tip.

### 5.3 Adjacent Nanoindentation Array

Indentations were performed with a cube corner indenter on Si(100) at 50  $\mu\text{N}$ , 200  $\mu\text{N}$ , and 800  $\mu\text{N}$ . 50  $\mu\text{N}$  adjacent indents represented adjacent abrasive contacts in the magnetic assisted finishing (MAF) process which contact the surface with ultra-low loads imparted by the magnetic field. Fracture at this load would indicate that adjacent diamond abrasive contacts in MAF were also capable of causing fracture. This would

indicate that fracture would be a possible material removal mechanism in MAF. It would also prove a significant limitation to the indentation fracture model in not addressing adjacent contacts. If fracture were observed at this load, it would be evidence of a stress field interaction between adjacent indentations.

200  $\mu\text{N}$  indents represented contacting close to, but below the fracture threshold. Fracture at this load would indicate a stress field interaction between adjacent indentations.

800  $\mu\text{N}$  indents represented contacting above the fracture threshold. Fracture was expected at this load. By indenting above the fracture threshold, the radial cracks extending from indentation corners could be measured as a function of indent spacing.

Due to the effect of load on indent size, adjacent indents were separated as a normalized function of indent size, represented by the indent radius,  $a$ . The separation distances selected for each load were; zero (repeated indent),  $1a$ ,  $2a$ ,  $5a$ , and  $10a$ . Measurements of the indent radii of 50  $\mu\text{N}$ , 200  $\mu\text{N}$ , and 800  $\mu\text{N}$  indents are shown in Figure 5-1.

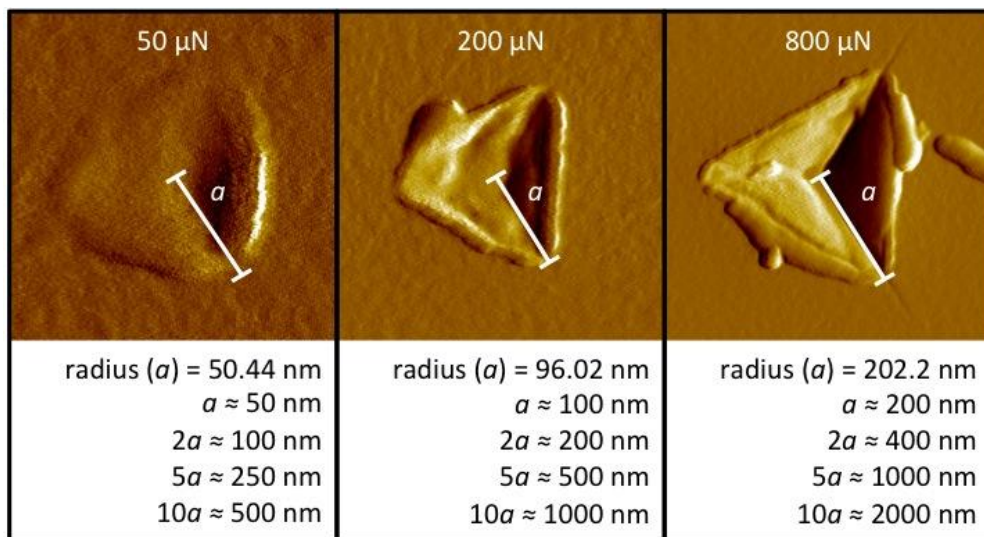


Figure 5-1. AFM images of indent radius measurements for 50  $\mu\text{N}$ , 200  $\mu\text{N}$ , and 800  $\mu\text{N}$  indents

Each adjacent indent pair was repeated 5 times for statistical significance. The result was; 3 maximum loads, 2 indents in each pair, 5 different separations, and 5 copies of every indent pair, for a total of 150 indents

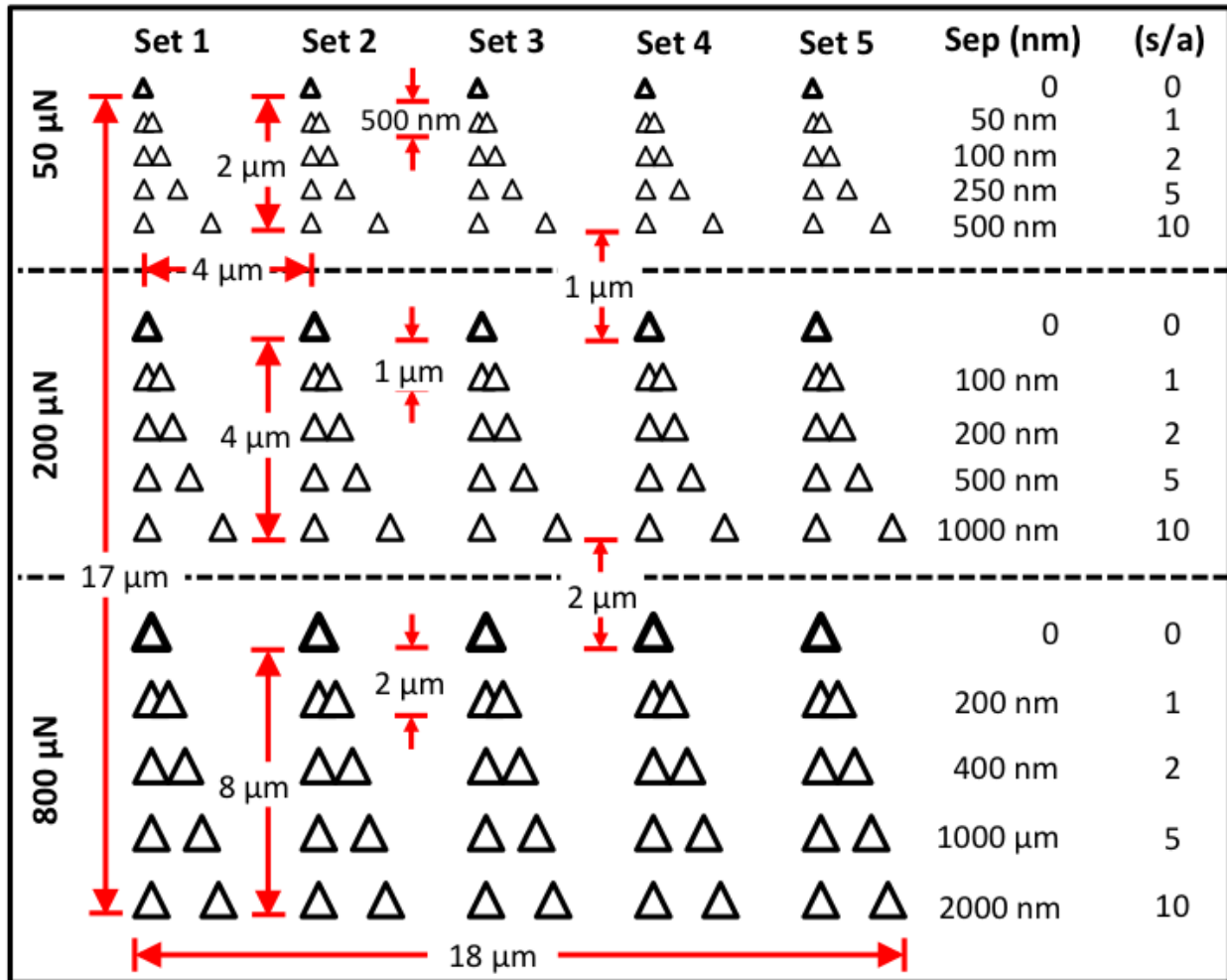


Figure 5-2. Schematic of the adjacent indentation array (not to scale)

50  $\mu\text{N}$  indents pairs were separated from other 50  $\mu\text{N}$  indent pairs by 500 nm. This corresponded to the maximum separation distance of  $10a$  for 50  $\mu\text{N}$  indents, which represented the separation at which there is no interaction between indents. 200  $\mu\text{N}$  indents were separated by 1  $\mu\text{m}$ , which represented infinite separation (no interaction) for indents at this load. 800  $\mu\text{N}$  indent pairs were separated by other indent pairs by 2

$\mu\text{m}$ , which represented infinite spacing for that load. Each set of indents at a particular load were separated from all other sets of indents of the same load by  $4\ \mu\text{m}$ , which was twice the distance considered to be infinite spacing for the highest load.

Indentations were performed under load control. The loading function for each indent consisted of a 5 sec load, 2 sec hold, and 5 sec unload. Indentation was performed with a start distance of  $5.26\ \mu\text{m}$ , force distance of  $500\ \text{nm}$ , and velocity of  $100\ \text{nm/s}$ . The trigger was set to force and maintained at  $5\ \mu\text{N}$  for all indents. Maximum indent depth was recorded for every indent using load displacement data from the nanoindenter. An illustration of the adjacent indent array is shown in Figure 5-2.

AFM was performed using the procedure outlined in section 3.7. Indents were scanned using an SSS-NCH SuperSharpSilicon™ (Nanosensors™) non-contact mode AFM probe with  $\sim 2\text{-}10\ \text{nm}$  tip radius. Post image processing was conducted on the indents using the methodology described in section 3.8. Indent radial crack length was measured from AFM amplitude images using the methodology described in section 3.9. Processed AFM height images of each indent were measured to record residual indent depth using the methodology detailed in section 3.10.

## 5.4 Results

Visual inspection of AFM amplitude images of every indent in the adjacent indentation array revealed that there were no cracks below the single, isolated fracture threshold reported in Chapter 4 ( $280\ \mu\text{N} - 290\ \mu\text{N}$ ). A selection of adjacent indents, representative of the five indent separation distances, are shown in Figure 5-3 as a function of load and indent separation.

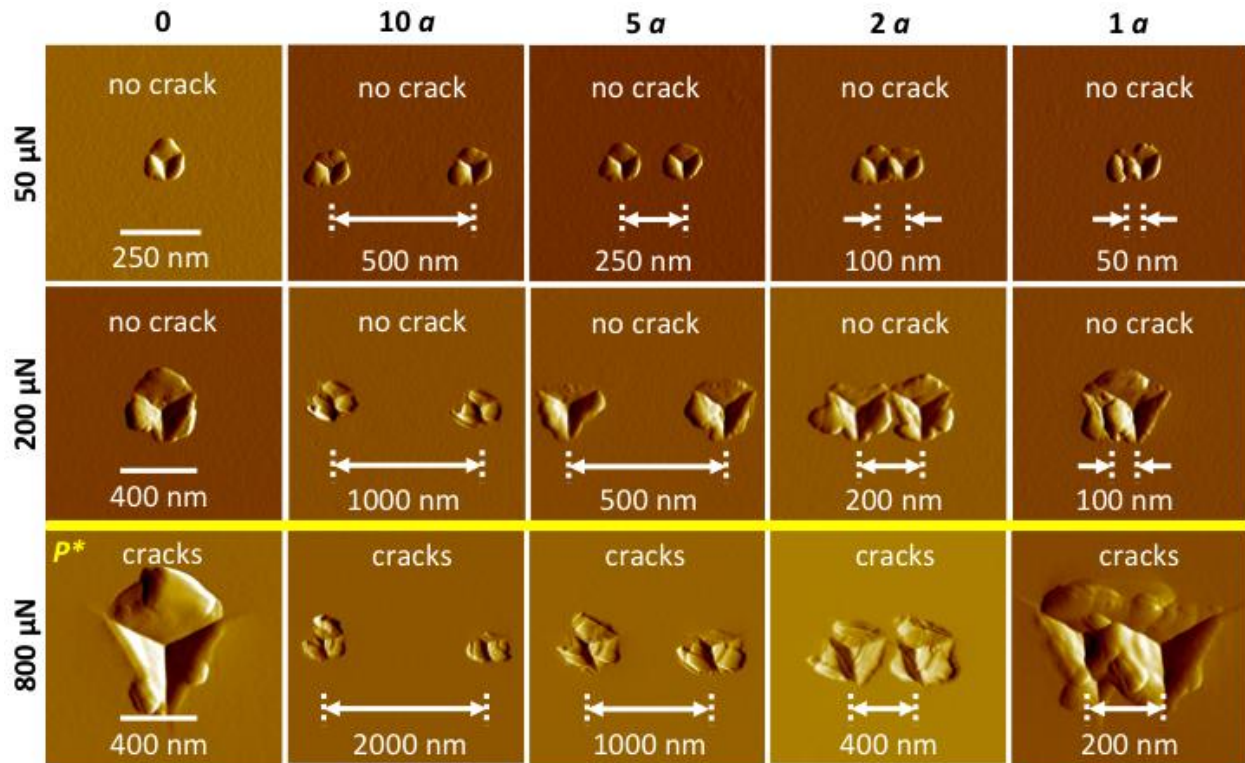


Figure 5-3. A selection of AFM amplitude images of the adjacent indentation array shown as a function of load and indent separation. Initial (first) indents are on the left of each pair and second indents are on the right. The yellow line represents the fracture threshold load,  $P^*$ , above which cracks are visible and below which there are no cracks

A selection of AFM amplitude images representing each indent separation from the 50  $\mu\text{N}$  adjacent indentation pairs are shown in Figure 5-4. The separation is shown in both absolute and normalized form. Below the AFM images of each indentation pair, measurements of initial (first) and second indents are plotted as a function of experimental number (identical repeats of each pair). Maximum depth ( $h_{\text{max}}$ ) vs. experimental number is plotted as a function of indent separation, below a selected AFM image of that indent separation pair. Residual depth ( $h_{\text{res}}$ ) vs. experimental number is plotted as a function of indent separation, below the maximum depth plot of the same indent separation pair.

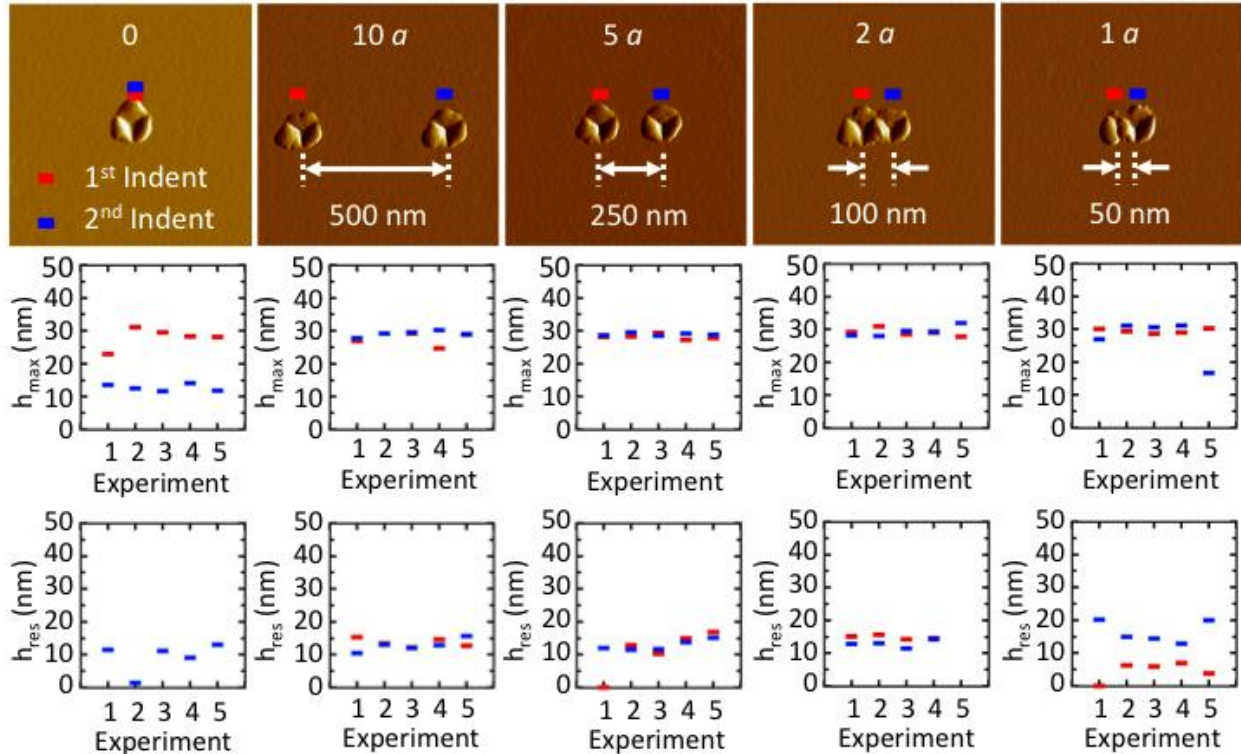


Figure 5-4. 50  $\mu\text{N}$  adjacent indent amplitude images with maximum depth and residual depth measurements. Data from the five repeats (experiments) of each indentation condition are provided

A selection of AFM amplitude images representing each indent separation from the 200  $\mu\text{N}$  adjacent indentation pairs are shown in Figure 5-5. The separation is shown in both absolute and normalized form. Below the AFM images of each indentation pair, measurements of initial (first) and second indents are plotted as a function of experimental number (identical repeats of each pair). Maximum depth ( $h_{\max}$ ) vs. experimental number is plotted as a function of indent separation, below a selected AFM image of that indent separation pair. Residual depth ( $h_{\text{res}}$ ) vs. experimental number is plotted as a function of indent separation, below the maximum depth plot of the same indent separation pair.

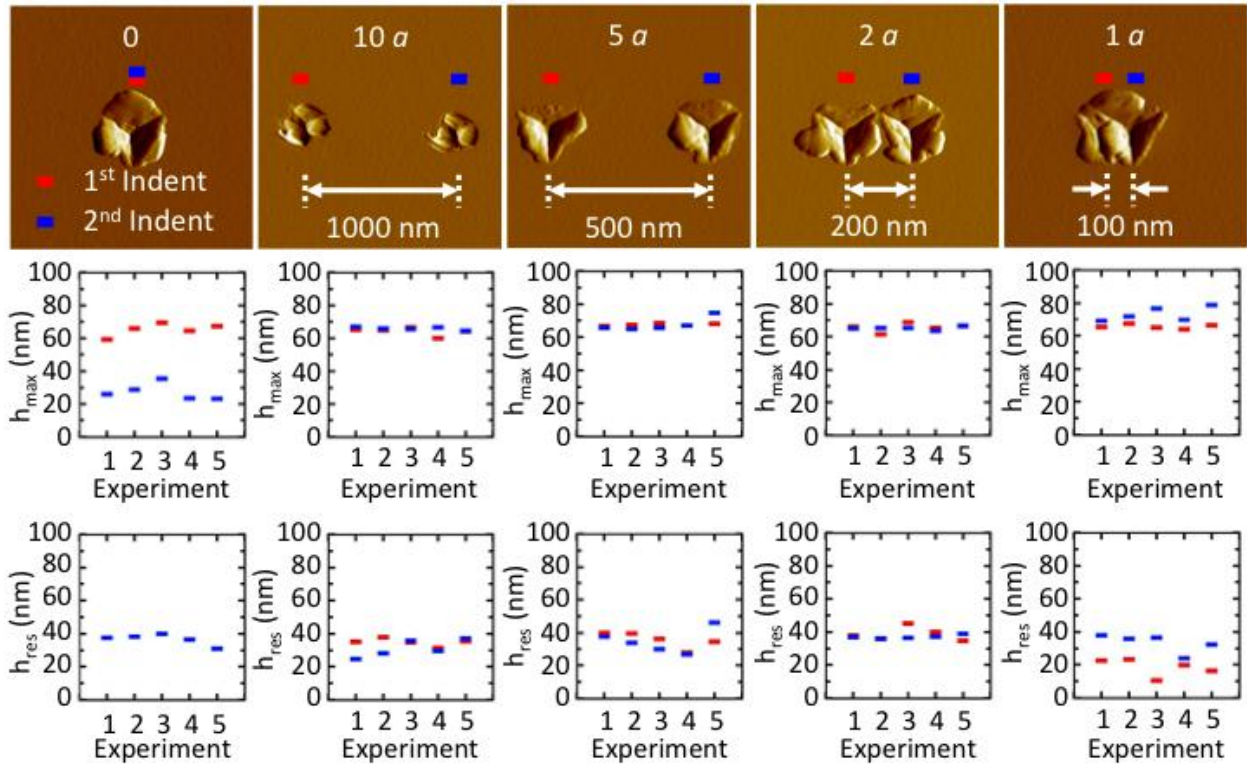


Figure 5-5. 200  $\mu\text{N}$  adjacent indent amplitude images with maximum depth and residual depth measurements. Data from the five repeats (experiments) of each indentation condition are provided

A selection of AFM amplitude images representing each indent separation from the 800  $\mu\text{N}$  adjacent indentation pairs are shown in Figure 5-6. The separation is shown in both absolute and normalized form. Below the AFM images of each indentation pair, measurements of initial (first) and second indents are plotted as a function of experimental number (identical repeats of each pair). Maximum depth ( $h_{\text{max}}$ ) vs. experimental number is plotted as a function of indent separation, below a selected AFM image of that indent separation pair. Residual depth ( $h_{\text{res}}$ ) vs. experimental number is plotted as a function of indent separation, below the maximum depth plot of the same indent separation pair. Because 800  $\mu\text{N}$  is above the fracture threshold load, cracks appear in each image. Crack length is plotted for each separation.

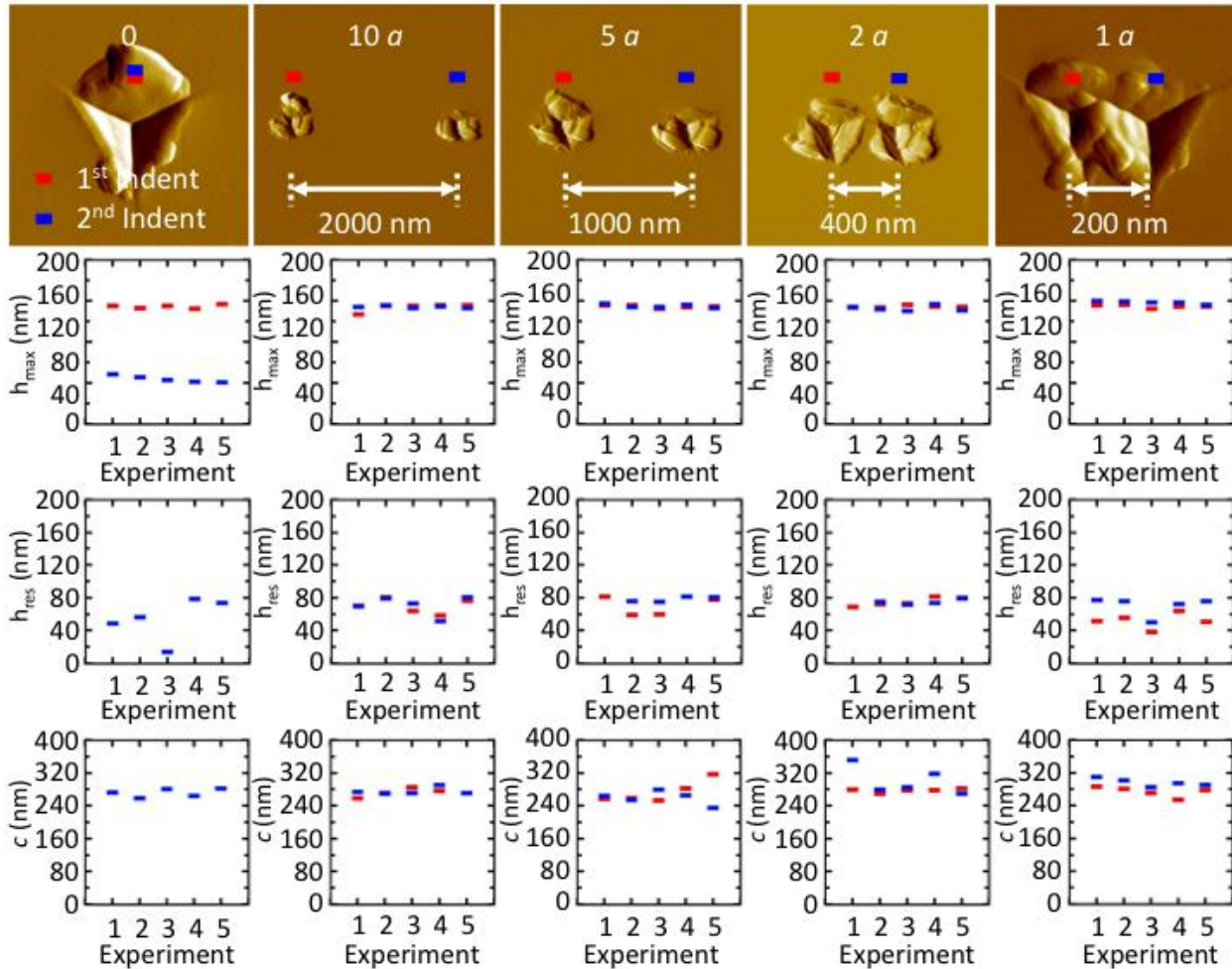


Figure 5-6. 800  $\mu\text{N}$  adjacent indent amplitude images with maximum depth, residual depth, and radial crack length measurements. Data from the five repeats (experiments) of each indentation condition are provided

## 5.5 Discussion

### 5.4.1 No Fracture Below the Threshold

Visual inspection of AFM amplitude images found no cracks below the single isolated indent fracture threshold reported in Chapter 4 (280  $\mu\text{N}$  – 290  $\mu\text{N}$ ). This indicated that stress field interactions from adjacent indents do not increase tensile stress to the threshold level necessary for fracture. Future studies could investigate a different range of separation distances, a larger number of interacting stress fields (from  $>2$  indents), and a maximum load that is closer to the single isolated fracture threshold.

#### **5.4.2 Elastic Relaxation of Indents**

The combination of elastic recovery and oxide growth significantly reduced the residual depth of each indent to ~ half the maximum depth as observed in the indent depth plots of (Figures 5-4, 5-5, and 5-6). Another potential factor contributing to the difference in depth measurements is the error associated with the radius of the cantilever tip, which limits its ability to reach the deepest point of the indent. Tip wear increases the radius of the tip and thus the error in indent depth measurements. This error would have led to reported residual indent depth that was shallower than the true indent depth.

#### **5.4.3 Adjacent Nanoindentations Separated by 0a**

At zero separation (0a), there are two indents in the same position. At this separation, at all loads (50  $\mu\text{N}$ , 200  $\mu\text{N}$ , 800  $\mu\text{N}$ ), second indents are less deep than first indents because the material has been plastically deformed by the first indent prior to the second indentation. The residual indentation consists of only one impression, so that only one set of residual measurements is recorded and plotted in Figures 5-4, 5-5, and 5-6.

#### **5.4.4 Adjacent Nanoindentations Separated by 10a**

At 10a separation, the maximum depth, residual depth, and radial crack length (for 800  $\mu\text{N}$  indents) of first indents are the same or within a close size range (10 nm) of second indents, which indicates that there is no interaction between indents separated by 10a. This result is supported by the work of Zhang, et al.<sup>40</sup> who performed adjacent Vickers indentations in glass and found that when the normalized separation was large, i.e. the separation was greater than 10 times the diameter of the indents, the interaction between adjacent indents was negligible.

#### **5.4.5 Adjacent Nanoindentations Separated by 5a**

At a separation of 5a, there does not appear to be a consistent difference between the maximum depth, residual depth, or radial crack length (for 800  $\mu\text{N}$  indents) of first and second indents at any load. If there is an interaction between indents at this separation, it does not result in consistently decreasing or increasing the depth of the second indent, or the length of the radial cracks. The reason for this could be associated with an attractive or repulsive interaction response described by Choi, et al.<sup>41</sup>, who reported that cracks due to adjacent indents in soda-lime glass may be “repulsive” or “attractive” depending on the induced stress field, with the crack size due to the second indent being greater in the “attractive” mode than in the “repulsive” mode. Though their study was concerned with crack interaction, it is possible that a similar system affects indent depth also. Further studies would be necessary to confirm this.

#### **5.4.6 Adjacent Nanoindentations Separated by 2a**

At a separation of 2a, there does not appear to be a consistent difference between the maximum depth, residual depth, or radial crack length (for 800  $\mu\text{N}$  indents) of first and second indents at any load. If there is an interaction between indents at this separation, it does not result in consistently decreasing or increasing the depth of the second indent, or the length of the radial cracks. This reason for this could be the same as that explained in section 5.4.5 for adjacent nanoindentations separated by 5a, in the presence of competing ‘attractive’ forces, which increase indent depth and crack length, and ‘repulsive’ forces, which decrease indent depth and crack length.

Visual inspection of indents separated by 2a led to the identification of cracks that extended between each indent. This was found only in indent pairs separated by 2a, and was found in each of the 5 experimental repeats of each pair at this separation. At

1a separation, adjacent indents overlapped each other so that pile-up would have obscured the presence of any cracks in that region. At separations of 5a and 10a, it is assumed that the stress field interactions are not sufficient to cause intermediate cracks. These results are supported by a study of Xu, et al.<sup>59</sup> who investigated interacting sequential scratches via experiments on alumina ceramics, and found that in scratch pairs, the second scratch significantly extended the median crack induced by the first scratch and made it propagate towards the second scratch.

Zhang, et al.<sup>40</sup> reported that the median damage due to the first indentation propagates towards the second causing a damaged region at the center of the two indentations. Experimental validation of the finite element analysis revealed that at small separations, additional damage continues to occur between adjacent indentations. From the current study, it appears that this effect extends to nanoscale contacts at indentation separations  $< 5a$ . An amplitude image of an 800  $\mu\text{N}$  indentation pair separated by 2a, showing the intermediate crack between them, is shown in Figure 5-7.

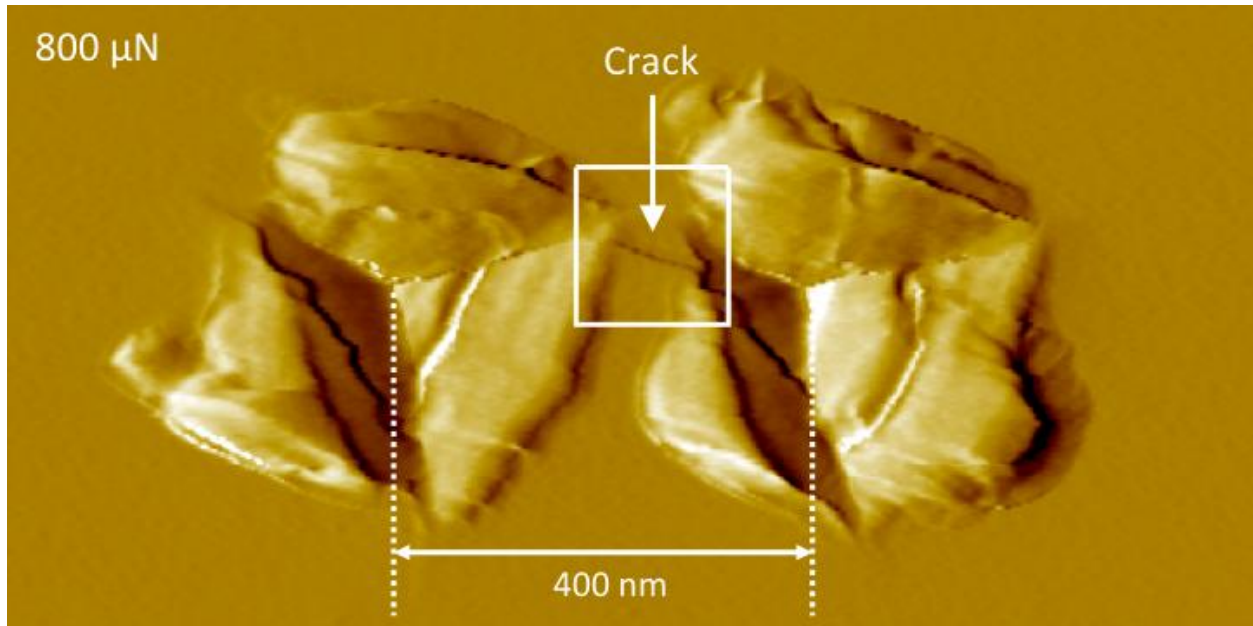


Figure 5-7. Amplitude image of 800  $\mu\text{N}$  adjacent indents separated by  $2a$  showing an intermediate crack between indents

#### 5.4.7 Adjacent Nanoindentations Separated by $1a$

At a separation of  $1a$ , second indents are consistently deeper at all loads (50  $\mu\text{N}$ , 200 $\mu\text{N}$ , 800 $\mu\text{N}$ ), and have a greater crack length (for 800  $\mu\text{N}$  indents), than first indents. This result indicates a stress field interaction, and is supported by the work of Zeng, et al.<sup>60</sup>, who reported that the residual stress field of a crack from a Vickers indentation strongly affects the crack length of a second indentation and that this effect increases as the second indent is closer to the first. The current study extends this result to nanoscale contacts.

#### 5.4.8 Stress Field Contours for Adjacent Indentations

Von Mises stress field contours provide a qualitative visualization of interacting elastic stress fields from adjacent indentations. Li, et al.<sup>61</sup> (1998) modeled the stresses of contacts in wire saw slicing. Those contours were developed from the solution to the problem of a rigid cone as solved by Sneddon<sup>62</sup> (1948) and incorporate stresses due to

tangential force. This study also uses the results of Sneddon<sup>62</sup>, however these contours are designed to aid in the visualization of nanoindentation contacts, not the lateral movements of abrasives in wiresaw slicing, and therefore do not incorporate stresses due to tangential forces.

#### **5.4.8.1 Equations of stress for a rigid cone contact**

The indentation process is modeled as a rigid circular cone indenting on a semi-infinite surface with normal force  $N$ . Indenters of various geometries are modeled as a cone by assigning them an effective cone angle,  $\alpha$ , which corresponds to the geometry of the indenter. For a cube corner indenter,  $\alpha = 42.280$ .<sup>63</sup>

The horizontal plane at  $z = 0$  represents the substrate surface with which the indenter makes contact. The point of contact is the origin of the coordinate system,  $O$ . The  $z$  axis is positive pointing downwards into the substrate. The cone is assumed to penetrate a distance of  $(b + \epsilon)$  into the substrate with a contact radius of  $a$ . The position at any point in the medium for which stresses are calculated is defined by the polar coordinates  $(r, \theta, z)$ .

The original surface at  $z = 0$  is pushed down due to loading of the indenter. On the surface, the normal component of the displacement vector is given by the shape of the cone in the  $r \leq a$  region, from the vertex,  $V$ , to the uppermost contact circle of radius  $a$ . Outside this region, i.e. at  $0 \leq z \leq b$  and  $r > a$ , the normal component of the stress vanishes across the boundary of the medium because no contact is made, and the deformed surface is a free surface. Shear stress is assumed to be zero across the entire surface  $z = 0$ . An indentation model for a conical contact is shown in Figure 5-8.

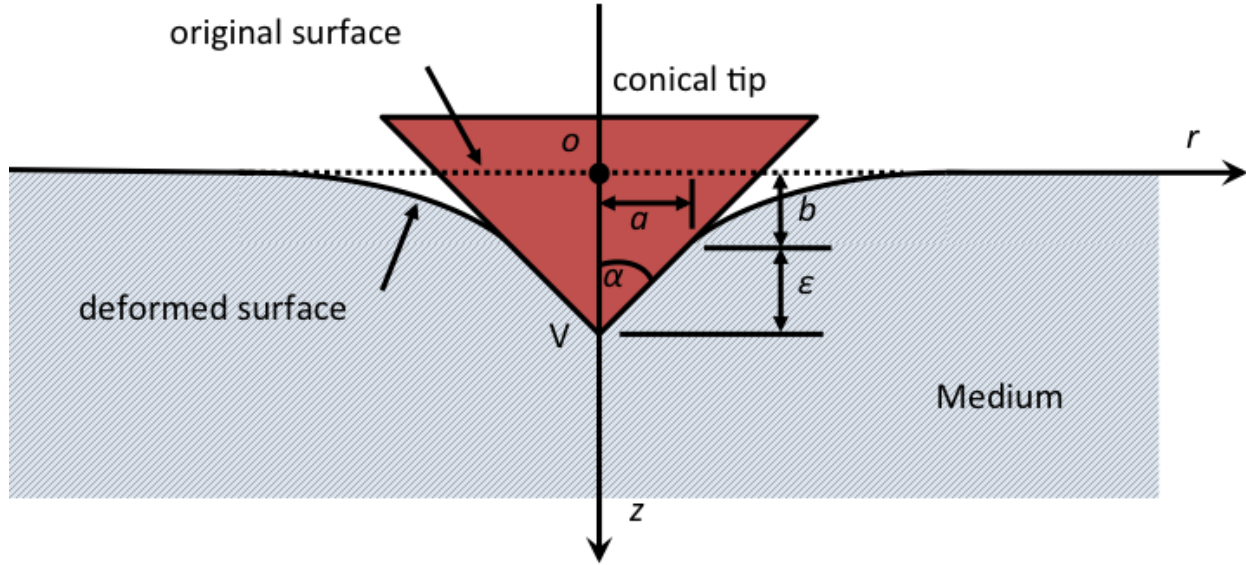


Figure 5-8. Indentation model for a conical contact penetrating a medium a depth of  $b + \epsilon$ , where  $b$  is the distance from the vertical point of contact to the original surface of the medium, and  $\epsilon$  is the depth of the contact area from the vertex to the level of the circle with radius  $a$ .  $O$  is the origin of the coordinate system and  $V$  is the vertex of the conical tip

The equilibrium equations for infinitesimal motions along the  $r$  and  $z$ -directions

(Sneddon, 1947)<sup>62</sup> are:

$$\frac{\partial \sigma_r}{\partial r} + \frac{\partial \tau_{rz}}{\partial z} + \frac{1}{r}(\sigma_r - \sigma_\theta) = 0 \quad (5-1)$$

$$\frac{\partial \tau_{rz}}{\partial r} + \frac{\partial \sigma_z}{\partial z} + \frac{\tau_{rz}}{r} = 0 \quad (5-2)$$

With boundary conditions

$$u_z = [u_z(r)]_{z=0} \text{ at } z = 0, 0 \leq r \leq a \quad (5-3)$$

$$\sigma_z = 0 \text{ at } z = 0, r > a \quad (5-4)$$

$$\tau_{rz} = 0 \text{ at } z = 0, r \geq a \quad (5-5)$$

#### 5.4.8.2 Polar stress coordinates

The theory of Henkel transforms<sup>62</sup> can be used to solve Equations 5-1 through 5-5 to obtain the polar coordinate stresses Equations 5-6 through 5-9. Two normalized

parameters are defined with respect to the geometric parameter of indentation:  $\zeta = z/a$  and  $\rho = r/a$ . The stresses are written with a scaling factor,  $a/\varepsilon E$ , to obtain dimensionless measures of stress, as follows;

$$\frac{a\sigma_z}{\varepsilon E} = -\frac{1}{2(1-\nu^2)} [J_1^0(\rho, \zeta) + \zeta J_2^0(\rho, \zeta)] \quad (5-6)$$

$$\frac{a\sigma_\theta}{\varepsilon E} = -\frac{1}{2(1-\nu^2)} \left[ 2\nu J_1^0(\rho, \zeta) + \frac{1}{\rho} (1 - 2\nu) J_1^1(\rho, \zeta) \right] \quad (5-7)$$

$$\frac{a(\sigma_r + \sigma_\theta + \sigma_z)}{\varepsilon E} = -\frac{1}{(1-\nu)} J_1^0(\rho, \zeta) \quad (5-8)$$

$$\frac{a\tau_{rz}}{\varepsilon E} = -\frac{1}{2(1-\nu^2)} \zeta J_2^1(\rho, \zeta) \quad (5-9)$$

where  $E$  is Young's modulus,  $\nu$  is Poisson ratio, and  $J_m(\rho p)$  is the Bessel function of  $m^{\text{th}}$  order. The integrals  $J_n^m$  can be written as

$$J_n^m(\rho, \zeta) = \int_0^\infty [1 - \cos(p)\rho^{n-2} J_m(\rho p) e^{-p\zeta}] dp \quad (5-10)$$

In Equations 5-16 through 5-19 five  $J_n^m$  integrals are needed

$$J_1^0(\rho, \zeta) = \frac{1}{2} \ln \frac{\xi^2 + 2\xi\sqrt{1+\zeta^2}\cos(\theta-\phi) + 1 + \zeta^2}{(\zeta + \sqrt{\rho^2 + \zeta^2})^2} \quad (5-11)$$

$$J_2^0(\rho, \zeta) = \frac{1}{\sqrt{\rho^2 + \zeta^2}} - \frac{\cos(\phi)}{\xi} \quad (5-12)$$

$$J_1^1(\rho, \zeta) = \frac{1}{\rho} [\sqrt{\rho^2 + \zeta^2} - \xi \cos(\phi)] \quad (5-13)$$

$$J_0^1(\rho, \zeta) = \frac{1}{2} \left[ \rho J_1^0(\rho, \zeta) + \frac{1}{\rho} (1 - \xi \sin\phi) - \zeta J_1^1(\rho, \zeta) \right] \quad (5-14)$$

$$J_2^1(\rho, \zeta) = \frac{1}{\rho} \left[ \frac{\sqrt{\rho^2 + \zeta^2}}{\xi} \cos(\theta - \phi) - \frac{\zeta}{\sqrt{\rho^2 + \zeta^2}} \right] \quad (5-15)$$

where;

$$\phi = \frac{1}{2} \tan^{-1} \left( \frac{2\zeta}{\rho^2 + \zeta^2 - 1} \right) \quad (5-16)$$

$$\xi^4 = (\rho^2 + \zeta^2 - 1)^2 + 4 \quad (5-17)$$

$$\cot\theta = \zeta \quad (5-18)$$

The geometric parameters and components of stress elements due to indenting forces are displayed in Figure 5-9.

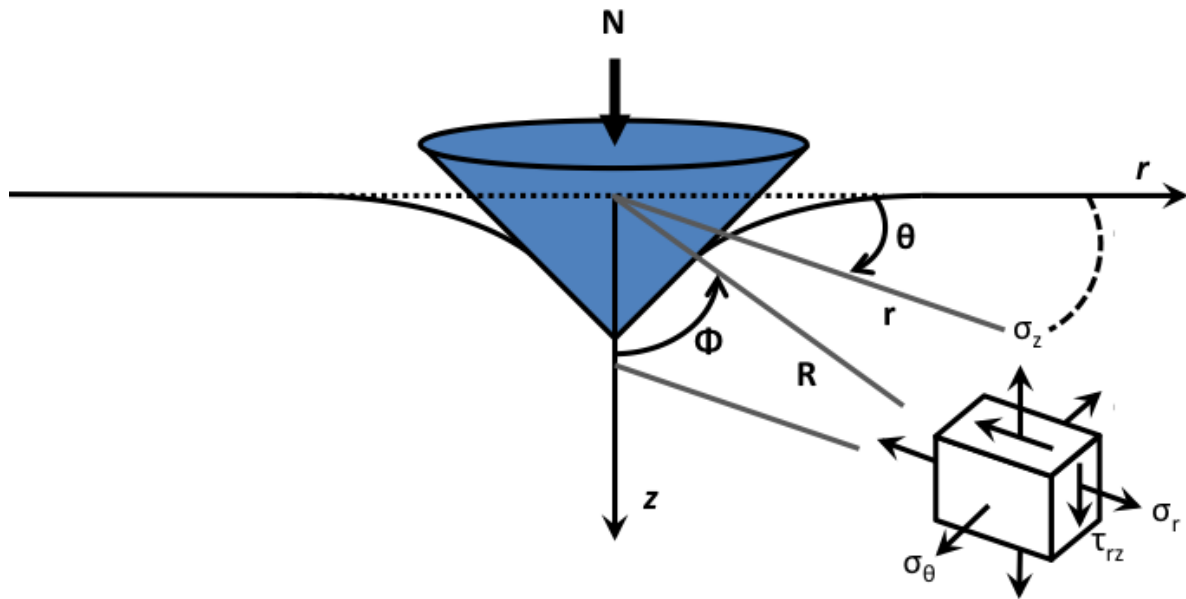


Figure 5-9. Illustration of the polar stress components of an infinitesimal element in response to an indenting cone with normal force (N) applied vertically downwards. The distance of the stress element from the origin is R, with a projection onto the xy-plane and z onto the z-axis. The polar stresses,  $\sigma_r$ ,  $\sigma_\theta$ , and  $\sigma_z$  as well as the shear stress  $\tau_{rz}$  are shown

To create a single indentation stress field plot, the equations of stress (Equations 5-6 through 5-9) are plotted as a function of Equations 5-11 through 5-15 and the dimensionless factors (Equations 5-16 through 5-18) and the following inputs;

$\epsilon$  (contact depth of medium) = max indent depth (use experimental results)

$\alpha$  (effective cone angle) =  $42.28^\circ$  (Fischer-Cripps, 2002)<sup>64</sup>

a (contact circle radius) =  $h_p \tan(\alpha)$

E (elastic modulus of Si(100)) = 185.6 GPa (Pharr, 1998)<sup>27</sup>

v (Poisson's ratio) = 0.25 (Li, et al., 1998)<sup>61</sup>

#### 5.4.8.3 Principal stresses

Principal stresses are calculated from polar coordinate stresses:

$$\sigma_1 = \frac{\sigma_r + \sigma_z}{2} + \sqrt{\left(\frac{\sigma_r - \sigma_z}{2}\right)^2 + \tau_{rz}^2} \quad (5-19)$$

$$\sigma_2 = \sigma_\theta \quad (5-20)$$

$$\sigma_3 = \frac{\sigma_r + \sigma_z}{2} - \sqrt{\left(\frac{\sigma_r - \sigma_z}{2}\right)^2 + \tau_{rz}^2} \quad (5-21)$$

Maximum shear stress is calculated from the principal stresses:

$$\tau_{max} = \frac{1}{2} (\sigma_1 - \sigma_3) \quad (5-22)$$

#### 5.4.8.4 Von Mises stress criterion

Octahedral shear stress theory, also known as the maximum distortion energy criterion, the Maxwell-Huber-Hencky-von Mises theory, or the von Mises stress criterion is used to estimate the yield stress of ductile materials. It is used to model stress field interactions for nanoscale contacts (<100 nm) because there is a considerable plastic material response before fracture at this scale. This is in contrast to the brittle material response of Si as observed at the macroscale.

The von Mises criterion states that failure occurs when the energy of distortion reaches the same energy for yield/failure in uniaxial tension. Mathematically, this is expressed as:

$$\sigma_v = \sqrt{\frac{1}{2} (\sigma_1 - \sigma_2)^2 + (\sigma_1 - \sigma_3)^2 + (\sigma_2 - \sigma_3)^2} \quad (5-23)$$

Where  $\sigma_v$  is the von Mises stress.

The von Mises yield surface is plotted against principal stress axes and represented in three dimensions in Figure 5-10 where it is shown in relation to the Tresca yield surface

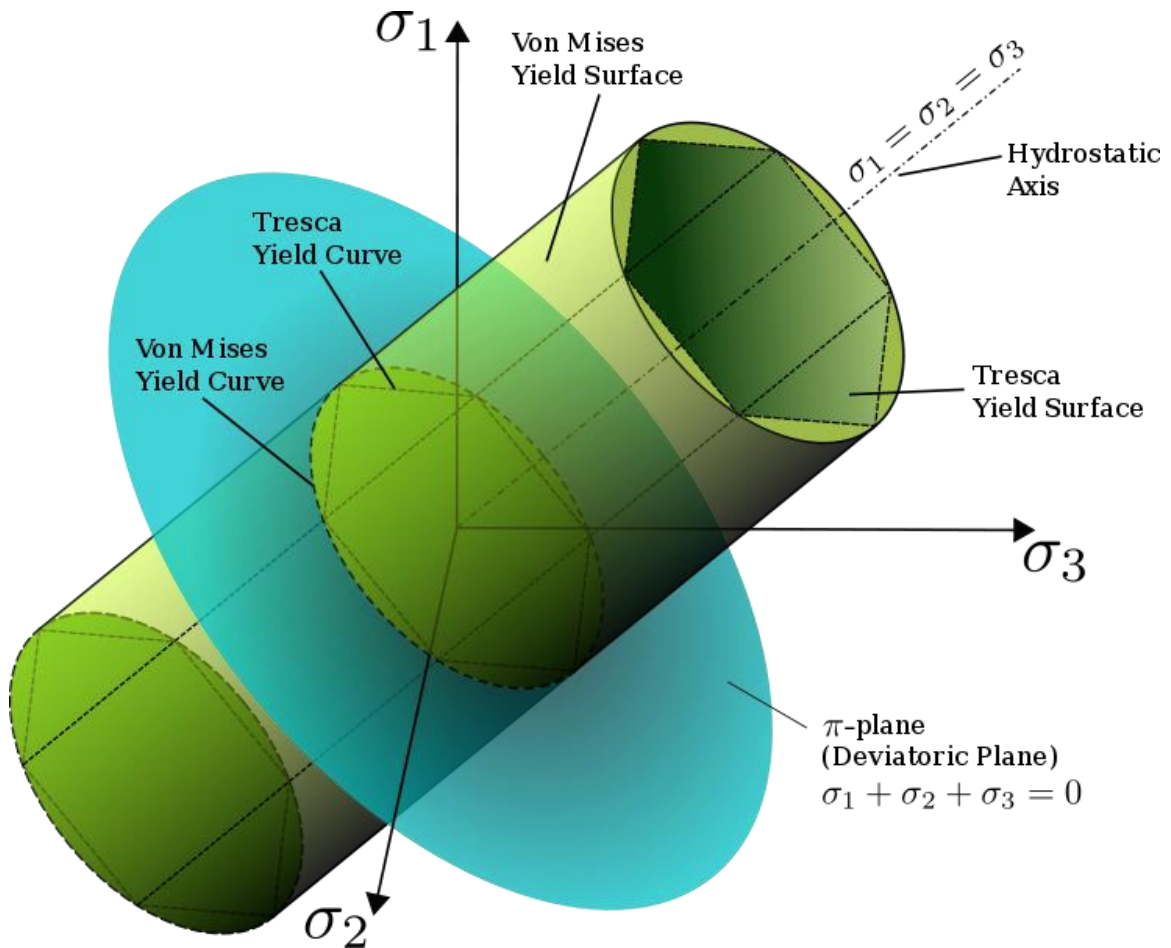


Figure 5-10. Illustration of von Mises and Tresca yield surfaces in the principal stress coordinates, including the deviatoric plane and hydrostatic axis. [Adapted from Rswarbrick, Von Mises yield criterion, Available at [HYPERLINK "http://en.wikipedia.org/wiki/Von\\_Mises\\_yield\\_criterion"](http://en.wikipedia.org/wiki/Von_Mises_yield_criterion) [http://en.wikipedia.org/wiki/Von\\_Mises\\_yield\\_criterion](http://en.wikipedia.org/wiki/Von_Mises_yield_criterion) (2009)]

#### 5.4.8.5 Modeling the stress field contours in Matlab

Stress field contours were developed from Equations 5-1 through 5-23 using Matlab (MathWorks®, Natick, MA, USA) software. The coordinate positions on each plot

were normalized to the radius of the circle of contact,  $a$ , in the form  $(\zeta, \rho)$ , where  $\zeta = z/a$  and  $\rho = r/a$ . In the contour plots, the indenter load,  $P$ , for the initial (first) indent is applied vertically downwards at coordinate position  $(0,0)$ . The second indenter load, equivalent to  $P$  also, is applied at a distance  $\rho = r/a$ , from the initial indent. The value of each stress contour ( $\sigma_v$ ) was normalized with the scaling factor  $a/(\epsilon E)$ . The m-file code used to create the adjacent indentation stress field contours is reproduced in Appendix A. The m-file code used to create the single indentation stress field contour is reproduced in Appendix B.

#### **5.4.8.6 Von Mises stress field contours for adjacent indentations**

The Von Mises stress field contours for a single indentation and adjacent indentations separated by  $1a$ ,  $2a$ ,  $5a$ , and  $10a$ , are shown in Figure 5-11. The magnitude of the stress contours is normalized by the factor  $a/(\epsilon E)$ .

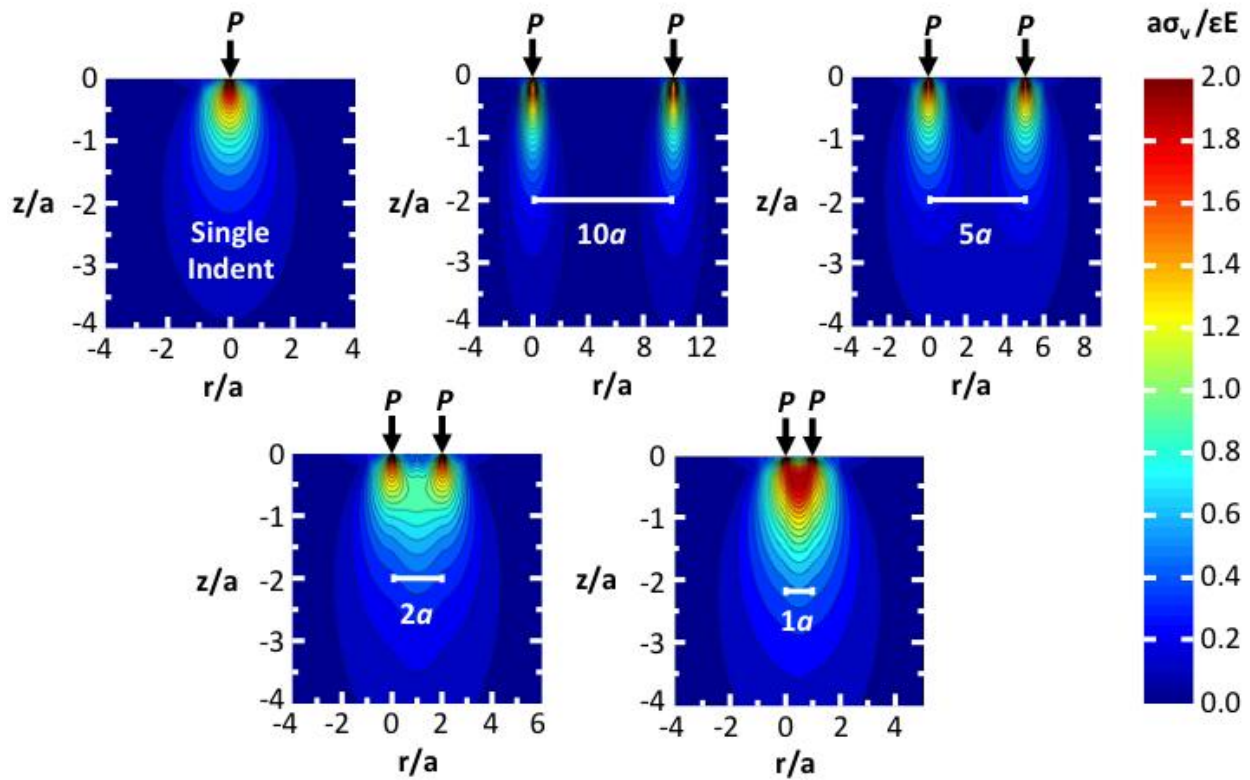


Figure 5-11. Von Mises stress field contours for adjacent indentations

It is important to note that these contours were developed for a purely qualitative understanding of interacting stress fields. For simplicity, these contours assume simultaneous contact and zero plastic deformation. In practice, the contacts are sequential and the first indentation creates plastic deformation that affects the second indentation, particularly at small separations. This would result in asymmetrical contours. A more quantitative contour model of interacting stress fields would account for plastic deformation, residual stress effects on the second indent, and the effects of the interaction on the development of the stress field. Such complexity is beyond the scope or requirements of this thesis. For a qualitative visualization of the interaction of

stress fields from adjacent indentations, the current elastic stress field superposition contour model is sufficient.

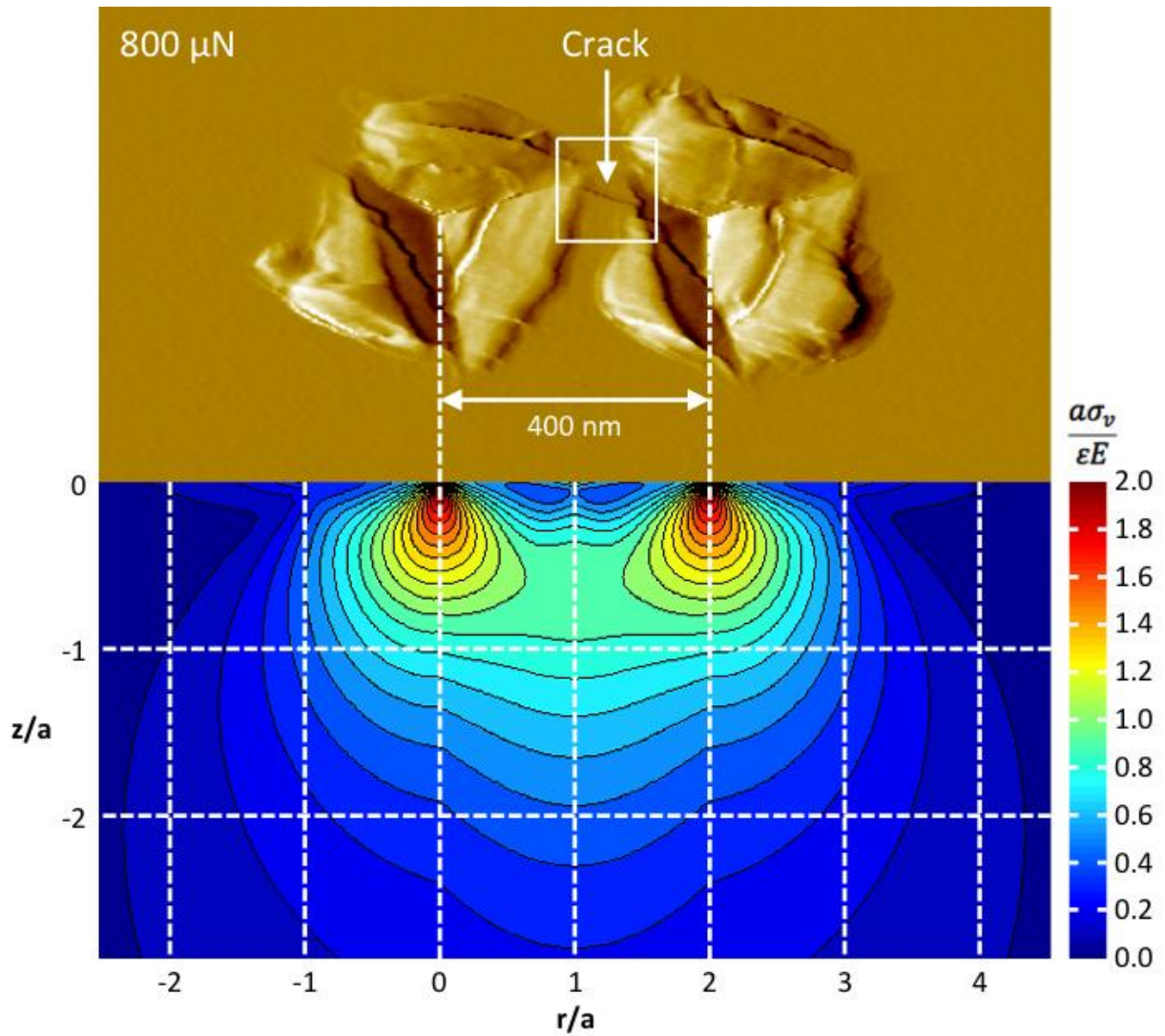


Figure 5-12. Amplitude image of a 800  $\mu\text{N}$  adjacent indents separated by  $2a$  with matching Von Mises stress field contours

From Figure 5-11 it is evident that no stress field interaction exists at a separation of  $10a$ . At a separation of  $5a$  there also appears to be no interaction. At a separation of  $2a$  there is a superposition of stress fields that creates a region of increased stress between the two indents. It is expected that this region of increased tensile stress is responsible for the intermediate crack between 800  $\mu\text{N}$  adjacent indents separated by

2a as shown in figure 5-12. At 1a separation, the Von Mises contours (Figure 5-11) reveal a very intense region of increased stress between and surrounding the two contacts, below the surface. This is thought to be the cause of the consistent increase in indent depth and radial crack length between first and second indents in the adjacent indentation experiment.

#### **5.4.9 Secondary Radial Cracks Release Residual Stress**

Secondary crack systems further complicate the measurement of cracks and their associated stress field interactions. Secondary cracks are cracks that are observed to extend from the indent impression, but not parallel to one of the vertices. Secondary radial cracks (Figure 5-13) release some of the residual stress in the material, thus affecting the crack-opening displacement (COD) of the main radial cracks.<sup>29</sup> At low loads such as in these experiments (< 1 mN), the COD is in the order of nanometers, making it difficult to draw conclusions from trends in the data. Considering the presence of multiple crack systems and interaction effects, the stress-analysis based approach becomes very complicated. Energy-based models have been developed to deal with such complications. A review of the use of energy-based models in brittle fracture can be found in the review by Chen, et al.<sup>29</sup>

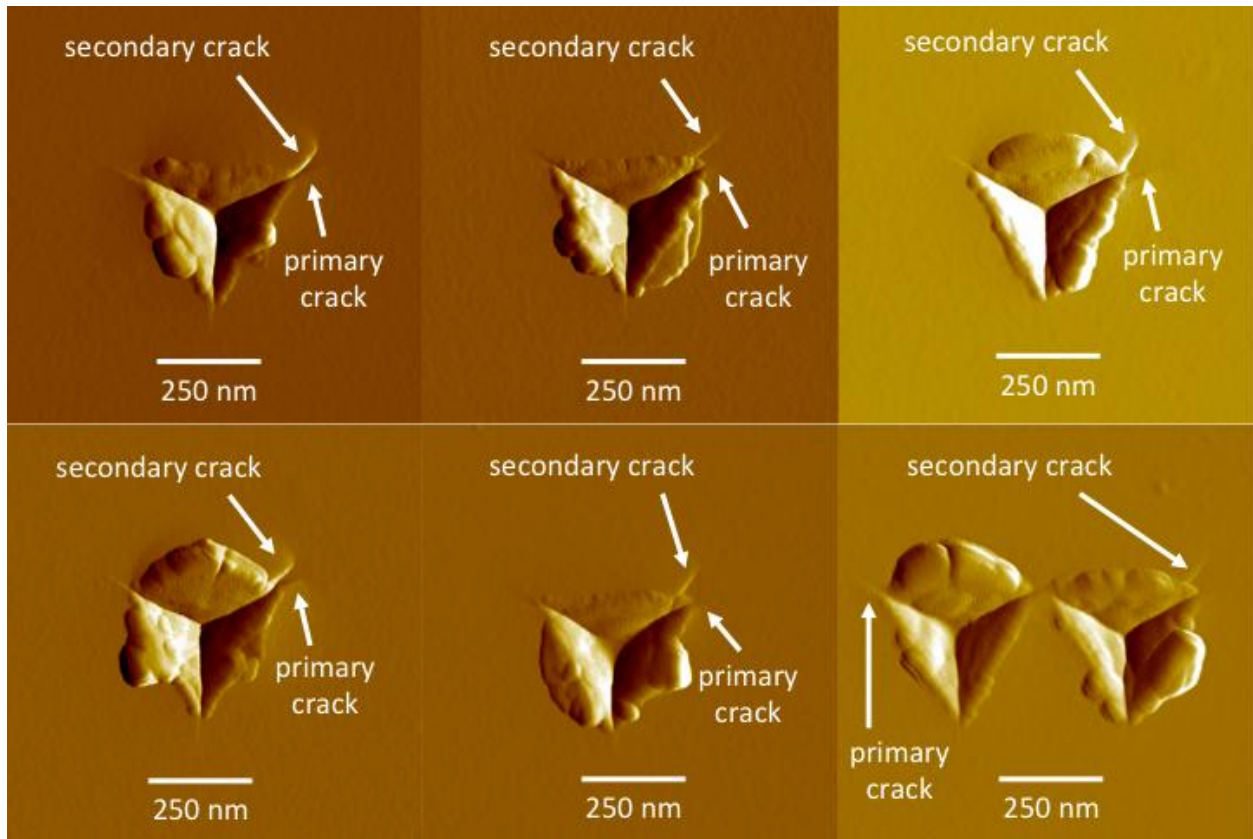


Figure 5-13. Selected amplitude images of 800  $\mu\text{N}$  indents showing the presence of both primary and secondary cracks. Secondary cracks release some of the residual stress in the material, this affecting the extension of primary cracks

## CHAPTER 6 CYCLIC LOADED INDENTATION EXPERIMENT

### 6.1 Overview

In this chapter, cyclic loaded indentation is performed as a function of maximum load and load cycle. AFM metrology is conducted by inspecting indent images for evidence of fracture below the threshold. Indents are characterized via depth and crack length measurements, which are plotted against load cycle for the observation of correlations between these parameters.

### 6.2 Calibration and Preparation

The nanoindenter was calibrated with a virtual deflection calibration as outlined in section 3.5, then an InvOLS calibration using the procedure in section 3.6. After nanoindentation calibrations were completed, the 10 x 10 mm<sup>2</sup> Si(100) substrate was cut, cleaned and checked for particulates as described in section 3.2. A 0.5 mm line was scribed at a 5 mN load using a Berkovich indenter as described in section 3.8. After these preparatory steps, the nanoindentation arrays were performed with a cube corner indenter tip.

### 6.3 Cyclic Load Nanoindentation Array

The cube corner indenter was inserted into the nanoindenter module, which was still affixed to the AFM head. The AFM head was then lowered onto the Si sample which remained unmoved since the Berkovich scribing to ensure a contact with close proximity (< 90  $\mu\text{m}$ ) to the previous final Berkovich tip withdrawal. Indentations were performed under load control at maximum loads of 50  $\mu\text{N}$ , 200  $\mu\text{N}$ , 400  $\mu\text{N}$ , and 800  $\mu\text{N}$ .

50  $\mu\text{N}$  adjacent indents represented adjacent abrasive contacts in the magnetic assisted finishing (MAF) process, which contact the surface with ultra-low loads

imparted by the magnetic field. Fracture at this load would indicate that adjacent diamond abrasive contacts in MAF were also capable of causing fracture. This would indicate that fracture would be a possible material removal mechanism in MAF. It would also prove a significant limitation to the indentation fracture model in not addressing adjacent contacts. If fracture were observed at this load, it would be evidence of a stress field interaction between adjacent indentations.

200  $\mu\text{N}$  indents represented contacting close to, but below the fracture threshold. Fracture at this load would indicate a stress field interaction between adjacent indentations.

400  $\mu\text{N}$  indents were present in the cyclic loading experiment but did not feature in the adjacent indentation tests of Chapter 5. The addition was due to the fact that when adjacent indentations were conducted, the final fracture threshold experiments were not complete, and the fracture threshold was known only to occur below 800  $\mu\text{N}$  (see Figure 4 – 6). After the adjacent indentation experiment was complete, further experiments (section 4.2.8) discovered the more precise value for the fracture threshold of 280  $\mu\text{N}$  – 290  $\mu\text{N}$ . With this information, cyclic indentation was performed at 400  $\mu\text{N}$  to represent a force close to, but just above, the fracture threshold. Fracture at this load, which is above the fracture threshold, was expected. This would allow for the measurement of indent cracks as a function of load cycle.

800  $\mu\text{N}$  represented a load relatively high above the fracture threshold of 280  $\mu\text{N}$  – 290  $\mu\text{N}$ . Fracture was expected at this load. This would allow for the measurement of indent cracks as a function of load cycle.

Indents were conducted in 3 different load cycle functions: Single loading, 10 load cycles, and 100 load cycles. Deformation and indent crack length was measured as a function of load cycle. Each maximum indentation load, and load cycle, were performed 5 times for added statistical significance to the data. 5 copies of 50  $\mu\text{N}$  single loaded indents were separated by 1  $\mu\text{m}$  in the x direction. 5 copies of 50  $\mu\text{N}$  indents loaded 10 times were performed 1  $\mu\text{m}$  below the single loaded indents and were also separated by 1  $\mu\text{m}$  in the x direction. 5 copies of 50  $\mu\text{N}$  single loaded indents were separated by 1  $\mu\text{m}$  in the x direction. 5 copies of 50  $\mu\text{N}$  indents loaded 100 times were performed 1  $\mu\text{m}$  below the indents loaded 10 times and were also separated by 1  $\mu\text{m}$  in the x direction. This resulted in a 5 x 3 grid of 50  $\mu\text{N}$  indents where the x axis position indicated the experimental repeat number of the indent and the y axis position indicated the load cycle. The 200  $\mu\text{N}$  indents were conducted in the same fashion as the 50  $\mu\text{N}$  indents with the exception that the separation between indents was 2  $\mu\text{m}$  and the grid of indents was performed 2  $\mu\text{m}$  below the 50  $\mu\text{N}$  indents. 400  $\mu\text{N}$  indents were performed in the same manner but with 3  $\mu\text{m}$  spacing, and 800  $\mu\text{N}$  indents were separated by 4  $\mu\text{m}$ . The nanoindentation array is illustrated in Figure 6-1.

The loading function for each indent consisted of a 5 sec load, 2 sec hold, and 5 sec unload. Indentation was performed with a start distance of 5.26  $\mu\text{m}$ , force distance of 500 nm, and velocity of 100 nm/s. The trigger was set to 5  $\mu\text{N}$ .

AFM was performed using the procedure outlined in 3.7. Indents were scanned using an SSS-NCH SuperSharpSilicon<sup>TM</sup> (Nanosensors<sup>TM</sup>, Neuchatel, Switzerland) non-contact mode AFM probe with ~2 nm tip radius. Post image processing was conducted on the indents using the methodology described in 3.8. Indent radial crack length was

measured from AFM amplitude images using the methodology described in section 3.9. Processed AFM height images of each indent were measured to record residual indent depth using the methodology detailed in section 3.10.

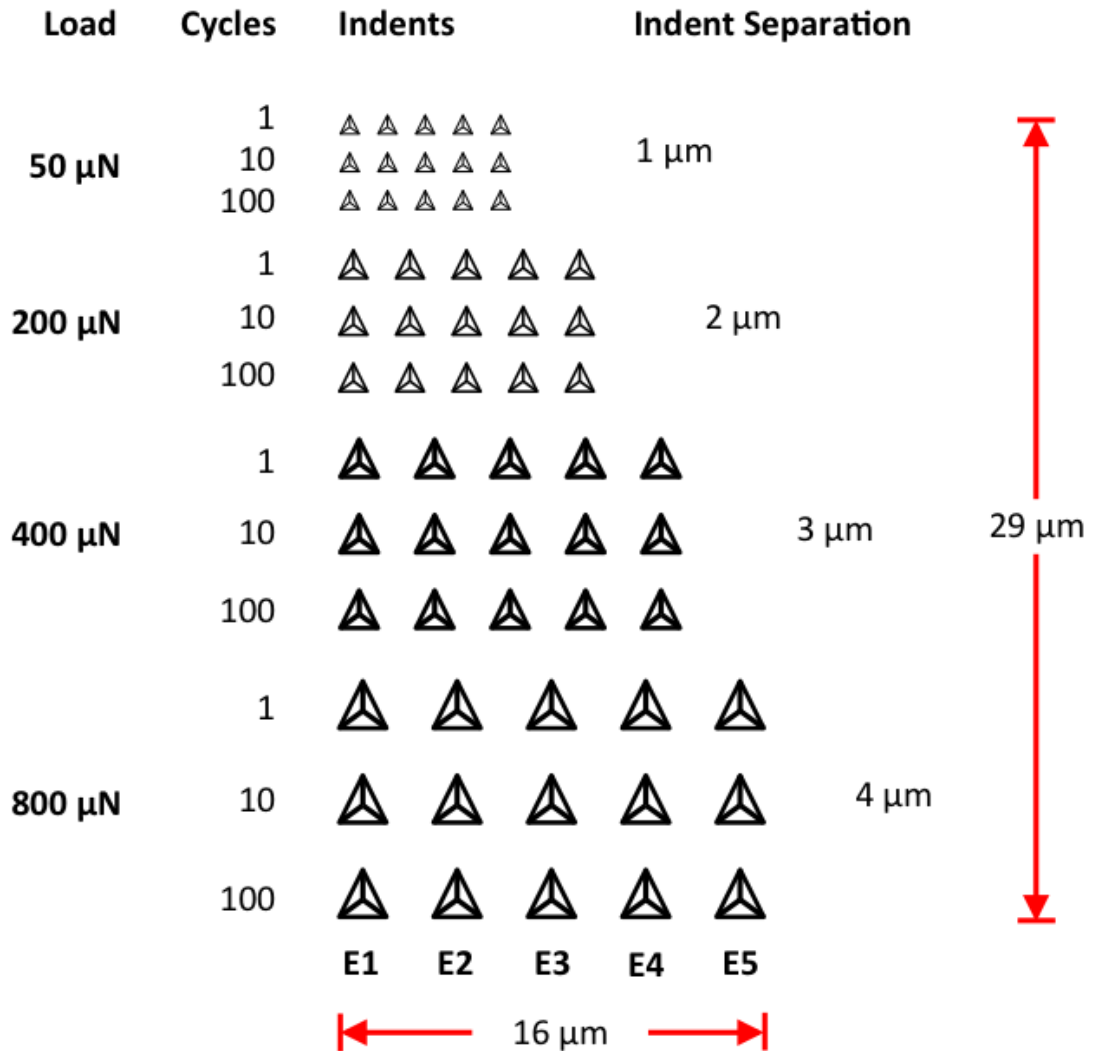


Figure 6-1. Illustration of the cyclic load indentation array. E1, E2, etc. refers to the experimental repeat number

### 6.3 Results

Visual inspection of the AFM scans of the cyclic load indentations (Figure 6-1) revealed an increase in plastic deformation, surface pile-up, and indent size associated

with increased load cycle. No cracks appeared below the fracture threshold for single, isolated indentations (280  $\mu\text{N}$  – 290  $\mu\text{N}$ ).

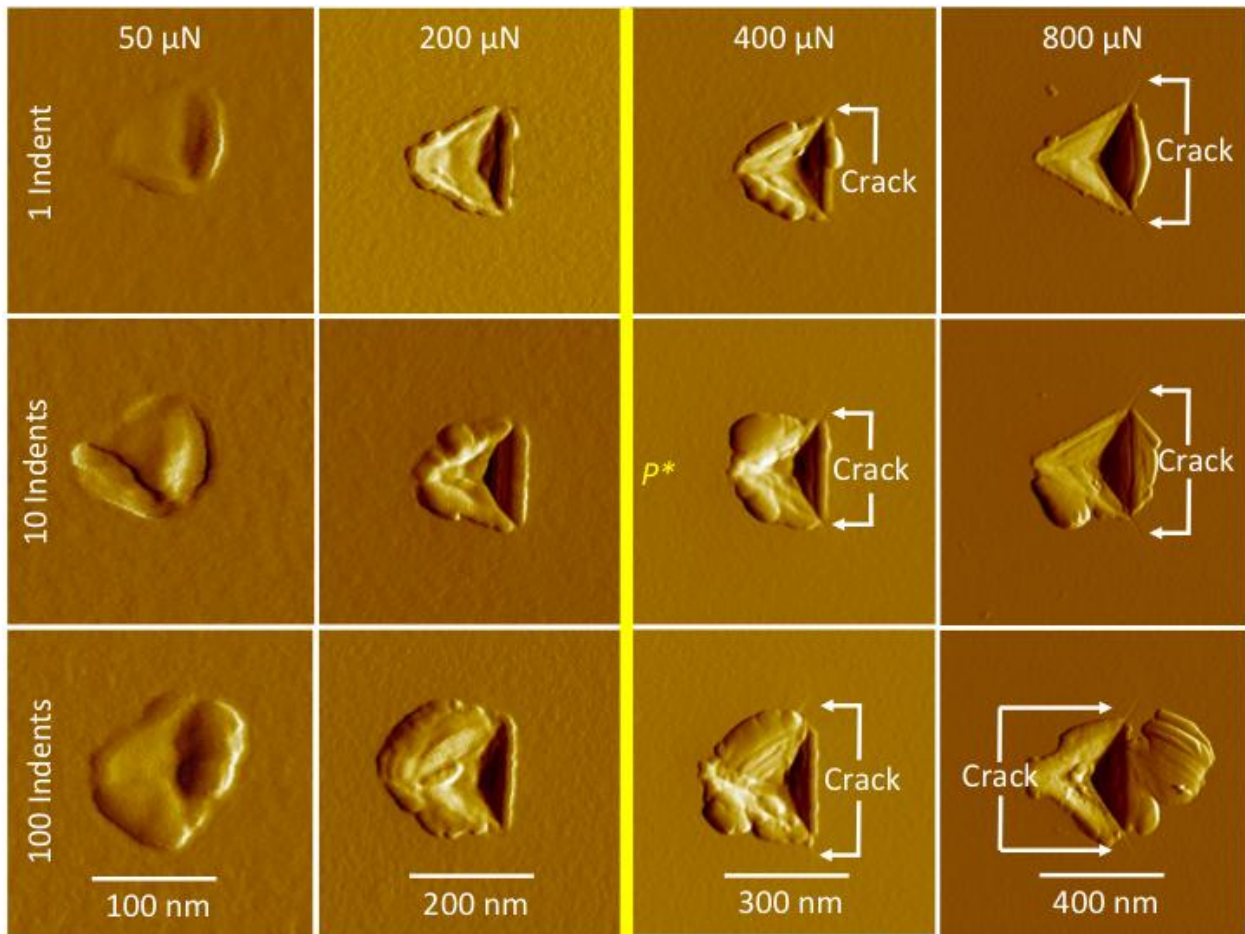


Figure 6-2. Selection of AFM amplitude images of cyclic load indents, showing no fracture below the fracture threshold,  $P^*$

Residual indent depth was plotted as a function of load cycle on a log plot in Figure 6.3. This plot shows an increase in residual indent depth associated with an increase in load cycle from 1 to 10 to 100 cycles. This increased residual depth occurs at each indentation load, both above and below the fracture threshold, however the effect is more pronounced above the fracture threshold.

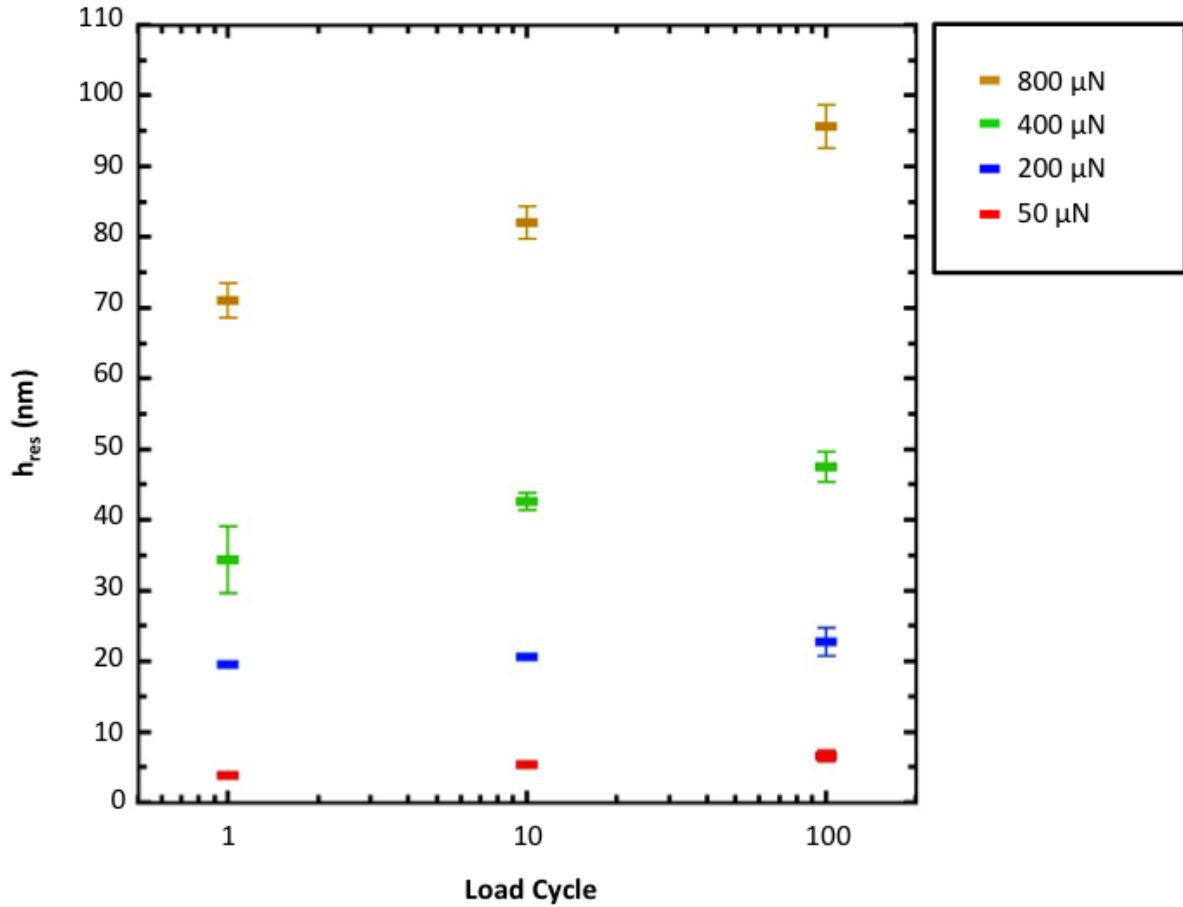


Figure 6-3. Load cycle vs. residual indent depth ( $h_{\text{res}}$ ) plot. Error bars represent 1 standard deviation from the mean

Radial crack length ( $c$ ) was plotted as a function of load cycle on a log plot in Figure 6-4 for 400  $\mu\text{N}$  and 800  $\mu\text{N}$  indents. Only data from indents loaded above the fracture threshold are plotted, because there are no cracks below the threshold load. This plot reveals that load cycles increase the radial crack length at both 400  $\mu\text{N}$  and 800  $\mu\text{N}$  indents. The increase in radial crack length between 10 and 100 load cycles for a 400  $\mu\text{N}$  indentation appears to be less pronounced than between 1 and 10 load cycles of the same load.

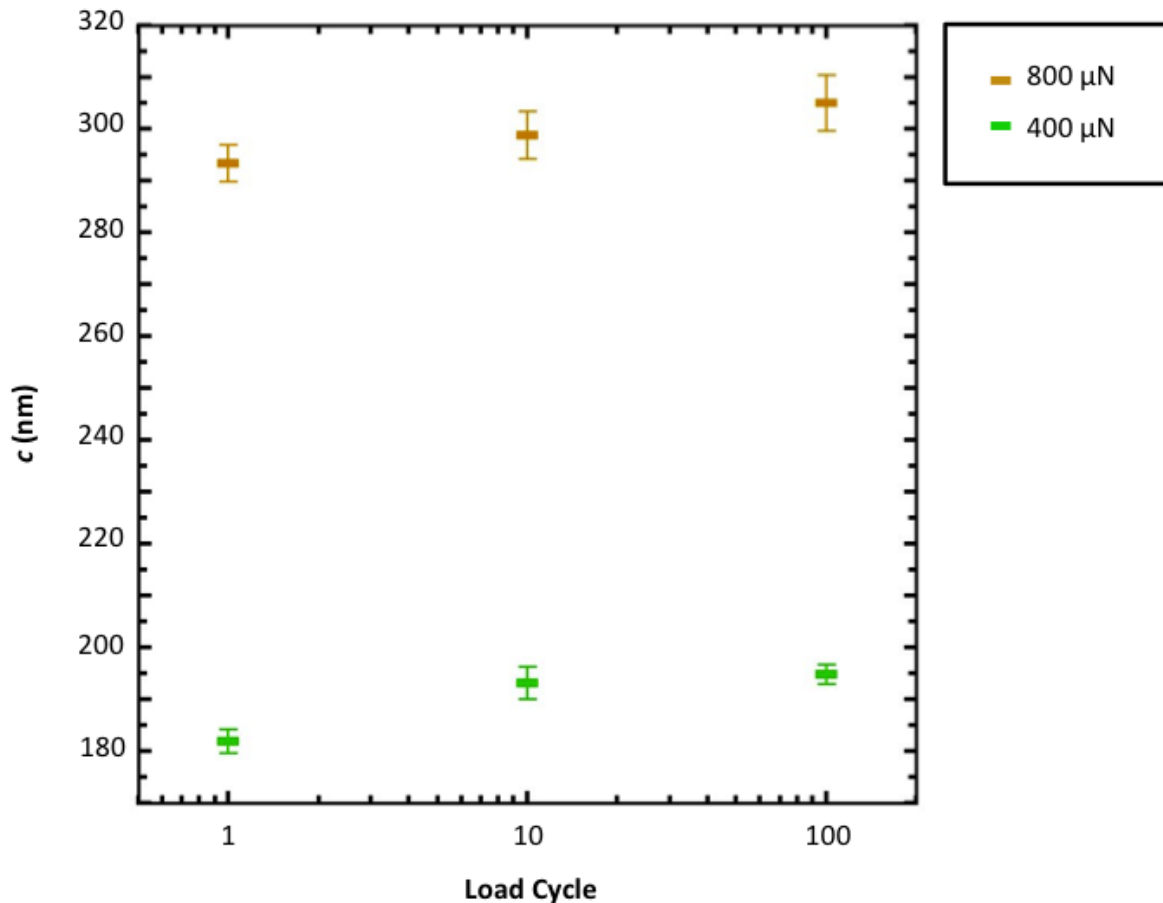


Figure 6-4. Load cycle vs. radial crack length ( $c$ ) plot. Error bars represent 1 standard deviation from the mean

#### 6.4 Discussion

No fracture was observed below the threshold, despite cyclic loading. However, cyclic loading increases plastic deformation, surface pile-up, and indent size in nanoindentations performed by a cube corner indenter in Si(100). This experiment also found that above the fracture threshold, cyclic loading leads to an increase in radial crack length.

Based on previous studies<sup>43, 45, 26, 50, 51</sup> that investigated the effects of cyclic loading at larger scales ( $>>1$  mN), it is thought that the cause of the increased deformation, pile-up, indent depth, and crack length from cyclic loading is caused by

stress concentration. Slip steps lead to immediate plastic deformation and emit dislocations into the crystal upon subsequent reloading of the surface. In contrast, defects that move to the surface in single loaded indentations did not act as dislocation sources. The contact fatigue response of cyclic indentation suppresses homogenous defect nucleation within the crystal, causing the crystal to yield at lower loads. Furthermore, cyclic contacts lead to increased dislocation interactions near the indented surface, resulting in an effective cyclic strain hardening of the crystal.

## CHAPTER 7 CONCLUSION

Mechanical nanofabrication technologies will be indispensable in the production of emerging micro- and nano-technologies. Methods such as nanoimprint embossing, massively parallel tip-based nanofabrication, continuous roll-to-roll processing, free abrasive machining, etc., provide a viable means of scalable nanostructuring of surfaces. This enables production of nanotechnologies with unmatched resolution and is compatible with almost any material. Mechanical nanofabrication involves moving parts and mating of surfaces that contact at dimensions less than 100 nm. Such small contacts concentrate the applied stresses, and can create irreversible damage and fracture, which limits resolution, accuracy, and reproducibility of the fabrication process. Therefore, it is critical to understand the fundamental deformation and fracture mechanisms that occur at nanoscale contacts.

This work investigated the extension of the Lawn and Evans indentation fracture model (developed primarily for microscale contacts) to nanoscale contacts. Systematic nanoindentation fracture experiments were performed on Si(100) using a sharp diamond cube corner (radius = 32 nm) indenter as a function of maximum load, cyclic loading, and contact separation. Atomic force microscopy (AFM) was used to image and measure contact deformation and fracture. Fracture appeared in AFM images of indents loaded to 290  $\mu\text{N}$ , which is lower than the previously reported fracture threshold for a cube corner indenter.

Sequential adjacent indentation experiments resulted in deeper second indents than first indents and longer radial cracks in second indents than first indents at a separation of twice the indent radius. At separations greater than 2 indent radii, this did

not occur. This indicates that the stress/strain fields between indents at this separation interact with each other to promote deformation and radial crack growth.

Cyclic loaded Indents that were repeated in the same position 100 times were found to be deeper, wider, and have longer radial cracks than single loaded indents. No cracks were observed below the single indentation fracture threshold.

Thus, the indentation fracture model extends to nanoscale contacts in the presence of single, adjacent, and cyclic loaded indentations. These results have clear implications for nanofabrication where stress field interactions impose limits on the closeness (resolution) to which features can be generated and to free abrasive machining where stress field interactions enhance the ability to machine below the threshold load.

The results have particular application to magnetic assisted nanomachining (MAF), where it is estimated that abrasives with nanoscale facets (<50 nm) strike the surface with loads of < 50  $\mu\text{N}$ , resulting in surface polishing that creates a <1 nm rms (root mean squared) surface. Although the indentation fracture model<sup>23</sup>, with a fracture threshold of 3000  $\mu\text{N}$  appears to indicate that fracture is not possible in MAF, the increased stress concentration from adjacent and cyclic contacts was thought to be capable of lowering the fracture threshold to loads imparted to abrasives in MAF (<50  $\mu\text{N}$ ). By investigating the effects of adjacent and cyclic contacts to the fracture threshold, this study was able to answer the question of fracture as a possible material removal mechanism in MAF. Finding that fracture was not possible below the fracture threshold (280  $\mu\text{N}$  – 290  $\mu\text{N}$ ), despite the presence of cyclic and adjacent contact stress

concentrations, this study concludes that fracture is not a material removal mechanism in MAF.

However, a lower fracture threshold than previously published, enables measurements of fracture toughness for smaller volumes, i.e. ultra-thin films and structures. Furthermore, this study has provided a better understanding of the effects of contact dimension, spacing, and repeated loading on fracture of brittle materials.

Future work will investigate the effects of increasing loading rate on fracture and deformation from cyclic loaded indentations. Future studies will investigate a variety of adjacent indent separation distances that were not studied in this experiment in order to achieve a more precise tracking of the effects of stress field interactions as two contacts approach each other. Such experiments aim to further extend the indentation fracture model to a variety of contact conditions. This will provide the manufacturing industry with a greater understanding of nanoscale fracture and deformation, and the ability to optimize mechanical nanofabrication methods, improving resolution, accuracy and throughput of the production process.

## APPENDIX A MATLAB M-FILE OF VON MISES STRESS FIELD CONTOURS FOR ADJACENT INDENTATIONS

```

% Von Mises Stress Fields
% Below a Cube Corner Indenter
% Using the Equations of Stress from;
% "Introduction to Contact Mechanics" Fischer-Cripps pp.97-99, 2002
% "Boussinesq's Problem for a Rigid Cone" Sneddon, 1948
% For the Masters Thesis of Jared Hann
% University of Florida, 2012

clear

% Preparing The Meshgrid
rsep=2; % Indent separation distance
x=round(400/rsep); % Add columns
v=0.25; % Poisson's ratio
r2=linspace(rsep,0); % Linspace rows
r22=(r2(1,1)-r2(1,2))*(1:x))+rsep; % Extra rows for correct size
z2=linspace(400,0,400); % Linspace columns
a=100*(tan(42.28*(pi/180))); % Indent radius (Fischer-Cripps)
p1=[fliplr(r22) r2]; % Row entries (flipped r22 plus r2)
q1=z2./a; % Column entries
[p,q]=meshgrid(p1,q1); % Meshgrid coordinates
R=(p.^2+q.^2-1).^2+4*q.^2).^0.25; % Dimensionless factor (Sneddon)
r=(1+q.^2).^0.5; % Dimensionless factor (Sneddon)
theta=atan2(1,q); % Dimensionless factor (Sneddon)
phi=0.5*atan2((2*q),(p.^2+q.^2-1)); % Dimensionless factor (Sneddon)

% Integrals (Inputs)
J02=(p.^2+q.^2).^0.5-(cos(phi)./R);
J11=(1./p).*((p.^2+q.^2).^0.5-(R.*cos(phi)));
J12=(1./p).*((r./R).*cos(theta-phi)-q.*(p.^2+q.^2).^0.5);
J01=0.5*(log(R.^2+2.*R.*r.*cos(theta-phi)+1+q.^2)-
log((q+(p.^2+q.^2).^0.5).^2));
J10=0.5*(p.*J01+1./p.*(1-R.*sin(phi))-q.*J11);

% Polar Coordinate Stresses
sigma_z=-(J01+q.*J02);
sigma_t=-(2*v.*J01+(1./p).*((1-2*v).*J10-q.*J11));
sigma_r=-(2*(1-v^2)*(1-v)^-1).*J01-sigma_z-sigma_t;
tau_rz=-(q.*J12);
z=-acosh(1./p);

% Flip And Scale The Stress Field So That It Will Fit A Second Stress Field
% First Remove NaN Columns In Sigma Matrices
sigma_z(:,size(sigma_z,2))=sigma_z(:,size(sigma_z,2)-1);
sigma_t(:,size(sigma_t,2))=sigma_t(:,size(sigma_t,2)-1);
sigma_r(:,size(sigma_r,2))=sigma_r(:,size(sigma_r,2)-1);
tau_rz(:,size(tau_rz,2))=tau_rz(:,size(tau_rz,2)-1);

% Flip The Portion Of The Matrix Containing The Indent.
fsigma_z=fliplr(sigma_z(:,size(sigma_z,2)-x+1:end));
fsigma_t=fliplr(sigma_t(:,size(sigma_t,2)-x+1:end));
fsigma_r=fliplr(sigma_r(:,size(sigma_r,2)-x+1:end));
ftau_rz=fliplr(tau_rz(:,size(tau_rz,2)-x+1:end));

% Flip A Portion Of The p Matrix.
% Flips the same number of columns flipped In The Sigma matrixes
fp=fliplr(p(:,size(p,2)-x+1:end));

%Remove Redundant Columns In The Flipped Matrices

```

```

fsigma_z(:,1)=[];
fsigma_t(:,1)=[];
fsigma_r(:,1)=[];
ftau_rz(:,1)=[];
fp(:,1)=[];

% Combine Flipped And Not Flipped
sigma_z=[sigma_z fsigma_z];
sigma_z=sigma_z+fliplr(sigma_z);

sigma_t=[sigma_t fsigma_t];
sigma_t=sigma_t+fliplr(sigma_t);

sigma_r=[sigma_r fsigma_r];
sigma_r=sigma_r+fliplr(sigma_r);

tau_rz=[tau_rz ftau_rz];
tau_rz=tau_rz+fliplr(tau_rz);

% Principal Stresses
newsigma_1=0.5*(sigma_r+sigma_z)+((0.5.*sigma_r-
0.5.*sigma_z).^2+tau_rz.^2).^0.5;
newsigma_3=0.5*(sigma_r+sigma_z)-((0.5.*sigma_r-
0.5.*sigma_z).^2+tau_rz.^2).^0.5;
newsigma_2=sigma_t;
newtau_max=0.5*(newsigma_1-newsigma_3);

% Construct Matrices That Define The x And y Positions Of Each Point In
% The Stress Matrix. p => Horizontal Direction. q => Vertical Direction
np=-p;
new_p=-fliplr([np fp]);
new_q=[q q(:,1:size(fp,2))];

% Von Mises Stresses
sigma_v=(0.5*((newsigma_1-newsigma_2).^2+(newsigma_1-
newsigma_3).^2+(newsigma_2-newsigma_3).^2)).^0.5

contourf(new_p,-new_q,sigma_v,20),xlabel('r/a'),ylabel('z/a');
title('\sigma_v');

% Colorbar Settings
B=colorbar('vert');
set(B, 'Position', [.91 .11 .05 .815])

% Saving the Figure as a BMP
% print(gcf, '-dbmp', 'Adjacent_I.bmp')

```

## APPENDIX B

### MATLAB M-FILE OF VON MISES STRESS FIELD CONTOURS FOR A SINGLE INDENTATION

```

% Von Mises Stress Fields
% Below a Cube Corner Indenter
% Using the Equations of Stress from;
% "Introduction to Contact Mechanics" Fischer-Cripps pp.97-99, 2002
% "Boussinesq's Problem for a Rigid Cone" Sneddon, 1948
% For the Masters Thesis of Jared Hann
% University of Florida, 2012

```

```

clear

% Indent Radius 'a'
hp = 50 % Depth of circle of contact (nm)
alpha = 42.28; % Effective cone angle for a cube corner
indenter
a = hp*tan(alpha); % Indentation radius

% Prepare the Meshgrid
r2=linspace(1600,0); % linspace (r axis)
z2=linspace(1600,0); % linspace (z axis)
p1=r2./a; % Normalized radial displacement
q1=z2./a; % Normalized z displacement
[p,q]=meshgrid(p1,q1);

% Inputs for Integrals
v=0.25; % Poisson's ratio
R=( (p.^2+q.^2-1).^2+4*q.^2).^0.25; % Dimensionless factor
r=(1+q.^2).^0.5; % Dimensionless factor
theta=atan2(1,q); % Dimensionless factor
phi=0.5*atan2((2*q),(p.^2+q.^2-1)); % Dimensionless factor

% Integrals
J02=(p.^2+q.^2).^(-0.5)-(cos(phi)./R);
J11=(1./p).*((p.^2+q.^2).^0.5-(R.*cos(phi)));
J12=(1./p).*((r./R).*cos(theta-phi)-q.*(p.^2+q.^2).^(-0.5));
J01=0.5*(log(R.^2+2.*R.*r.*cos(theta-phi)+1+q.^2)-
log((q+(p.^2+q.^2).^0.5).^2));
J10=0.5*(p.*J01+1./p.*(1-R.*sin(phi))-q.*J11);

% Polar Coordinate Stresses
sigma_z=-(J01+q.*J02);
sigma_t=-(2*v.*J01+(1./p).*((1-2*v).*J10-q.*J11));
sigma_r=-(2*(1-v^2)*(1-v)^(-1).*J01-sigma_z-sigma_t);
tau_rz=-(q.*J12);
z=-acosh(1./p);

% Principal Stresses
sigma_1=0.5*(sigma_r+sigma_z)+((0.5.*sigma_r-0.5.*sigma_z).^2+tau_rz.^2).^0.5;
sigma_3=0.5*(sigma_r+sigma_z)-((0.5.*sigma_r-0.5.*sigma_z).^2+tau_rz.^2).^0.5;
sigma_2=sigma_t;
tau_max=.5*(sigma_1-sigma_3);

% Removing NaNs
sigma_1(:,100)=sigma_1(:,99);
sigma_2(:,100)=sigma_2(:,99);
sigma_3(:,100)=sigma_3(:,99);
tau_max(:,100)=tau_max(:,99);

% Reflecting Stress Fields Along the Z Axis
fsigma_1=fliplr(sigma_1);
fsigma_2=fliplr(sigma_2);
fsigma_3=fliplr(sigma_3);
ftau_max=fliplr(tau_max);
fp=fliplr(p);
fp(:,1)=[];
np=-p;

% Correcting Matrix Dimensions
fsigma_1(:,1)=[];
fsigma_2(:,1)=[];
fsigma_3(:,1)=[];
ftau_max(:,1)=[];

```

```

% Corrected Principal Stresses
newsigma_1=[sigma_1 fsigma_1];
newsigma_2=[sigma_2 fsigma_2];
newsigma_3=[sigma_3 fsigma_3];
newtau_max=[tau_max ftau_max];
new_p=[np fp];
new_q=[q q(:,1:99)];

% Von Mises Stresses
sigma_v=(0.5*((newsigma_1-newsigma_2).^2+(newsigma_1-
newsigma_3).^2+(newsigma_2-newsigma_3).^2)).^0.5

contourf(new_p,-new_q,sigma_v,20),xlabel('r/a'),ylabel('z/a');
title('\sigma_v');

% Colorbar Settings
B=colorbar('vert');
set(B, 'Position', [.91 .11 .05 .815])

% Saving the Figure as a BMP
% print(gcf, '-dbmp', 'Adjacent_I.bmp')

```

## LIST OF REFERENCES

1. Guo, Recent Progress in nanoimprint technology and its applications. *Journal of Physics* **37** (11), R123-R141 (2004).
2. Ting, C. J., Huang, M. C., Tsai, H. Y., Chou, C. P. & Fu, C. C., Low cost fabrication of the large-area anti-reflection films from polymer by nanoimprint/hot-embossing technology. *Nanotechnology* **19** (20), 1-5 (2008).
3. Tseng, A. A., Jou, S., Notargiacomo, A. & Chen, T. P., Recent Developments in Tip-Based Nanofabrication and Its Roadmap. *Journal of Nanoscience and Nanotechnology* **8** (5), 2167-2186 (2008).
4. Giam, L. R., Wang, Y. & Mirkin, C. A., Nanoscale Molecular Transport: The Case of Dip-Pen Nanolithography. *Journal of Physical Chemistry A* **113** (16), 3779-3381 (2009).
5. Krebs, F. C., Tromholt, T. & Jorgensen, M., Upscaling of polymer solar cell fabrication using full roll-to-roll processing. *Nanoscale* **2** (6), 873 (2010).
6. Krebs, F. C., Gevorgyan, S. A. & Alstrap, J., A roll-to-roll process to flexible polymer solar cells: model studies, manufacture and operational stability studies. *Journal of Materials Chemistry* (30), 5442-5451 (2009).
7. Bhagavat, S., Ultra-low load multiple indentation response of materials: In purview of wiresaw slicing and other free abrasive machining (FAM) processes. *International Journal of Machine Tools and Manufacture* **47**, 666-672 (2007).
8. Hsu, C. Y., Chen, C. S. & Tsao, C. C., Free abrasive wire saw machining of ceramics. *International Journal of Advanced Manufacturing Technologies* **40** (5-6), 503-511 (2009).
9. Yamaguchi, H. *et al.*, Magnetic field-assisted finishing for micropore X-ray focussing mirrors fabricated by deep reactive ion etching. *CIRP Annals-Manufacturing Technologies* **59** (1), 351-354 (2010).
10. Y, E. *et al.*, Simulation-Based Study of MEMS X-Ray Optics for Microanalysis. *IEEE Journal of Quantum Electronics* **46** (9), 1295 (2010).
11. Vettiger, P. *et al.*, The Millipede - Nanotechnology Entering Data Storage. *IEEE Trans. Nanotech.* **1** (1), 39-55 (2002).
12. Pozidis, H. *et al.*, Demonstration of Thermomechanical Recording at 641 Gbit/in. *IEEE Trans. Magnetics* **40** (4), 2531-2536 (2004).

13. Wang, W., Wu, S., Reinhardt, K., Lu, Y. & Shaochen, C., Broadband Light Absorption Enhancement in Thin-film Silicon Solar Cells. *Nano Letters* **10**, 2012-2018 (2010).
14. Ma, Z., Ma, L. & Su, M., Engineering Three Dimensional Micromirror Arrays by Fiber-Drawing Nanomanufacturing for Solar Energy. *Advanced Materials* **20**, 3734-3738 (2008).
15. Koo, O. M., Rubenstein, I. & Onyuksel, H., Role of nanotechnology in targeted drug delivery and imaging: a concise review. *Nanomedicine: Nanotechnology, Biology and Medicine* **1** (3), 193-212 (2005).
16. Park, K., Nanotechnology: What it can do for drug delivery. *Journal of Control Release* **120** (1-2), 1-3 (2007).
17. Serano, E., Rus, G. & Garcia-Martinez, J., Nanotechnology for sustainable energy. *Renewable and Sustainable Energy Reviews* **13** (9), 2373-2384 (2009).
18. Grave, A. D., Olsen, S. I., Hansen, H. N. & Arentoft, M., in *Micromanufacturing, Engineering & Technology* (Elsevier, Oxford, 2010).
19. S K Sahoo, S. P. J. J. P., The present and future of nanotechnology in human health care. *Nanomedicine: Nanotechnology, Biology, and Medicine* **3**, 20-31 (2007).
20. Luo, J. & Fang, F., The First International Conference on Nanomanufacturing (NanoMan2008). *Journal of Micromechanics and Microengineering* **19** (5), 1 (2009).
21. Weiss, J. & P Takhistov, D. J. M., Functional Materials in Food Nanotechnology. *Journal of Food Science* **71** (9), 107-116 (2006).
22. Farhang, B., Nanotechnology and Lipids. *Lipid Technology* **19** (6), 132-135 (2007).
23. Lawn, B. R. & Evans, A. G., A model for crack initiation in elastic/plastic indentation fields. *Journal of Materials Science* **12**, 2195-2199 (1977).
24. Riveros, R. E. *et al.*, Magnetic Field-assisted Finishing of Silicon Microelectromechanical Systems Micro-pore X-ray Optics. *Journal of Manufacturing Science and Engineering*, 1-23 (2011).
25. Harding, D. S., Oliver, W. C. & Pharr, G. M., *Cracking During Nanoindentation and its Use in the Measurement of Fracture Toughness*, presented at Materials Research Society Symposium Proceedings, 1995 (unpublished).

26. Guiberteau, F., Padture, N. P., Cai, H. & Lawn, B. R., Indentation fatigue: A simple cyclic Hertzian test for measuring damage accumulation in polycrystalline ceramics. *Philosophical Magazine A* **68** (5), 1003-1016 (1993).
27. Pharr, G. M., Measurement of mechanical properties by ultra-low load indentation. *Materials Science and Engineering* **A253**, 151-159 (1998).
28. Cook, R. F. & Pharr, G. M., Direct observation and analysis of indentation cracking in glasses and ceramics. *Journal of American Ceramic Society* **73**, 787 (1990).
29. Chen, J., Indentation-based methods to assess fracture toughness for thin coatings. *Journal of Physics D: Applied Physics* **45** (20), 1-14 (2012).
30. Harding, D. S., Pharr, G. M. & Oliver, W. C., *Cracking during nanoindentation and its use in the measurement of fracture toughness*, presented at Materials Research Society Symposium Proceedings (unpublished).
31. Pharr, G. M., Harding, D. S. & Oliver, W. C., in *Mechanical Properties and Deformation Behavior of Materials Having Ultra-Fine Microstructures*, edited by Natasi, M., Parkin, D. M. & Gleiter, H. (Porto Novo, 1992), Vol. 233, pp. 417-428.
32. Anstis, G. R., Chantikul, P., Lawn, B. R. & Marshall, D. B., A Critical Evaluation of Indentation Techniques for Measuring Fracture Toughness: I Direct Measurements. *Journal of the American Ceramic Society* **64** (9), 533-538 (1981).
33. Lawn, B. R., *Fracture of Brittle Solids* (Cambridge University Press, Cambridge, 1993).
34. Marshall, D. B. & Lawn, B. R., An Indentation Technique for Measuring Stresses in Tempered Glass Surfaces. *Journal of the American Ceramic Society* **60** (1-2), 31 (1977).
35. Hill, R., *Plasticity* (Clarendon Press, Oxford).
36. Sih, G. C., *Handbook of Stress Intensity Factors* (Lehigh University Press, Lehigh, 1973).
37. Lawn, B. R., Fracture and deformation in brittle solids: A perspective on the issue of scale. *Journal of Materials Research* **19** (1), 22-29 (2004).
38. Feynman, R. P., There's Plenty of Room at the Bottom, Available at HYPERLINK <http://calteches.library.caltech.edu/1976/1/1960Bottom.pdf> (1959).

39. Zeng, K. & Rowcliffe, D., Vickers Indentation in Glass-I, Residual Stress Fields and Iso-stress Contour Maps. *Acta Metallurgica et Materiala* **43** (5), 1935-1943 (1995).
40. Zhang, W. & Subhash, G., Finite element analysis of interacting Vickers indentations on brittle materials. *Acta Materiala* **49**, 2961-2974 (2001).
41. Choi, S. R. & Salem, J. A., Interaction of cracks between two adjacent indents in glass. *Journal of Materials Science* **28**, 501-505 (1993).
42. Twigg, P. C., Davidge, R. W., Riley, F. L. & Franco, A., Indentation-induced crack interaction in ceramics. *Philosophical Magazine A* **74** (5), 1245-1252 (1996).
43. Vliet, K. J. V. & Suresh, S., Simulations of cyclic normal indentation of crystal surfaces using the bubble-raft model. *Philosophical Magazine A* **82** (10), 1993-2001 (2002).
44. Bragg, L. & Nye, J. F., A Dynamical Model of a Crystal Structure. *Proceedings of the Royal Society of London, Series A, Mathematical and Physical Sciences* **190** (1023), 474-481 (1947).
45. Muhlstein, C. L., Brown, S. B. & Ritchie, R. O., High-cycle fatigue and durability of polycrystalline silicon thin films in ambient air. *Sensors and Actuators A: Physical* **94** (3), 177-188 (2001).
46. Li, X. & bhushan, B., Fatigue studies of nanoscale structures for MEMS/NEMS applications using nanoindentation techniques. *Surface and Coatings Technology* **163-164**, 521-526 (2003).
47. Clarke, D. R., Kroll, M. C., Kirchner, P. D., Cook, R. F. & Hockey, B. J., Amorphization and Conductivity of Silicon and Germanium Induced by Indentation. *Physical Review Letters* **60** (21), 2156-2159 (1988).
48. Gogotsi, Y. G., Kailer, A. & Nickel, K. G., Phase transformations in materials studied by micro-Raman spectroscopy of indentations. *Materials Research Innovations* **1** (1), 3-9 (1997).
49. Pharr, G. M., Oliver, W. C. & Harding, D. S., New evidence for a pressure-induced phase transformation during the indentation of silicon. *Journal of Materials Research* **6** (6), 1129-1130 (1991).
50. Guiu, F., Reece, M. J. & Vaughn, D. A. J., Cyclic fatigue of ceramics. *Journal of Materials Science* **26**, 3275-3286 (1991).

51. Cavaliere, P., Cyclic deformation of ultra-fine and nanocrystalline metals through nanoindentation: similarities with crack propagation. *Procedia Engineering* **2**, 213-222 (2010).
52. Bonilla, A. & Fuierer, R. Combining AFM and Instrumented Indentation for Mechanical Characterization at the Nanoscale. AVS Conference. (Boston, 2008).
53. Electrochemistry, Available at HYPERLINK <http://www.asylumresearch.com/Gallery/Materials/Materials.shtml#electro> (2012).
54. Bhushan, B. & Li, B., Micromechanical and tribological characterization of doped single-crystal silicon and polysilicon films for microelectromechanical systems devices. *Journal of Materials Research* **12** (1), 59 (1997).
55. Pharr, G. M., Oliver, W. C. & Clarke, D. R., Hysteresis and Discontinuity in the Indentation Load--Displacement Behavior of Silicon. *Scripta Materiala* **23** (11), 1949-1952 (1989).
56. Gogotsi, Y. G., Dominich, V. & Dub, S., Cyclic nanoindentation and Raman microspectroscopy study of phase transformations in semiconductors. *Journal of Materials Research* **15** (4), 871-879 (2000).
57. Juliano, T., Gogotsi, Y. & Dominich, V., Effect of indentation unloading conditions on phase transformation induced events in silicon. *Journal of Materials Research* **18** (5), 1192-1201 (2003).
58. Jang, J., Lance, M. J., Wen, S., Tsui, T. Y. & Pharr, G. M., Indentation-induced phase transformations in silicon: influences of load, rate and indenter angle on the transformation behavior. *Acta Materiala* **53**, 1759-1770 (2005).
59. Xu, H. H. K., Jahanmir, S. & Wang, Y., Effect of Grain Size on Scratch Interactions and Material Removal in Alumina. *Journal of the American Ceramic Society* **78** (4), 881-891 (1995).
60. Zeng, K. & Rowcliffe, D., Experimental Measurement of Residual Stress Field Around Sharp Indentation in Glass. *Journal of the American Ceramic Society* **77** (2), 524-530 (1994).
61. Li, J., Kao, I. & Prasad, V., Modelling stresses of contacts in wire saw slicing of polycrystalline and crystalline ingots: application to silicon wafer production. *Journal of Electronic Packaging* **120**, 123-128 (1998).
62. Sneddon, I., Boussinesq's problem for a rigid cone. *Mathematical Proceedings of the Cambridge Philosophical Society* **44**, 492-507 (1948).

63. Fischer-Cripps, A. C., *Nanoindentation* (Springer-Verlag, New York, 2002).
64. Fischer-Cripps, *Introduction to Contact Mechanics* (Springer-Verlag, New York, 2000).
65. Rswarbrick, Von Mises yield criterion, Available at HYPERLINK [http://en.wikipedia.org/wiki/Von\\_Mises\\_yield\\_criterion](http://en.wikipedia.org/wiki/Von_Mises_yield_criterion) (2009).
66. Alliance for American Manufacturing (AAM), Manufacturing, Jobs and the US Economy, Available at HYPERLINK <http://americanmanufacturing.org/category/issues/jobs-and-economy/manufacturing-jobs-and-us-economy> (2010).
67. Fischer-Cripps, A. C., *The IBIS Handbook of Nanoindentation*, 1st ed. (Fischer-Cripps Laboratories Pty Ltd, Forestville, 2009).
68. Sherman, R. & Hirt, D., Surface cleaning with carbon dioxide snow jet. *Journal of Vacuum Science & Technology* **12** (4), 1876-1881 (1994).
69. Doemer, M. F. & Nix, W. D., A method for interpreting the data from depth-sensing indentation instruments. *Journal of Materials Research* **1**, 601-609 (1986).
70. Pharr, G. M. & Oliver, W. C., Measurement of thin film mechanical properties using nanoindentation. *MRS Bulletin* **17** (7), 28-33 (1992).
71. Oliver, W. C. & Pharr, G. M., An improved technique for determining hardness and elastic modulus using load and displacement sensing indentation experiments. *Journal of Materials Research* **7** (6), 1564-1583 (1992).
72. Loubet, J. L., Georges, J. M., Marchesini, O. & Meille, G., Vickers Indentation Curves of Magnesium Oxide (MgO). *Journal of Tribology* **106** (1), 43-48 (1984).
73. Nix, W. D., Mechanical properties of thin films. *Metallurgical Transactions* **20** (11), 2217-2245 (1989).
74. Pethica, J. B., Hutchings, R. & Oliver, W. C., Hardness measurement at penetration depths as small as 20 nm. *Philosophical Magazine A* **48** (4), 593-606 (1983).
75. Newey, D., Wilkens, M. A. & Pollock, H. M., An ultra-low-load penetration hardness tester. *Journal of Physics E: Scientific Instruments* **15** (1), 119-122 (1982).

76. Kese, K. & Rowcliffe, D. J., Nanoindentation Method for Measuring Residual Stress in Brittle Materials. *Journal of the American Ceramic Society* **86** (5), 811-16 (2003).
77. Kruzic, J. & Ritchie, R., Determining the toughness of ceramics from Vickers indentations using the crack-opening displacements: an experimental study. *Journal of American Ceramics Society* **86** (8), 1433-1436 (2003).
78. Sundararajan, S. & Bhushan, B., Fatigue studies of nanoscale structures for MEMS/NEMS applications using nanoindentation techniques. *Surface and Coatings Technology* **163-164**, 521-526 (2003).
79. Pethica, J. B. & Oliver, W. C., *Mechanical Properties of Nanometre Volumes of Material: use of the Elastic Response of Small Area Indentations*, presented at MRS Proceedings, 1988 (unpublished).

## BIOGRAPHICAL SKETCH

Jared Nathan Hann was born in Adelaide, Australia, in 1982. He graduated from Marryatville High School in Adelaide, Australia in 1999 and then worked to pay for a two-year service mission, which was fulfilled in Florida, USA between 2001 and 2003. Following his missionary service, Jared returned to Australia and continued his studies in chemistry and biological Sciences at the University of Queensland in Brisbane, Australia. Graduating in 2007 with a major in nanotechnology, Jared worked to save for travel to Central America, Israel and the USA. While travelling through Florida to visit friends from his missionary service, Jared decided to follow his passion for space and apply for graduate school in aerospace engineering at the University of Florida. After returning to Australia to earn the money for this next challenge, he came to Florida at the beginning of 2010 to begin graduate school, and a project in a rocket propulsion lab. However, funding was cut to his project and a decision was made to move to a project in mechanical engineering in the field of nanomanufacturing. Here, over a period of two years, Jared completed his Master of Science in mechanical engineering. His wife, Nichelle Baxter Hann, is graduating with her PhD in geology at the same time Jared is graduating with his Master's. Following graduation, they plan to obtain employment in their respective fields and continue their passion for science.